DOCTORAL THESIS

Gravitational Microlensing Simulation for the Large Survey Era

Author:
David Specht

Supervisor:
Dr. Eamonn Kerins

A thesis submitted to the University of Manchester
for the degree of Doctor of Philosophy

in the

Department of Physics and Astronomy in the School of Natural Sciences
Faculty of Science and Engineering

2023

Contents

Contents **2**

List of Figures **7**

List of Tables **9**

Physical Constants **10**

Abstract **11**

Declaration of Authorship **12**

Copyright Statement **13**

Acknowledgements **14**

Dedication **14**

Preface **15**

1 Introduction **16**
- 1.1 What is Gravitational Lensing? 16
- 1.2 Exoplanet detection 18
- 1.3 Microlensing Surveys 19
- 1.4 The PSPL Model 22
- 1.5 Finite Source Effects 26
- 1.6 Microlensing Parallax 30
  - 1.6.1 Earth motion parallax 30
  - 1.6.2 Space-based parallax 32
- 1.7 Binary Lensing 33
- 1.8 Astrometric Microlensing 35
- 1.9 Outline 38

2 MaBμlS-2 **40**
- 2.1 The Besançon Galactic Model 41
  - 2.1.1 The Thin Disk 44

- 2.1.2 The Thick Disk . . . 44
- 2.1.3 The Bar . . . 45
- 2.1.4 The Halo . . . 45
- 2.1.5 Adding Low Mass Objects . . . 46
- 2.1.6 Synthetic Catalogue Generation . . . 47
- 2.2 Microlensing Parameters . . . 49
  - 2.2.1 The Microlensing Optical Depth . . . 50
  - 2.2.2 The Average Einstein Radius Crossing Time . . . 51
  - 2.2.3 The Microlensing Event Rate . . . 52
- 2.3 Improvements on Legacy MaBμlS . . . 53
  - 2.3.1 Error Estimation . . . 53
  - 2.3.2 Finite Source Effects . . . 54
  - 2.3.3 Event Selection Criterion . . . 56
- 2.4 Online Tool Functionality . . . 58
- 2.5 Comparison with OGLE-IV survey results . . . 59
- 2.6 MaBμlS-2 in Summary . . . 61

3 Detecting FFPs From Space **67**
- 3.1 Space Telescopes . . . 67
- 3.2 Free Floating Planets . . . 68
- 3.3 Modifying MaBμlS-2 . . . 70
  - 3.3.1 Signal-to-noise criteria . . . 71
  - 3.3.2 The finite source measurement . . . 73
  - 3.3.3 Introducing a parallax measurement . . . 73
- 3.4 Results . . . 74

4 Exoplanets From Kepler K2 Campaign 9 **82**
- 4.1 K2-2016-BLG-0005 . . . 88
- 4.2 The binary parameterisation . . . 92
- 4.3 The fitting process . . . 94
- 4.4 Analysis of the source . . . 101
- 4.5 Analysis of the lens . . . 101
- 4.6 Conclusion . . . 102

5 Complex Caustics **105**
- 5.1 The Earth Microlensing Zone . . . 107
  - 5.1.1 The Raycasting Algorithm . . . 111
  - 5.1.2 Results . . . 113
  - 5.1.3 Detection Probability and Event Rate . . . 115
- 5.2 GPU Powered Microlensing . . . 115
- 5.3 Conclusion . . . 118

6 Conclusion **120**

List of Figures

1.1 The planetary mass vs semi-major axis distribution of known exoplanets is shown on a logarithmic scale. 20
1.2 The microlensing schematic: an observer (on the right), views a source object at a distance D_{S} (on the left) undergoing a microlensing event by a lens object at a distance D_{L} (in the middle). 23
1.3 The shape of an infinitesimal unit area of the source in polar coordinates at a distance u from the lens is shown, where in this case $u < 1$, as it is interior to the Einstein radius, shown a circle of radius θ_{E} centred on the lens. 25
1.4 On the left is the PSPL magnification map, centred at $(X, Y) = (0, 0)$ on the lens. 26
1.5 A simulated view of a red giant star, with a source radius one fifth of the Einstein radius, is shown undergoing gravitational microlensing. 27
1.6 Shown is the setup for Earth motion parallax. 31
1.7 Artists impression of several configurations for a space-based parallax scenario. 32
1.8 Shown are examples of the magnification maps of the close, resonant and wide binary topologies, from left to right, in the s, q parameter space. . . . 34
1.9 Shown above is an example of the magnification map (shown on a logarithmic scale) of a resonant binary caustic topology. 36
1.10 The source centroid offsets for a PSPL model (left), FSPL model (middle) and binary lens model (right) are shown on the top row. On the bottom row is shown the trajectory of the source for three different impact parameters: $u_0 = 0.1$, $u_0 = 0.5$ and $u_0 = 1.0$. 38

2.1 The colour-magnitude diagram for all source stars generated by BGM1307 for the HST comparison is shown above in the Sloan r filter and $r - i$ colour. 42
2.2 The proper motion distributions in Galactic coordinates are shown for both disk (left) and bar (right) populations. 43
2.3 The reduced χ^2 minimisation for brown dwarf mass function slope for legacy MaBμlSwith MOA-II data and the new MaBμlS-2 with OGLE-IV data is shown. 47

2.4 On the top is shown the MOA-II timescale map, with the $b < 0^\circ$ portion of the OGLE-IV timescale map shown in the middle and the difference between the two (OGLE-IV - MOA-II) is shown on the bottom. 48
2.5 The microlensing optical depth in the Johnson Cousins I-band filter is shown over the entire MaBμlS-2 simulated field. 51
2.6 The average microlensing timescale is shown across the MaBμlS-2 field, using the same configuration and selection criteria as figure 2.5. 52
2.7 On the left is shown the microlensing event rate per source star per year, again using the same configuration and selection criteria as figure 2.5, with values on the order of 10^{-5}. 53
2.8 From top to bottom are shown the optical depth τ, average event timescale $\langle t_{\mathrm{E}} \rangle$, event rate per source star Γ_* and event rate per square degree $\Gamma_\circ$ on the left and their associated error maps on the right, all using a signal-to-noise at peak magnification requirement of $S/N \geq 50$ and a survey limiting magnitude of $m_{\mathrm{lim}} = 21$. 55
2.9 The distribution of u_{max} as a function of A_{min} and ρ is shown on the left, with the analytical form of $A_{\mathrm{cut}}(\rho)$ shown in blue. 57
2.10 Shown is the interface for the MaBμlS-2 online tool. 59
2.11 The OGLE-IV 8,000 event survey microlensing maps are shown in the left column with associated error maps on the right. 63
2.12 The I-band MaBμlS-2 parameter maps using equation 2.32 as the event selection criterion. 64
2.13 On the left is shown the residual between the OGLE-IV 8,000 event maps and the MaBμlS-2 equivalent, normalised to the error. 65
2.14 Same as figure 2.13, but comparing the legacy MaBμlS to OGLE-IV data. . 66

3.1 The Nancy Grace Roman Space Telescope (left, *credit: NASA*) and EUCLID Space Telescope (right, *credit: ESA*) are pictured. 69
3.2 The ROMAN W146 filter, showing its transmission curve (blue) superimposed with the Johnson-Cousins H (dashed red line) and J (dotted red line). 71
3.3 Shown are the distributions of ρ assuming Earth mass (blue line) and Jupiter mass (orange line) FFPs, weighted using the rate-weight parameter w^p from equation 2.15. 72
3.4 Illustration of the contiguity enforcing algorithm. 76
3.5 Various FFP event rate maps produced by MaBμlS-2 are shown, with the event rate displayed on a logarithmic scale. 77
3.6 The cumulative event rate fraction distributions are shown, with each distribution corresponding to the rate map of the same row and column from figure 3.5. 78

4.1 Shown is the K2C9 superstamp inside which the survey's events were found, superimposed over a 2MASS image of the Galactic center aligned in equatorial coordinates, extracted using the *Aladin* tool (Bonnarel et al., 2000). 83
4.2 The K2C9 photometry for the 12 FFP candidate events which were also found by KMTNet are shown in blue with associated errorbars, along with the degenerate model from equation 4.3 overlayed in a solid red line. . . . 85
4.3 Same as figure 4.2, but for the nine events found by OGLE. 86
4.4 The relative event rates of various models are shown, assuming K2 survey optics and $u_t = 1$. 89
4.5 The K2C9 photometry gathered for the K2-2016-BLG-0005 event, with associated errorbars, is shown on top of the best fit binary model (black solid line). 90
4.6 Same as figure 4.5, but for the ground photometry. 91
4.7 The K2-2016-BLG-0005 event is shown in its entirety, including the larger PSPL trend from the primary lens, with all photometry contributions from both ground-based observatories and KEPLER. 92
4.8 The magnification maps for the best fit standard wide solution (left column) and two close solutions (middle and right columns) are shown on a log-scale to compress the dynamic range for illustrative purposes. 96
4.9 The distributions of the top 50% best performing samples extracted from the fitting process and plotted in an s, q parameter space are shown for the close, resonant and wide solutions. 98
4.10 The corner plot displaying the distributions of the best 50% performing solutions from stage five for the standard wide caustic model, for the parameters t_0, u_0,t_E, t_* and $t_{0,\mathrm{pl}}$ is shown. 99
4.11 Shown above is the continuation of figure 4.10, for the parameters $u_{0,\mathrm{pl}}$, $t_{\mathrm{E,pl}}$, $\pi_{\mathrm{E,N}}$, $\pi_{\mathrm{E,E}}$ and $f_{\mathrm{s,sat}}$, the latter representing the scaling flux for the K2C9 photometry. 100
4.12 Shown are the final 2D joint distributions of parameters from figures 4.10 and 4.11. 100
4.13 The colour-magnitude diagram of stars within 60" of K2-2016-BLG-0005, indicated with black dots, calibrated to the PanSTARRS-1 (*PS1*) system, is shown. 103
4.14 An updated version of figure 1.1 with K2-2016-BLG-0005Lb indicated by a red cross. 104

5.1 The dimensions of the central (primary) caustic are shown. 108
5.2 The dimensions of the planetary caustics are shown, for both the close (left) and wide (right) topologies. 110

5.3 Shown on the left are the raycasting emission and receiver planes for a wide ($s = 1.5$, $q = 0.005$) binary lens, with lens locations indicated by black crosses. 113
5.4 The Solar System caustic network is shown for the aligned configuration of the Solar System. 114
5.5 Same as figure 5.4 but for a spiral configuration of the Solar System, where the viewing axis is aligned with the normal to the plane of the Solar System. 115
5.6 A noisy magnification map of the lenses described in table 5.1 is shown, with critical boundaries drawn as a green line and lens locations indicated by green plus symbols. 117
5.7 Shown is the result of applying the de-noising algorithm to the magnification map in figure 5.6. 118

List of Tables

2.1 The exponential profile fits for optical depth maps in the $|l| < 5°, b < 0°$ region using the normalisation τ_0 and scale size a from equation 2.12. 47

2.2 The magnitude brackets used for each of the four catalogues generated for each line of sight in the MaBμlS-2 simulation. 49

2.3 Tabulated above are the sky backgrounds for each filter used in equation 2.28. 58

3.1 The parameters $\Omega_{\rm psf}$, $m_{\rm zp}$, $t_{\rm exp}$ and $\mu_{\rm sky}$ used in MaBμlS-2 from equations 2.27, 2.28 and 2.20 for the ROMAN W146, EUCLID VIS and NISP-H filters are tabulated below. 68

3.2 The signal-to-noise $u_{\rm max}$ grid parameters are listed with their axis ranges and grid spacing distribution. Each axis was sampled with a resolution of 20 points. 72

3.3 The parameter ranges for the finite source detection $u_{\rm max}$ grid. 73

3.4 The parameter ranges for the parallax detection $u_{\rm max}$ grid are shown, as well as the number of grid points used. 75

3.5 Centroid locations of the ROMAN Cycle-7 fields in Galactic (l, b) coordinates, evaluated in the work done by Penny et al. (2019). 76

3.6 Centroid locations of the EUCLID fields in Galactic (l, b) coordinates selected after optimisation. 76

3.7 The annual FFP detection rates are shown tabulated for each model, combination of filters and combination of simulated event selection criteria. . 79

4.1 The best fit parameters for the K2C9 FFP candidate events found by the pipeline described in McDonald et al. (2021), using the flux model from equation 4.3. 87

4.2 Details on the ground-based telescopes used in the analysis of K2-2016-BLG-0005. 93

4.3 The fitted PSPL, binary, finite source and parallax model parameters are tabulated above for the best fit solutions of each of the four tested models. 98

4.4 The properties of the lens are tabulated above, including the binary parameters s and q. 102

5.1 The lens system configuration (normalised mass and positions) are shown for each component. 116

Physical Constants

Speed of Light	$c = 2.997\,924\,58 \times 10^{8}\,\mathrm{m\,s^{-1}}$
Newton's Gravitational Constant	$G = 6.674\,30 \times 10^{-11}\,\mathrm{m^{3}\,kg^{-1}\,s^{-2}}$
Astronomical Unit	$AU = 1.495\,98 \times 10^{11}\,\mathrm{m}$
Kiloparsec	$kpc = 3.0857 \times 10^{19}\,\mathrm{m}$
Year	$yr = 3.155\,76 \times 10^{7}\,\mathrm{s}$
Arcsecond	$arcsec, '' = 4.8481 \times 10^{-6}\,\mathrm{rad}$
Milliarcsecond	$mas = 1 \times 10^{-3}\,''$
Solar Mass	$M_{\odot} = 1.988\,47 \times 10^{30}\,\mathrm{kg}$
Jupiter Mass	$M_{\mathrm{Jup}} = 1.898\,13 \times 10^{27}\,\mathrm{kg}$
Earth Mass	$M_{\oplus} = 5.9742 \times 10^{24}\,\mathrm{kg}$
Solar Luminosity	$L_{\odot} = 3.828 \times 10^{26}\,\mathrm{kg\,m^{2}\,s^{-3}}$

THE UNIVERSITY OF MANCHESTER

Abstract

Faculty of Science and Engineering
Department of Physics and Astronomy in the School of Natural Sciences

Doctor of Philosophy

Gravitational Microlensing Simulation for the Large Survey Era

by David Specht

Over the coming decade, new space-based and ground-based observatories promise to usher in a large survey era of gravitational microlensing science, promising a host of new exoplanet discoveries as well as high fidelity data on Galactic structure. To compliment these scientific endeavours, accurate microlensing simulations are required to inform mission parameters and analyse the unprecedented diversity of results. This work aims to provide some of the tools with which to accomplish these tasks, as well as providing a framework for further development. Primarily, the new MaBμlS-2 simulation tool was developed to simulate microlensing parameters such as the event rate or optical depth and shows a higher level of agreement with empirical results from the OGLE-IV survey than has been achieved with previous work and surveys. MaBμlS-2 was then employed to inform a future mission proposal by the Euclid and Roman space-based observatories aiming to characterise the free-floating planet (FFP) mass distribution via microlensing, demonstrating that such a mission could detect hundreds of Earth mass FFPs over the life time of the mission. Work was also done analysing the binary microlensing event K2-2016-BLG-0005, found by the Kepler Space Telescope during its K2C9 microlensing campaign, which led to the discovery of a 1.10 ± 0.08 Jupiter mass exoplanet. This demonstrated the efficacy of using a space-based observatory at leading the discovery of exoplanets via the microlensing method. In addition to work on binary events, a raycasting simulation code was developed to analyse the magnification maps of even higher order lens systems, which was then adapted to work on a graphics processing unit, achieving increases in computation speed of two orders of magnitude, paving the way for more wide spread future applications of trinary or higher lensing calculations.

Declaration of Authorship

I, David Specht, declare that this thesis titled, “Gravitational Microlensing Simulation for the Large Survey Era” and the work presented in it are my own. I confirm that:

- This work was done wholly while in candidature for a research degree at this University.
- Where I have consulted the published work of others, this is always clearly attributed.
- I have acknowledged all main sources of help.
- Where the thesis is based on work done by myself jointly with others, I have made clear exactly what was done by others and what I have contributed myself.

Copyright Statement

(i) The author of this thesis (including any appendices and/or schedules to this thesis) owns certain copyright or related rights in it (the “Copyright”) and he has given The University of Manchester certain rights to use such Copyright, including for administrative purposes.

(ii) Copies of this thesis, either in full or in extracts and whether in hard or electronic copy, may be made **only** in accordance with the Copyright, Designs and Patents Act 1988 (as amended) and regulations issued under it or, where appropriate, in accordance with licensing agreements which the University has from time to time. This page must form part of any such copies made.

(iii) The ownership of certain Copyright, patents, designs, trademarks and other intellectual property (the “Intellectual Property”) and any reproductions of copyright works in the thesis, for example graphs and tables (“Reproductions”), which may be described in this thesis, may not be owned by the author and may be owned by third parties. Such Intellectual Property and Reproductions cannot and must not be made available for use without the prior written permission of the owner(s) of the relevant Intellectual Property and/or Reproductions.

(iv) Further information on the conditions under which disclosure, publication and commercialisation of this thesis, the Copyright and any Intellectual Property and/or Reproductions described in it may take place is available in the University IP Policy (see documents.manchester.ac.uk), in any relevant Thesis restriction declarations deposited in the University Library, The University Library’s regulations (see www.library.manchester.ac.uk/about/regulations/) and in The University’s policy on Presentation of Theses.

Acknowledgements

First and foremost, I would like to thank my PhD supervisor, Dr. Eamonn Kerins, for making this thesis possible and for providing the many fantastic research opportunities I've had and benefited from over the last four years. My advisor, Dr. Rowan Smith, has also been of great assistance throughout my PhD, providing guidance where necessary. It has of course been an honour working with many of the great minds in the field on multiple projects, including Dr. Radek Poleski, whose patience while I was using his MCPM code was without bound. Last but certainly not least, I would like to thank my Parents and Uncle for their unwavering support throughout the PhD journey, support without which I would not have succeeded in finishing this work. An honourable mention goes to the family cat Daisy, who although limited in her intellectual grasp of gravitational microlensing and exoplanet science, has provided much moral support throughout the process, simply by virtue of existing.

Preface

The author's experience in the field of astrophysics includes a 1st class masters degree (MPhys) in Physics with Astrophysics from the University of Manchester, having starting in September 2014 and graduating in June 2018, with research experience from an STFC funded PhD program from September 2018 until March 2022, working for the Jodrell Bank Centre for Astrophysics (JBCA).

Chapter 1

Introduction

1.1 What is Gravitational Lensing?

Rays of light, much like everyday objects, are influenced by gravity. Like a bullet travelling at high speed, their trajectories will ever so slightly curve as they are drawn towards the gravitational body, known as the lens. This effect is subtle; for a light ray, whose journey through the universe passes just above the Earth's atmosphere, its angle of deflection would be only one half of a milli-arcsecond, or one ten-millionth of a degree. This effect scales proportionally with the mass of the lens M_L and inversely with the distance of closest approach b given by

$$\alpha = \frac{4GM_\mathrm{L}}{bc^2}, \tag{1.1}$$

resulting in deflection angles which, although still small, are thousands of times greater for stellar mass objects such as our sun. In the most extreme cases, the lens is an entire galaxy with a mass of hundreds of billions of stars, or a galaxy cluster, with masses upward of a hundred trillion stars. In these galactic scale theatres, the deflection of light can be sufficiently large that we can observe its effect through our telescopes; many famous Hubble Space Telescope images showcase visually the consequences of this phenomenon. The deflection of light lends itself well to the name of this phenomenon: gravitational lensing.

The historical legacy of gravitational lensing is also significant. Albert Einstein's general theory of relativity was used in the total solar eclipse of 29th May 1919 by British astronomer Sir Arthur Eddington to predict the deflection of the position of background stars near the sun during totality (Earman & Glymour, 1980). His prediction suggested a deflection angle twice as large as predicted by the accepted theory of gravity at the time, Newtonian gravity (Sauer, 2008). The general relativistic value of 1.75 arcseconds was shown to be accurate from Eddington's observations, propelling Einstein to international levels of fame and, along with the precession of Mercury's perihelion, became one of the first successful tests of the theory.

The field of gravitational lensing developed over the following century and has since become an excellent tool for studying the universe. Today, the field is divided into three main subcategories: strong lensing, weak lensing and microlensing. Strong lensing appears in a regime where the lens is of sufficient mass that resolved background objects are visibly distorted. The distortion generated by the lens' gravitational potential can be used to reverse engineer the mass distribution of the lens object, which is typically a galaxy (Trick et al., 2016; Nightingale et al., 2019). The earliest detection of a strong lensing system was of the "double quasar" B0957+561 A and B (Walsh, Carswell & Weymann, 1979), originally detected as part of the Jodrell Bank 966 MHz radio survey. Follow up optical observations showed the dual nature of the quasar, with each component separated by 6 arcseconds with identical redshifts of $z = 1.41$, as well as very similar spectral characteristics. Walsh, Carswell & Weymann (1979) proposed that the observations could best be explained by a distant quasar being lensed by the gravity of a foreground galaxy. Further observations confirmed this to be the case; see Walsh (1989) for a historical review. Strong lensing is particularly useful in the detection of dark matter (Limousin et al., 2008), as the retrieved mass distribution will often suggest more mass than is provided by the detectable luminous matter locked up in stars, gas and dust.

Weak lensing operates in a similar regime of resolvable galaxies as the background objects (sources) but does not require a strong visual distortion. Instead, it relies on measuring the apparent ellipticity of source galaxies in a local region around the lensing and comparing the average ellipticity of these galaxies to what would be expected from a purely random distribution of galactic rotations (Mellier, 1999). The effect of gravitational lensing in the weak regime is to stretch the image of source galaxies along an axis perpendicular to the direction of the mass distribution, resulting in a statistically significant excess of ellipticity which can be used to retrieve the profile of the lens mass distribution.

The third manifestation of gravitational lensing is in the form of microlensing. Often, the source objects of gravitational lensing are not galaxies, but stars in the Milky Way. Although the alignment of stars in the sky from Earth's vantage point close enough to produce a measurable lensing effect is extremely uncommon, due to the vast number of stars in our Galaxy (on the order of one hundred billion), stars in the sky can act as sources for other stellar lenses. If the angular separation of the two objects is small enough such that the light rays from the source will undergo significant deflection passing near the lens star, the image of the source will become noticeably distorted, resulting in a magnification of its apparent brightness (Paczynski, 1986). While stars other than our Sun are not typically resolvable as disks in the sky, we can still observe this gravitational lensing effect by monitoring the brightness of the source star over time, recording its flux as the source and lens approach and move past each other. It is in this regime, where the source is not resolvable and where the strength of the lensing effect varies over time, that we observe a gravitational microlensing event (Chang & Refsdal, 1979).

1.2 Exoplanet detection

The uses of gravitational microlensing are several-fold. In some cases, the lens system includes a star and a gravitationally bound exoplanet, in which case there is the possibility that the light-curve of the source star will show binary lensing effects which infer the presence of the exoplanet. To date, 130 exoplanets have been confirmed via microlensing[1]. Microlensing is particularly useful in the field of exoplanet science due to its ability to detect exoplanets orbiting beyond the snow-line of their host stars (Hwang et al., 2022), where we expect to find many low mass planets (Mordasini, 2018). The snow-line represents the distance from a star beyond which volatiles such as water and ammonia ices can form, which are predicted by planetary formation theories to aid in the initial accumulation of planetary cores. Shown in figure 1.1, one can see the planetary mass vs semi-major axis parameter space of discovered exoplanets, where the efficacy of microlensing for detecting low mass planets beyond the snowline is highlighted.

The main competing methods of exoplanet detection are the transit method and radial velocity method, with a notable contribution form direct imaging. The transit method is responsible for the majority of exoplanet discoveries and relies on the alignment of an exoplanet' orbital plane with the observer's line of sight, such that the planet transits the surface of its host star at some point during its orbit, blocking out a portion of that star's light. For a planet of radius R_p in an orbit around a star of radius R_s with semi-major axis a, ellipticity ϵ, argument of periapsis ω (relative to the observer's line of sight) and orbital inclination i, the minimum impact parameter r_min of the planet to the star for an observer is given by (Wright & Gaudi, 2013)

$$r_\mathrm{min} = \frac{a(1-\epsilon^2)}{1+\epsilon\cos(\omega)}\cos(i). \tag{1.2}$$

Assuming that $\cos(i)$ is uniformly distributed, the probability p of a transit for a particular set of orbital parameters is

$$p = (R_\mathrm{p} + R_\mathrm{s})\frac{1+\epsilon\cos(\omega)}{a(1-\epsilon^2)}, \tag{1.3}$$

which favours large planets in tight orbits, faithfully represented by the population of transit exoplanets in figure 1.1. Dedicated space-based surveys by the Kepler Space Telescope (Koch et al., 2004) and the Transiting Exoplanet Survey Satellite (TESS) (Ricker et al., 2014) have found thousands of exoplanets, with a bias towards large planetary radii and small semi-major axes. Although highly successful missions, the sensitivity of our most advanced instruments to planetary transits, including the recently operational James Webb Space Telescope (JWST) (Sabelhaus & Decker, 2004), makes detecting Earth-mass exoplanets beyond the snow line prohibitive (Beichman et al., 2014; Kaltenegger & Traub, 2009).

The radial velocity method has also contributed significantly to the database of confirmed exoplanets. When a bound exoplanet has sufficient mass to cause its host star to orbit the planet-star barycenter at sufficient orbital velocity, observers on the Earth can detect a shift in the host's spectrum due to the Doppler effect when the star moves in the radial direction, towards or away from the observer (Wright, 2018). In the limit that the planet mass $M_{\rm p}$ is much less than the mass of the host start $M_{\rm s}$, the observed semi-amplitude K of the host's radial velocity is given by (Wright & Howard, 2009)

---

[1] A list of confirmed exoplanets is available at `https://exoplanetarchive.ipac.caltech.edu/`

$$K = M_{\rm p} \sin(i) \sqrt{\frac{G}{a(1-\epsilon^2)M_{\rm s}}}, \tag{1.4}$$

where P is the orbital period of the exoplanet. Compared to the transit method, the radial velocity method is less sensitive to orbital semi-major axis, but relies on a large mass ratio between the planet and its host to produce a measureable effect. This is once again borne out in figure 1.1, where we can see a large contribution to the exoplanet catalogue from the radial velocity method for the large mass regime beyond the snow-line, or indeed for planets in tighter orbits on the lower mass scale, where the host star is also of lower mass. Instruments such as the High Accuracy Radial-velocity Planetary Search (HARPS) project (Astudillo-Defru et al., 2017) can achieve precision measurements of $K < 1\text{ms}^{-1}$, although falls short of the $K \sim 10\text{cms}^{-1}$ precision required to detect and Earth analogue (Wright & Gaudi, 2013).

Direct imaging of exoplanets involves spatially resolving the light contribution from the exoplanet from that of its host star. Two sources of light contribute to the observed flux of an exoplanet, namely emissions directly from the planet as a result of internal temperature or heat absorbed from the host and reflected star light from its host off of the planet's surface or atmosphere. The Spectro-Polarimetic High contrast imager for Exoplanets REsearch (SPHERE) (Beuzit et al., 2019) instrument installed on the Very Large Telescope in Chile takes advantage of adaptive optics (van Kooten et al., 2020) to compensate for atmospheric turbulence, active optics (Hugot et al., 2012) and a coronagraph to block out host star light. Similarly, the Gemini Planet Imager (GPI) (Macintosh et al., 2006) on the Gemini South Telescope also employs adaptive optics to improve imaging quality and detect Jupiter mass exoplanets in $\sim 10\%$ of systems observed (McBride et al., 2011). In spite of the impressive suite of technology used by direct imaging surveys, exoplanets discovered by this method are restricted to the super Jupiter mass regime, although they are invariably discovered beyond the snow line where the contrast between star light and planet light is the lowest.

1.3 Microlensing Surveys

Microlensing can also be used as a probe of galactic structure (Zhao & Mao, 1996); in particular, the frequency and average timescale of events along various lines of sight in the sky can be used to inform models of stellar mass distribution and kinematics across the Galaxy. As the detectability of a microlensing event increases with the mass of the lens, we can attempt to reverse engineer the mass density of the Galaxy by analysing

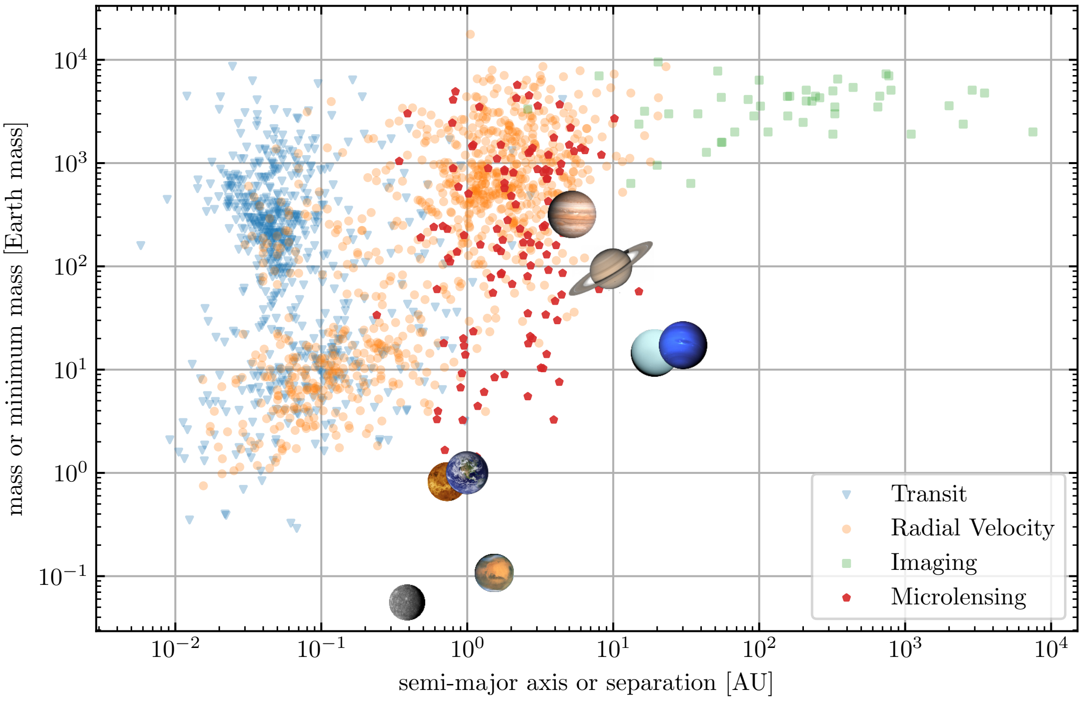

FIGURE 1.1: The planetary mass vs semi-major axis distribution of known exoplanets is shown on a logarithmic scale. Planets are indicated by markers determined by their detection type, with microlensing planets shown as red pentagons. The planets of the Solar system are shown graphically on top of exoplanet detections. The precise location of the snow line will depend on the mass of the host star; for microlensing, the average host mass is $\sim 0.4M_{\odot}$, found by taking the mean mass of exoplanet hosts from microlensing entries in the exoplanet archive. This puts the snow line at approximately 0.5AU, based on a typical stellar mass-temperature relation (Eker et al., 2015).

the results of microlensing surveys, taking care to correct for the detection efficiency for events of particular timescales and with sources of a particular observed brightness.

Among the most prolific of such microlensing surveys is the Optical Gravitational Lensing Experiment (OGLE), which has contributed much to microlensing science and our understanding of Galactic structure, beginning with OGLE-I from 1992 to 1995 (Udalski et al., 1992). A key result from the initial OGLE survey was reported by Udalski et al. (1994a), who found that the probability of microlensing for an individual source star, also known as the microlensing *optical depth*, was higher at $\sim 3 \times 10^{-6}$ than the purely theoretical estimates of $\sim 10^{-6}$ that had been made at the time (Paczynski, 1991). These initial results also confirmed the dominance of the Galactic bar as the main contributor to microlensing, with the Galactic disk providing approximately 5% of source stars. Over the years since, the OGLE mission has received multiple hardware upgrades and completed its second campaign, OGLE-II (Udalski et al., 1997) from 1997 to 2000, which also provided microlensing observations of the Megallanic clouds which were consistent with theoretical predictions (Wyrzykowski et al., 2010). The third campaign, OGLE-III (Udalski, 2003) began in 2001 and concluded in 2009 with results by Wyrzykowski et al. (2015) comparing the mean microlensing event timescale to that predicted by a simulation based on a Galactic model (Kerins et al., 2009) which exposed some discrepancies with the simulation and provided insight into the orientation and structure of the Galactic bar. The currently ongoing and final phase of the mission, OGLE-IV (Udalski et al., 2015), continues to provide important microlensing results and discoveries which will be discussed in chapter 2 in depth. The survey is also supported by the OGLE Early Warning System (EWS) which was first implemented in 1994 as a means of detecting ongoing microlensing events before reaching their peak magnification (Udalski et al., 1994b). For microlensing surveys, this ability provides a unique opportunity to coordinate observations across multiple telescopes in an effort to improve the sampling of the lightcurve (Jeong et al., 2015), as opposed to discovering the event months or years after the source flux has returned to its non-magnified baseline level.

Another key microlensing mission is the Microlensing Observations in Astrophysics (MOA) survey, which is comprised of two campaigns, namely the original MOA survey active for ten years from 1995 until 2005 and the ongoing MOA-II survey which began shortly after the end of the first campaign (Abe et al., 2008). MOA has yielded results consistent with OGLE (Sumi et al., 2003) from observations of the Galactic bar and has also performed observations of the Magellanic clouds (Muraki et al., 1999). Notably, work by Awiphan et al. (2016) compared results from the MOA-II survey (Sumi et al., 2013) to a simulation based on a more recent version of the Galactic model employed by Kerins et al. (2009) and found a deficit of $\sim 50\%$ in the event rate produced by the simulation in comparison to the empirical results from MOA-II.

The Korea Microlensing Telescope Network (KMTNet) is a more recent survey which began observations in 2015 with a primary science goal of detecting exoplanets in the vicinity of the Galactic bar(Kim et al., 2016). The network consists of three observatories: the South African Astronomical Observatory (SAAO), the Australian Siding Spring

Observatory (SSO) and the Cerro-Tololo Inter-American Observatory (CTIO) in Chile. Like the OGLE survey, KMTNet uses an early warning system to assist with observations (Kim et al., 2018a). This is particularly important, as obtaining a well sampled light curve is crucial when searching for exoplanets due to the smaller timescales of exoplanet signatures on the magnification variation (Gould & Loeb, 1992).

As with strong gravitational lensing, microlensing campaigns also offer an opportunity to investigate a possible source of dark matter. Massive Compact Halo Objects (MACHOs) represent a hypothetical population of dense objects with low or negligible luminosity, such as stellar remnants such as white dwarfs, or low mass stars such as red dwarfs, in orbit around the Milky Way's halo (Alcock et al., 1992). These objects, if they existed in large enough number to meaningfully contribute to dark matter, represent ideal candidates for lens objects for microlensing observations. Surveys investigating this phenomenon used source stars in the Magellanic clouds to detect these elusive objects, such as the initial phase of the first MOA campaign, as well as via the dedicated MACHO (Alcock et al., 2000) and EROS (Moniez, 2009) campaigns. Such missions have found optical depths on the order of 10^{-7}, a factor ten times lower than observed towards the Galactic bar, but if produced by a MACHO population, represents a MACHO population mass of $\sim 10^{11} M_{\odot}$. Such a large population of MACHOs is inconsistent with observations from the Hubble Space Telescope, which would detect the faint contributions of red and white dwarfs (Banerjee et al., 2003).

In addition to these dedicated microlensing campaigns, there have been multiple follow-up surveys which aid in exoplanet discovery by capitalising on event alert systems. The Microlensing Follow-Up Network (MicroFUN) (Yoo et al., 2004) is such a survey which principally focuses on high magnification events due to the sensitivity of such events to exoplanets, as explained in section 1.7. Similarly, the Probing Lensing Anomalies NETwork (PLANET) survey was a follow up survey which debuted with a pilot program in 1995 providing high cadence photometry to 11 MACHO and OGLE events, including a binary event MACHO-95-BLG-12 (Albrow et al., 1998). Working in concert with PLANET is the RoboNet-II robotic survey (Tsapras et al., 2009) which automatically searches microlensing alert systems for candidate events and prioritises events (Allan et al., 2006) for monitoring. Each of these follow up surveys provide additional sampling for microlensing events, allowing for more precise results.

1.4 The PSPL Model

When modelling the magnification of a background object, we must consider the nature of the lens, the source and the observer: is the lens a single object such as a star, or is it a system of lenses, such as a binary star or a star with a bound planet (Mao & Paczynski, 1991; Dominik, 1999)? Is the angular size of the source comparable to its closest approach to the lens, such that different parts of its surface receive an appreciably different magnification (Witt & Mao, 1994)? Is the relative velocity of the observer constant with respect to the lens-source system, or is the motion of the Earth around the Sun significant over

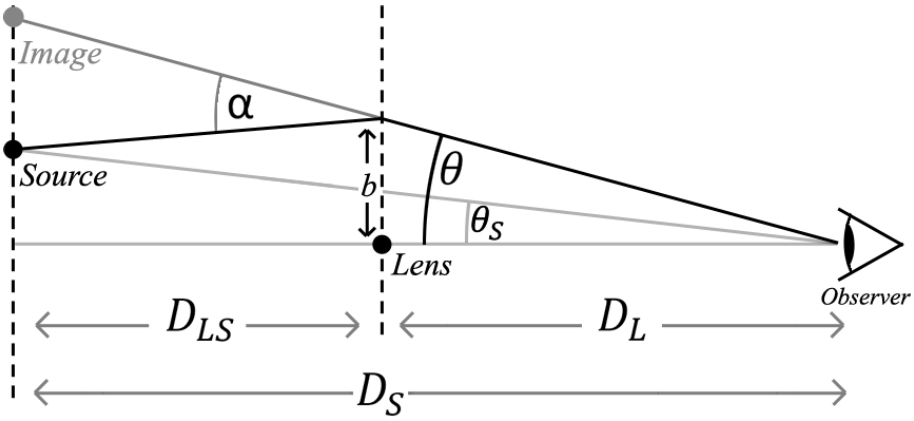

FIGURE 1.2: The microlensing schematic: an observer (on the right), views a source object at a distance D_S (on the left) undergoing a microlensing event by a lens object at a distance D_L (in the middle). The black line originating from the source is a light ray, which passes at a distance b from the lens, before being pulled towards the lens by its gravity and hence deflected by an angle α, sending it on a trajectory that intercepts the observer's location. The image of the source which the observer sees is the location in the source plane projected back along the light ray incident on the observer, shown on the top left. Note that the image of the source is not only displaced - it is also distorted in shape, which is not illustrated in this figure.

the course of the event (Alcock et al., 1995)? While each of these possibilities have been observed in nature, the simplest model of microlensing, known as the Paczyński model (Paczynski, 1986), which assumes a single point-like source, a single point-like lens, earning it an alternative name, the PSPL model (which is more often used and hence how it shall be referred to in this work), is by far the most used when modelling real events. As real events involve measuring the flux of the source star over time, any model, including the PSPL model must provide some calculation of magnification as a function of time t, typically denoted by $A(t)$.

Before deriving what $A(t)$ is in the PSPL model and indeed to provide a foundation to gravitational microlensing, we must first derive an important quantity - the angular Einstein radius θ_E. This is a quantity which depends on the mass M of the lens, the distance D_L to the lens and the distance D_S to the source through

$$\theta_\mathrm{E} = \sqrt{\frac{4GM}{c^2}\frac{D_\mathrm{S}-D_\mathrm{L}}{D_\mathrm{S}D_\mathrm{L}}}. \tag{1.5}$$

It represents the radius of a circle on the sky, centred on the lens and characterises the strength of the lensing effect, with larger Einstein radii not only increasing the magnification of the source at some fixed angular separation from the lens, but also increasing the likelihood of the event taking place due to the larger area in the sky over which a microlensing event can take place while also being detected by our telescopes. With this in mind, we can now consider the angular position of the source's image after being distorted by the gravitational lens. The layout of the source-lens-observer system is shown in figure 1.2, where we can see illustrated the deflection angle α from equation 1.1. Under the small angle approximation, we can relate the angular location of the source θ_S to the angular location of the image θ using

$$\theta D_{\mathrm{S}} = \theta_{\mathrm{S}} D_{\mathrm{S}} + \alpha (D_{\mathrm{S}} - D_{\mathrm{L}}). \tag{1.6}$$

This can be transformed further, using equations 1.5 and 1.1 to acquire

$$\theta D_{\mathrm{S}} = \theta_{\mathrm{S}} D_{\mathrm{S}} + \frac{\theta_{\mathrm{E}}^2 D_{\mathrm{S}}}{\theta}, \tag{1.7}$$

$$\theta^2 - \theta_{\mathrm{S}}\theta - \theta_{\mathrm{E}}^2 = 0, \tag{1.8}$$

which can then be solved using the quadratic formula to get

$$\theta = \frac{1}{2}\left(\theta_{\mathrm{S}} \pm \sqrt{\theta_{\mathrm{S}}^2 + 4\theta_{\mathrm{E}}^2}\right). \tag{1.9}$$

Equation 1.9 gives us two important details. Firstly, as it allows us to perform a coordinate transform, we can use it to calculate the ratio of the final image area to the original, un-distorted image area (and hence provide $A(\theta_{\mathrm{S}})$) and secondly, we can see that there are two solutions, $\theta_{\pm}$ to this equation, courtesy of the positive and negative square roots. These two solutions are both important, as they imply that the distorted image of the source actually has two copies, one outside the Einstein radius (positive root) and one inside the Einstein radius, on the opposite side of the lens to the source (negative root). If we want to find the final magnification of the lensing effect, we will need to sum the contributions of both images. Before doing so, it is important to consider the quantities that are measurable from the microlensing lightcurve. Unfortunately, without further information (which will be discussed in subsequent sections), neither the lens mass nor the lens distance is known and consequently θ_{E} is also unknown. As such, equation 1.9 can be normalised to θ_{E} to give $u_{\pm} = \frac{\theta}{\theta_{\mathrm{E}}}$ and $u = \frac{\theta_{\mathrm{S}}}{\theta_{\mathrm{E}}}$, yielding

$$u_{\pm} = \frac{1}{2}\left(u \pm \sqrt{u^2 + 4}\right). \tag{1.10}$$

We should now consider how the areas of the lensed and un-lensed images of the source compare to acquire the magnification. Note that the surface brightness of the star is conserved in the image and as such, the magnification only depends on the area of the image relative to the un-lensed source. In figure 1.3, we can see the scenario illustrated for the positive solution (the image external to the Einstein radius) in polar coordinates, with ϕ as the angular coordinate. The size of the infinitesimal unit area, which shall represent our un-lensed source in polar coordinates is given by

$$d\sigma = u du d\phi, \tag{1.11}$$

and the area of the image by

$$d\sigma_{\pm} = u_{\pm} du_{\pm} d\phi, \tag{1.12}$$

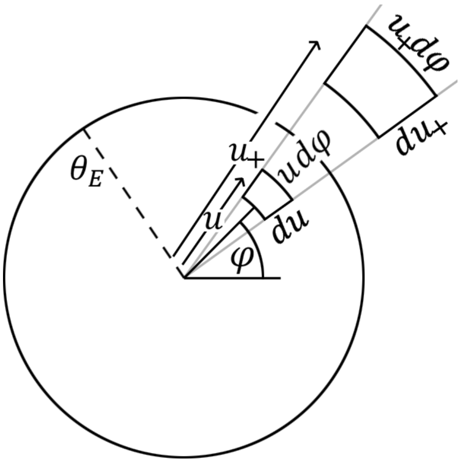

FIGURE 1.3: The shape of an infinitesimal unit area in polar coordinates at a distance u from the lens is shown, where in this case $u < 1$, as it is interior to the Einstein radius, shown a circle of radius θ_E centred on the lens. The equivalent area for the positive solution to equation 1.10 is shown further out from the lens, outside the Einstein radius at a distance u_+. It has a radial side length of du_+ and an azimuthal side length of $u_+ d\phi$, as opposed to the original pre-lensing area which has a radial side length du and azimuthal side length of $ud\phi$, which is smaller than its lensed counterpart. The negative solution is not shown here; it would be 180° out of phase with the positive solution, but would lie inside the Einstein radius.

with the magnification given simply by the sum of the ratio of the areas of both solutions, (keeping in mind that we want the positive area of the negative solution, requiring a minus sign to compensate)

$$A(u) = \frac{u_+}{u}\frac{du_+}{du} - \frac{u_-}{u}\frac{du_-}{du}. \tag{1.13}$$

Calculating the derivative of equation 1.10 gives us what we need,

$$\frac{du_\pm}{du} = \frac{1}{2}\left(1 \pm \frac{u}{\sqrt{u^2+4}}\right), \tag{1.14}$$

$$A(u) = \frac{1}{4u}\left(2u + \sqrt{u^2+4} + \frac{u^2}{\sqrt{u^2+4}}\right) - \frac{1}{4u}\left(2u - \sqrt{u^2+4} - \frac{u^2}{\sqrt{u^2+4}}\right), \tag{1.15}$$

$$A(u) = \frac{u^2+2}{u\sqrt{u^2+4}}. \tag{1.16}$$

The final step is to parameterise the normalised angular separation as a function of time. We must introduce three important parameters that are necessary to describe any microlensing light-curve. Firstly, the minimum normalised impact parameter u_0 quantifies the closest angular approach of the source to the lens, normalised to θ_E and controls the magnification. Secondly, the time of closest approach t_0, usually expressed in Julian days or modified Julian Date (MJD) represents the time of maximum magnification. Finally, the Einstein radius crossing time t_E represents the time taken for the source to travel

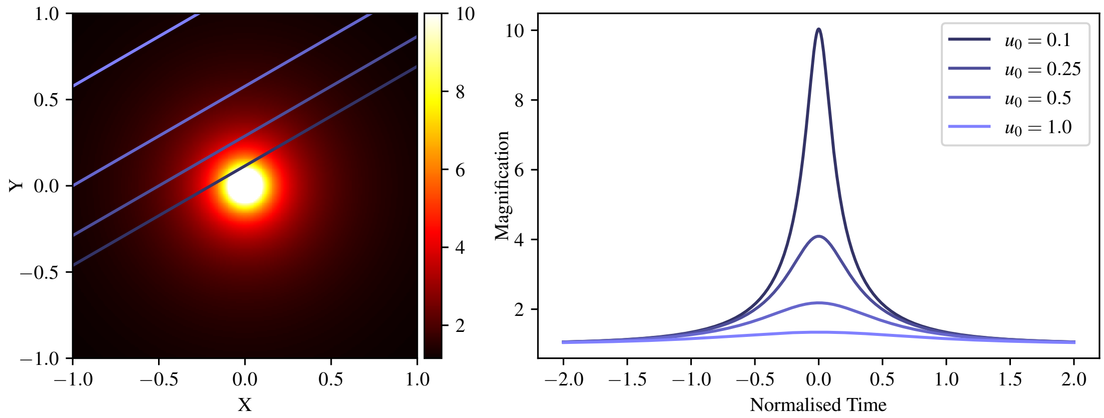

FIGURE 1.4: On the left is the PSPL magnification map, centred at $(X,Y) = (0,0)$ on the lens. The magnification climbs rapidly close to the lens, with $A(u) \approx \frac{1}{u}$ for small u. Four examples of source trajectories are shown, differentiable by their impact parameters of $u_0 = 0.1, 0.25, 0.5, 1.0$. On the right, the corresponding lightcurves are shown.

an angular distance of θ_E on the sky relative to the lens and can be expressed in terms of the lens-source relative proper motion μ_rel as

$$t_\mathrm{E} = \frac{\theta_\mathrm{E}}{\mu_\mathrm{rel}}. \tag{1.17}$$

The impact parameter u can thus be expressed, using Pythagoras' theorem, in terms of these three quantities through

$$u(t) = \sqrt{u_0^2 + \left(\frac{t - t_0}{t_\mathrm{E}}\right)^2}. \tag{1.18}$$

The shape of the PSPL lightcurve is obtained by substituting in the expression for u from equation 1.18 into $A(u)$ from equation 1.16 with examples shown in figure 1.4. While the PSPL model is a popular one, without the presence of first order effects in the lightcurve, we cannot extract important quantities such as the lens mass, D_L or μ_rel individually. Now, we must turn our attention to some departures from the PSPL model which can help us extract extra information from the lensing system.

1.5 Finite Source Effects

When examining equation 1.16, one notices the singularity at $u = 0$, where the magnification is formally infinite. Indeed for small impact parameters, the magnification is given approximately by

$$A(u) \approx \frac{1}{u}, \qquad u \ll 1. \tag{1.19}$$

This happens because when a point source lies perfectly behind a point lens with respect to the observer, the source is distorted into a ring which traces the angular Einstein radius. As an analogy to understand how the microlensing magnification behaves as the

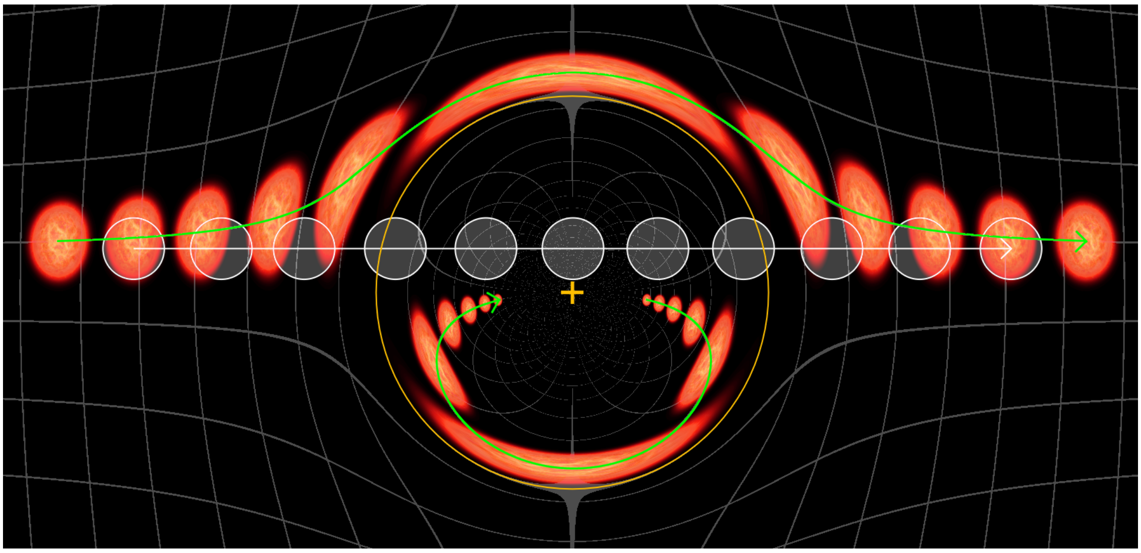

FIGURE 1.5: A simulated view of a red giant star, with a source radius one fifth of the Einstein radius, is shown undergoing gravitational microlensing. The many copies of the star are distributed horizontally to show the effect of the lensing at different locations along its journey. The white circles represent the actual, un-lensed location of the source. The orange + sign represents the location of the lens, with its Einstein radius indicated by the orange circle. The white arrow pointing to the right is the actual trajectory of the source relative to the lens and passes within one quarter of an Einstein radius of the lens (i.e. $u_0 = 0.25$). There are two green arrows; the one passing above and exterior to the Einstein radius corresponds to the lensed trajectory of the positive solution of equation 1.10, while the highly curved green arrow, completely contained within the Einstein radius, corresponds to the negative solution. A gray grid is shown beneath to illustrate the warping of the Cartesian coordinates around the lens.

impact parameter approaches zero, consider a scenario whereby an alien civilization uses a powerful circular radio transmitter, aimed at observers on the Earth, such that it lies directly behind a stellar mass lens from our vantage point, similar to the situation analysed by Maccone (2009). Although such a transmitter may have an incredibly small angular size, its finite nature will inevitably prevent an infinite magnification in the case of perfect alignment. If the transmitter has a physical radius R_S, it will have an angular size given by

$$\theta_* = \frac{R_\mathrm{S}}{D_\mathrm{S}}, \tag{1.20}$$

which in the context of microlensing, can be normalised to the angular Einstein radius as the parameter ρ,

$$\rho = \frac{\theta_*}{\theta_\mathrm{E}}. \tag{1.21}$$

When directly behind the lens, the primary and secondary images of the transmitter join together to produce a ring of a thickness dependent on ρ in normalised angular space. From equation 1.10, we can find the outer and inner radius of this ring by using the value of ρ for the positive and negative solutions, respectively. The finite source magnification for $u = 0$, assuming a uniform surface brightness, is then given by the ratio of the area a' of this "Einstein ring" to the original area a_0 of the source

$$a' = \pi\rho\sqrt{\rho^2 + 4}, \tag{1.22}$$

$$a_0 = \pi\rho^2 \tag{1.23}$$

$$A_\mathrm{FS}(u = 0) = \sqrt{1 + \frac{4}{\rho^2}}. \tag{1.24}$$

If we assume the aforementioned aliens have advanced technology and have constructed a vast transmitter 1,000km in diameter at a distance of 8kpc and are using a lens of $0.5M_\odot$ at a distance of 4kpc, we would expect an angular Einstein radius of $\theta_\mathrm{E} \sim 0.7$mas, an angular source radius of $\theta_* \sim 4.2 \times 10^{-7}$mas and a magnification of 3.4×10^6.

In general, when $\rho \approx u$ or $\rho > u$, we will notice that the magnification deviates significantly from what equation 1.16 predicts. In figure 1.5, we can see an example of the finite source effect in action, with $\rho = 0.2$. The magnification $A(u)$ must now be integrated over the profile of the source, which ultimately avoids the singularity at $u = 0$ for the PSPL model. Unfortunately, there is no analytical form for $A(u)$ in the finite source scenario $A_\mathrm{FS}(u)$, but we can make some progress by expressing the problem in integral form,

$$A_\mathrm{FS}(u) = \frac{1}{S_0}\int_0^{\rho}\int_0^{2\pi} S(u', \theta)A(U(u, u', \theta))u'du'd\theta, \tag{1.25}$$

$$S_0 = \int_0^{\rho} \int_0^{2\pi} S(u', \theta) u' du' d\theta, \tag{1.26}$$

$$U(u, u', \theta) = \sqrt{(u + u' \cos\theta)^2 + (u' \sin\theta)^2}, \tag{1.27}$$

where S_0 is the source intensity profile $S(u', \theta)$ integrated over the circular source given by equation 1.26 and $U(u, u', \theta)$ is the impact parameter of a particular part of the source, parameterised in polar coordinates by u' and θ, with the center of the source at a distance u away in normalised space as described in equation 1.27.

For the source intensity profile, two common options are used: the uniform disk, with $S(u', \theta) = 1$, which is a good approximation if the finite source effect is weak, with the second option being a linear limb darkening profile, characterised by a linear limb-darkening coefficient β via

$$S(u') = 1 - \beta\left(1 - \sqrt{1 - \left(\frac{u'}{\rho}\right)^2}\right). \tag{1.28}$$

Limb-darkening effects arise from the optical depth of stellar atmospheres, with the observer seeing deeper into the star where the atmosphere is hotter and hence brighter near the centre of the star's profile, while only penetrating to shallower depths near the edge of the star's profile, where temperatures are cooler, yielding a lower surface brightness. Equation 1.28 is often necessary to employ when fitting models to light-curves with strong finite source effects, as it can alter the estimation of ρ. Strong limb-darkening effects concentrate the source intensity near the center of the source, resulting in an underestimation of ρ with the uniform disk assumption.

An array of numerical methods has been developed to evaluate $A_{\mathrm{FS}}(u)$, with the method described in Lee et al. (2009) being used in this work. Assuming a value of ρ can be accurately determined from the light-curve photometry, we can use information about the source star to acquire θ_{E}. Stellar effective temperature T_{eff} and radius can be calculated from stellar colour, such as the Johnson-Cousins B-V (Sekiguchi & Fukugita, 2000; Boyajian et al., 2012), correcting for interstellar extinction, which allows an estimation of stellar luminosity through $L_{\mathrm{S}} = 4\pi R_{\mathrm{S}}^2 \sigma_{\mathrm{SB}} T_{\mathrm{eff}}^4$. Coupling this with a measurement of apparent magnitude m_{S}, we can acquire the distance to the source D_{S} using the distance modulus commonly used in astronomy,

$$m_{\mathrm{S}} - M_{\mathrm{S}} = 5\log(D_{\mathrm{S}}) - 5, \tag{1.29}$$

$$M_{\mathrm{S}} = M_{\odot} - 2.5\log\left(\frac{L_{\mathrm{S}}}{L_{\odot}}\right), \tag{1.30}$$

$$D_{\mathrm{S}} = 10^{\frac{1}{5}(m_{\mathrm{S}} - M_{\mathrm{S}} + 5)}, \tag{1.31}$$

where $M_\odot$ and $L_\odot$ are the solar absolute magnitude and luminosity respectively. Now that we have a measurement of D_S, equation 1.21 can now be reversed to acquire the Einstein radius, the first of two ingredients required to extract a mass measurement from equation 1.5. In order to fully break the microlensing degeneracy, we need to acquire the next parameter, D_L the distance to the lens, which can be determined from either the lens flux which is typically too small to observe[2] or the microlensing parallax effect. With an accurate estimation of D_L, the lens mass can then be fully resolved.

1.6 Microlensing Parallax

Although the distances to microlensing lenses and sources is typically on the order of kiloparsecs, the physical Einstein radius at the distance of the lens is typically comparable to an astronomical unit. This has an important implication in two distinct scenarios: firstly, if the timescale of the event is comparable to a year, then the Earth's motion around the Sun could result in a breakdown of the rectilinear assumption of the lens-source trajectory discussed in section 1.4. Secondly, if one were to observe the same microlensing event at two different locations in the Solar system, there could also be a noticeable offset in t_0, the time of peak magnification, as well as u_0, the normalised closest approach of the source to the lens. The magnitude of each of these effects depends on the distance to the lens D_L, although the offset in t_0 is primarily affected by the Earth-Sun separation projected onto the line of sight to the event. As such, measurements of these parameter offsets can lift the microlensing degeneracy and yield a mass measurement of the lens.

1.6.1 Earth motion parallax

The former case is known, aptly, as Earth-motion parallax and is the most common form of microlensing parallax observed in the literature, such as several cases of possible stellar remnant lenses in Wyrzykowski et al. (2016), from the OGLE-III survey. It involves introducing a normalised projection of the Earth's location relative to the Sun, to the rectilinear motion of the lens as assumed in equation 1.18. To begin with, we define the microlensing parallax π_E as

$$\pi_\mathrm{E} = \frac{a_\oplus}{\theta_\mathrm{E}} \frac{D_\mathrm{S} - D_\mathrm{L}}{D_\mathrm{S} D_\mathrm{L}} = \frac{a_\oplus}{\tilde{r}_\mathrm{E}}, \tag{1.32}$$

where $a_\oplus$ is the semi-major axis of the Earth (Gould, 2000). As well as π_E, we need to define some more terms to allow the geometric projection of the Earth's orbit into the lens-source reference frame. Firstly, the source star's latitude relative to the plane of the Solar system is parameterised in ecliptic coordinates as γ. For the longitude, we shall use the angle subtended by the Earth's current location and its location at $t = t_0$ from

---

[2] Measurements of the lens flux have been made which have been used to further constrain the value of D_L, such as in Koshimoto et al. (2017), where an exoplanet of mass $35^{+17}_{-9} M_\oplus$ was reported.

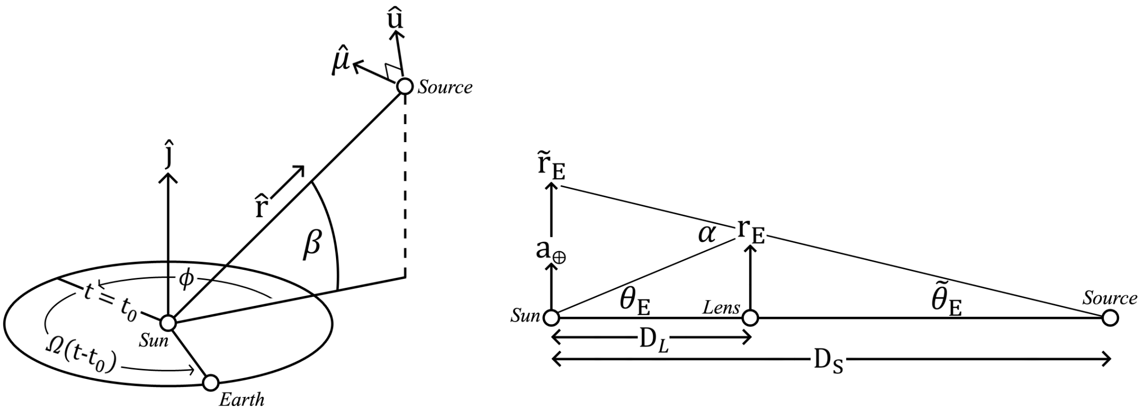

FIGURE 1.6: Shown is the setup for Earth motion parallax. On the left is shown the solar-system view, where we can see the Earth in its orbit around the Sun, shown at the center. The source lies at an ecliptic latitude β, with a direction vector $\hat{r}$. At a time $t = t_0$, the projection of $\hat{r}$ onto the ecliptic subtends an angle ϕ with the Earth. For any other time, the Earth has moved around its orbit by an angle $\Omega(t - t_0)$. The normal of the ecliptic plane is denoted by $\hat{j}$. The vector $\hat{\mu}$ is parallel to the lens-source relative proper motion $\mu_{\rm rel}$, while the vector $\hat{u}$ is parallel to the lens-source separation at closest approach, projected onto $\hat{r}$. On the right, we see the full observer-lens-source system. The value $\tilde{r_{\rm E}}$ represents the physical Einstein radius $r_{\rm E}$ projected back onto the observer plane.

the Sun. This is given by $\Omega(t - t_0)$[3], where Ω is the angular velocity of the Earth's orbit around the Sun, $\Omega = \frac{2\pi}{1\rm year}$, with an angle ϕ also added to account for the angular offset of the Sun-source axis projected onto the ecliptic, as shown in figure 1.6.

The kinematics of the lens-source system is parameterised by two orthogonal vectors, namely the normalised relative proper motion $\hat{\mu}$ and the normalised minimum impact parameter $\hat{u}$. With this in mind, we can express the impact parameter of the source to the lens relative to the Earth as

$$\vec{u}_{\oplus} = \hat{u}u_0 + \hat{\mu}\frac{t - t_0}{t_{\rm E}} + \pi_{\rm E}\Big(\hat{u}\cos\big(\Omega(t - t_0) + \phi\big) + \Lambda\hat{\mu}\sin\big(\Omega(t - t_0) + \phi\big)\Big), \tag{1.33}$$

where Λ is the parity, given by $\Lambda = \hat{j} \cdot (\hat{\mu} \times \hat{u})$ and $\hat{j}$ is the vector normal to the ecliptic plane and takes a value $\pm\sin(\gamma)$, where the sign depends on the lens-source trajectory. The final step to acquiring the Earth motion parallax model is to calculate the length of $\vec{u_{\oplus}}$,

$$\begin{aligned} u_{\oplus}{}^2 = u_{\odot}{}^2 + 2\pi_{\rm E}\Bigg(u_0\cos\big(\Omega(t - t_0) + \phi\big) + \frac{t - t_0}{t_{\rm E}}\Lambda\sin\big(\Omega(t - t_0) + \phi\big)\Bigg) \\ + \pi_{\rm E}{}^2\Bigg(\cos^2\big(\Omega(t - t_0) + \phi\big)(1 - \Lambda^2) + \Lambda^2\Bigg), \end{aligned} \tag{1.25}$$

---

[3] This assumes a constant angular velocity of the Earth around the Sun in a circular orbit. In reality, the Earth's orbit is elliptical with an eccentricity of $\epsilon = 0.0167$, introducing a small correction of $2\epsilon\sin(\Omega(t - t_0))$. Depending on the sensitivity of the survey and the alignment of the lens and source, this correction can improve a parallax fit when the Earth-Sun axis is aligned with the projection of $\hat{r}$ onto the ecliptic, although this correction is not propagated to the actual Earth-Sun separation, where it is negligible (Buchalter & Kamionkowski, 1997).

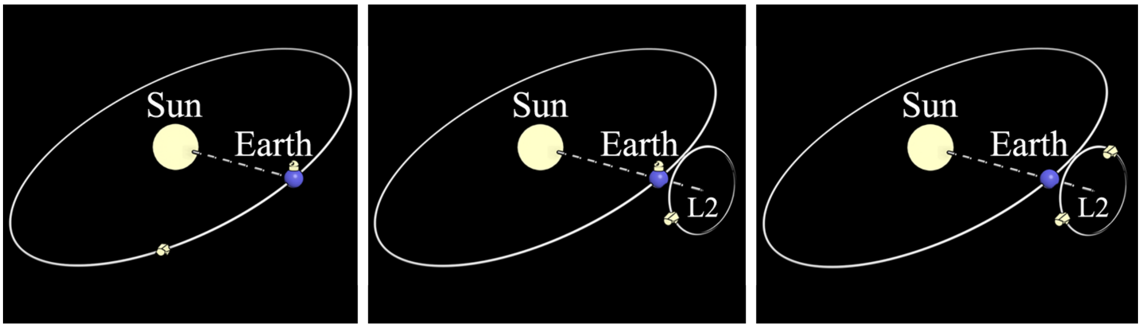

FIGURE 1.7: Artists impression of several configurations for a space-based parallax scenario. In each diagram, we can see the Sun and Earth indicated with yellow and blue spheres, respectively, as well as the Earth's orbit shown as a thin white line. On the left is shown the case where a parallax measurement could come from a baseline between an Earth based observatory, shown on the top of the Earth and a space-based observatory, shown trailing the Earth in its orbit. The middle diagram shows a similar scenario, but with the space-based observatory orbiting the Earth-Sun L2 Lagrange point in a halo orbit (Howell, 1984), shown as a smaller orbit perpendicular to the Sun-Earth axis. A third possibility is shown on the right, with two space-based observatories orbiting L2.

where $u_\odot$ is the impact parameter from the Sun's reference frame, which is identical to equation 1.18. Analysing equation 1.25 we can see that the only unknown parameter is the microlensing parallax π_E, while most other parameters can be calculated once the location of the source is known, which is independent of the microlensing event parameters. The PSPL parameters are usually known sufficiently well by casual observation of the light-curve to allow a good first approximation to the fitting process.

1.6.2 Space-based parallax

The other mechanism for producing microlensing parallax is via space-based parallax, which relies on a projected baseline between different observatories large enough to produce a measurable difference in t_0 and u_0 between each measured lightcurve. Typically, this has been done by comparing lightcurves from a space-based observatory and a ground-based observatory, such as presented in Yee et al. (2015), which discovered a $0.23 \pm 0.07 M_\odot$ mass lens in the Galactic disk using photometry from the Spitzer Space Telescope and OGLE-IV survey, from the event OGLE-2014-BLG-0939.

To parameterise the space-based parallax, π_E is broken down into perpendicular components $\pi_{\mathrm{E,E}}$ and $\pi_{\mathrm{E,N}}$ respectively, where the E and N subscripts refer to the components of π_E projected onto the Northern and Eastern vectors in the Equatorial coordinate system (Han et al., 2016). Casting the parallax vector into a coordinate system independent of the lensing parameters and kinematics allows us to consider the parallax contribution from both Earth motion and the baseline between two space-based observatories, or between a space-based and ground-based observatory. Three possible scenarios are shown in figure 1.7, some of which will be explored further in chapter 3.

1.7 Binary Lensing

So far, we have discussed the PSPL model and a few deviations involving the nature of the source, via finite source effects and the introduction of non-rectilinear trajectories resulting from the parallax effect. In none of these first order phenomena has the nature of the lens changed. In reality, this is sufficient to describe most lenses, but breaks down in a few scenarios; many stars in the Milky Way exist in binary systems (El-Badry et al., 2021) and most stars likely host bound exoplanets (Cassan et al., 2012). In some cases this is insufficient to introduce deviations from a point-lens model, such as where the angular separation of the two lenses is too large, allowing for a PSPL model to be used for a single component, or conversely, if the angular separation is too small compared to the impact parameter of the source at closest approach, causing the lens to behave like a single massive object. In some cases however, neither scenario applies and we must employ a binary lensing model, which introduces an astigmatism to the normally circularly symmetric gravitational potential of a single lens. This astigmatism manifests in the form of microlensing caustics, which represent the family of locations in the source plane where a point source would formally be magnified infinitely. In the PSPL case, the caustic is a single point directly behind the lens, leading to the singularity discussed in section 1.5. For multiple lens systems, the caustic takes on a more complicated structure. Not all complexity is the same however; trinary or multiple lenses are computationally expensive to model and have many different topologies, while a binary lens is symmetrical about the binary axis and comes in three different topologies, the close, resonant and wide structures (Tsapras, 2018).

The particular topology of the binary lens depends on only two parameters, the mass ratio q of the secondary to the primary lens and the separation s of the primary to the secondary lens, normalised to θ_{E} computed from the total system mass. In the case where q is small, such as for a stellar primary lens with a planetary secondary lens, the close topology will appear for $s < 1$, while the wide topology will be produced for $s > 1$. For heavier secondary lenses, a window in the s parameter space opens up around $s = 1$ allowing for the resonant topology to exist. Specifically, the boundaries between the close-resonant s_{c} and resonant-wide s_{w} topologies are given by (Cassan, 2008)

$$s_{\mathrm{c}}^{8} = \frac{(1+q)^{2}}{27q}\left(1 - s_{\mathrm{c}}^{4}\right)^{3}, \tag{1.34}$$

$$s_{\mathrm{w}}^{2} = \frac{\left(1 + q^{\frac{1}{3}}\right)^{3}}{1+q}. \tag{1.35}$$

The 2-dimensional magnification maps for examples of each topology, along with the topology boundary lines defined in equations 1.34 and 1.35, are showcased in figure 1.8. We can see from that diagram how the caustics manifest as sudden and discontinuous increases in magnification, bounding regions of high magnification relative to their exterior. The significance of these regions lies in the number of images of the source produced

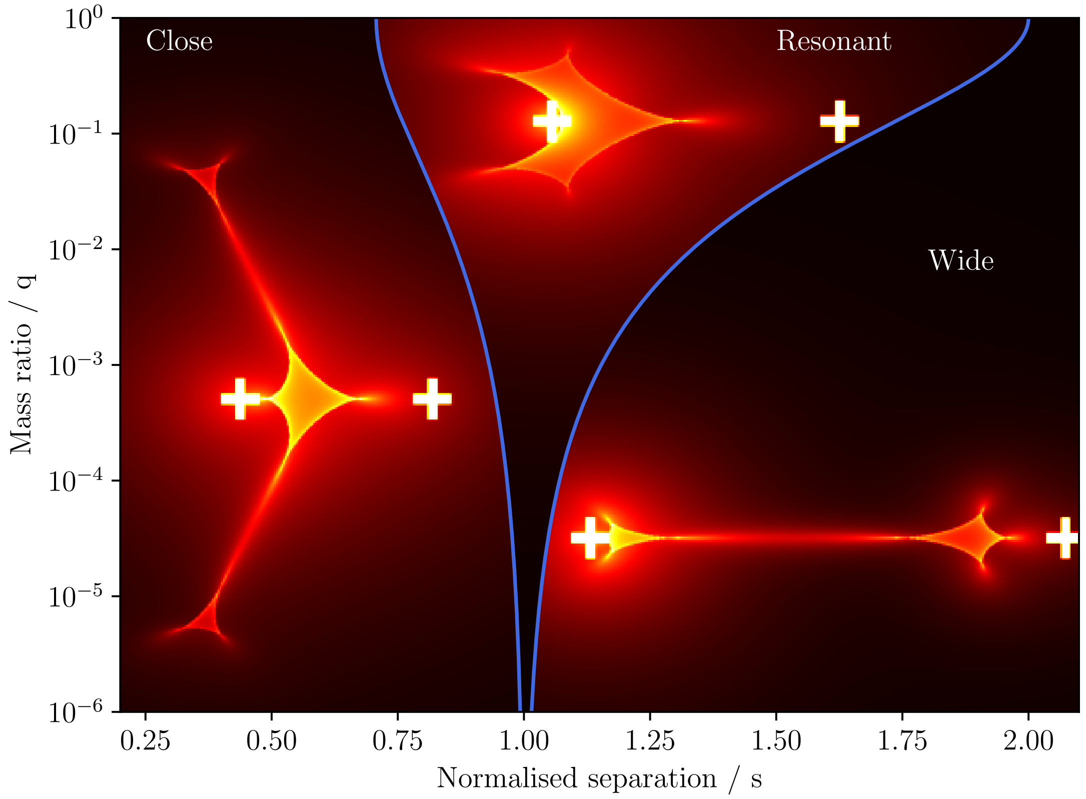

FIGURE 1.8: Shown are examples of the magnification maps of the close, resonant and wide binary topologies, from left to right, in the s, q parameter space. The blue lines represent the boundaries between the topologies, defined in equations 1.34 and 1.35. The location of the lenses for each case are indicated with white crosses.

when the source passes over them; when the source crosses a caustic into a higher magnification region, a new pair of images is created. Similarly, as the source leaves the higher magnification region, a pair of images merge together and disappear, dropping the magnification back down. This is illustrated in a resonant topology example in figure 1.9, where a merged pair of new images is created at the caustic entry, which subsequently split into distinct images when the source is fully inside the caustic, followed by two images merging back together as the source begins to leave the caustic which then disappear once more as the source fully exits.

The effect of binary lensing on a lightcurve can be significant. In the case where the secondary lens is a bound planet, with $q < 10^{-2}$ or less, the caustics can enable a detection through multiple means. The most obvious is the crossing of the caustic, which results in a sudden increase in the observed flux of the source, which is intuitive when interpreting the microlensing lightcurve as a 1-dimensional slice of the 2-dimensional magnification map. This can often be difficult to achieve, however, as the size of the secondary (or in this case *planetary*) caustic is proportional to $\sqrt{q}$. When q is of order $10^{-6} \rightarrow 10^{-5}$, the likelihood of the source passing over the planetary caustic becomes small. In that instance, we can instead rely on *magnification arms*; these are regions of higher magnification extending from a cusp of a secondary caustic to a corresponding cusp on the primary caustic and exist for both the close and wide topologies (figure 1.8 shows good examples of magnification arms for both topologies). While magnification arms do not produce as large a signal as caustics themselves, the source is more likely to pass over them due to their size. A final boon to detectability comes from the cusps, which project regions of higher magnification outward from the caustic, much like magnification arms, although their size is comparable to the caustic structures they belong to.

A use case of binary microlensing will be explored in chapter 4, where a binary model will be used to describe a real lightcurve produced by an array of telescopes, including Kepler, for an event detected in 2016. A more in-depth mathematical analysis of caustics and the evaluation of multi-lens magnification maps will likewise be explored in chapter 5.

1.8 Astrometric Microlensing

While most microlensing observations rely on photometric variations as the lens passes by the source, one can extract additional information about a microlensing event by monitoring the astrometric shift of the centroid of the source image pixels relative to its proper-motion trajectory. Microlensing surveys have already had the ability to detect source positions to micro-arcsecond precision (Dominik & Sahu, 1998), with upcoming space observatories showing even more promise in this regard (Nucita et al., 2017), making astrometric microlensing a useful tool in the large survey era of microlensing over the coming decade.

In the frame of reference of the lens, the position vector of the source is given by

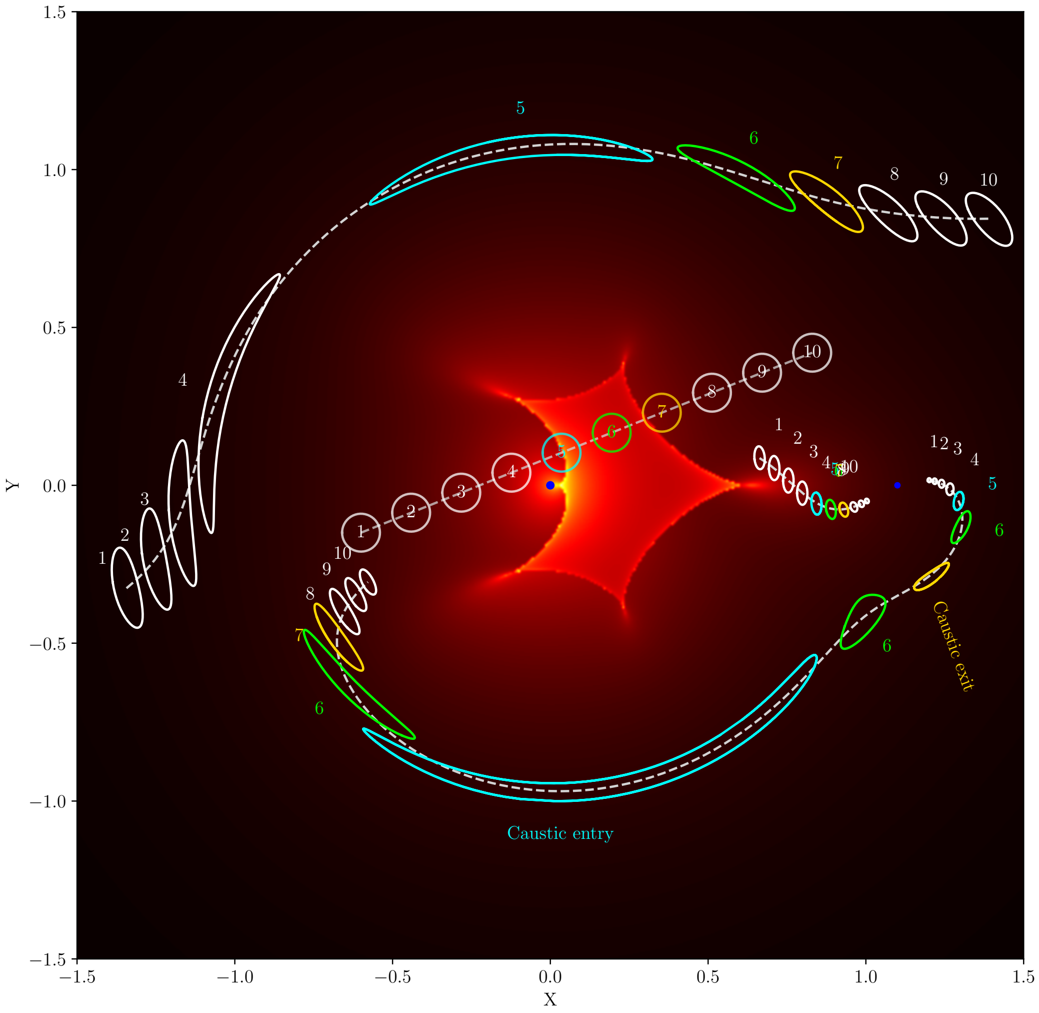

FIGURE 1.9: Shown above is an example of the magnification map (shown on a logarithmic scale) of a resonant binary caustic topology. The primary lens is shown as a blue circle centred on $(0, 0)$, with the secondary lens shown as a smaller blue circle to the right at $(1.1, 0)$. Overlayed on top of the magnification map are the trajectories of the lensed source images (curved trajectories) and trajectory of the real unlensed source (straight line trajectory). On top of the source and image trajectories are shown the outlines of the source at successive intervals in time, labelled $1 \rightarrow 10$. The caustic entry is indicated with the cyan circle, the exit with a golden circle and the interior passage with a green circle, with all other times wholly exterior to the caustic in white. Note the number of images in each case: exterior to the caustic, only three images of the source exist; the entry and exit produces four images and the caustic interior produces five images. To aid in understanding this complicated visualisation, note that the straight line trajectory across the centre with the perfectly circular sources would not be observed during the lensing - this is simply a visual aid to show where the source actually is behind the lens during the event.

$$\boldsymbol{u}(t) = \left(\frac{t - t_0}{t_{\mathrm{E}}}\right)\hat{\boldsymbol{\imath}} + u_0\hat{\boldsymbol{\jmath}}, \tag{1.36}$$

where $\hat{\boldsymbol{\imath}}$ is the unit vector parallel to the relative proper-motion vector μ_{rel} and $\hat{\boldsymbol{\jmath}}$ is the unit vector perpendicular to the trajectory. During a PSPL lensing event, the mean position of the source's image $\boldsymbol{u}'(t)$ is given by the magnification weighted sum of its primary and secondary image locations, $\boldsymbol{u}_+$ and $\boldsymbol{u}_-$ respectively, via

$$\boldsymbol{u}'(t) = \frac{A_+(t)\boldsymbol{u}_+(t) + A_-(t)\boldsymbol{u}_-(t)}{A(t)}, \tag{1.37}$$

$$\boldsymbol{u}_\pm(t) = \left(1 \pm \sqrt{1 + \frac{4}{u(t)^2}}\right)\frac{\boldsymbol{u}(t)}{2}, \tag{1.38}$$

$$A_\pm(t) = \frac{1}{2}\left(\frac{u^2 + 2 \pm u\sqrt{u^2+4}}{u\sqrt{u^2+4}}\right), \tag{1.39}$$

where equations 1.38 and 1.39 follow from the derivation for the PSPL magnification in equations 1.10 and 1.18. The centroid offset from the non-magnified source is then simply

$$\boldsymbol{\Delta}(t) = \boldsymbol{u}'(t) - \boldsymbol{u}(t), \tag{1.40}$$

$$\Delta_x = \frac{t - t_0}{t_{\mathrm{E}}\sqrt{u(t)^2 + 2}}, \tag{1.41}$$

$$\Delta_y = \frac{u_0}{\sqrt{u(t)^2 + 2}}. \tag{1.42}$$

Using this PSPL assumption, the centroid offset will, over the duration of the event, trace out an ellipse with a semi-major axis a and semi-minor axis b given by

$$a = \frac{1}{2\sqrt{{u_0}^2 + 2}}, \tag{1.43}$$

$$b = \frac{u_0}{2({u_0}^2 + 2)}, \tag{1.44}$$

which assuming both a and b can be accurately measured, allows for a determination of the minimum impact parameter,

$$u_0 = \frac{b}{2a^2}. \tag{1.45}$$

Introducing first order effects such as a finite source model has a noticeable impact on the offset track's shape, causing it to deviate from an ellipse and instead form a clover-like shape as the impact parameter shrinks; this represents another independent method of measuring finite source effects from a microlensing event. In the case where the lens system is a binary, the sudden appearance and disappearance of source images as the source passes over a caustic can cause the centroid offset to jump to a new location in Δ

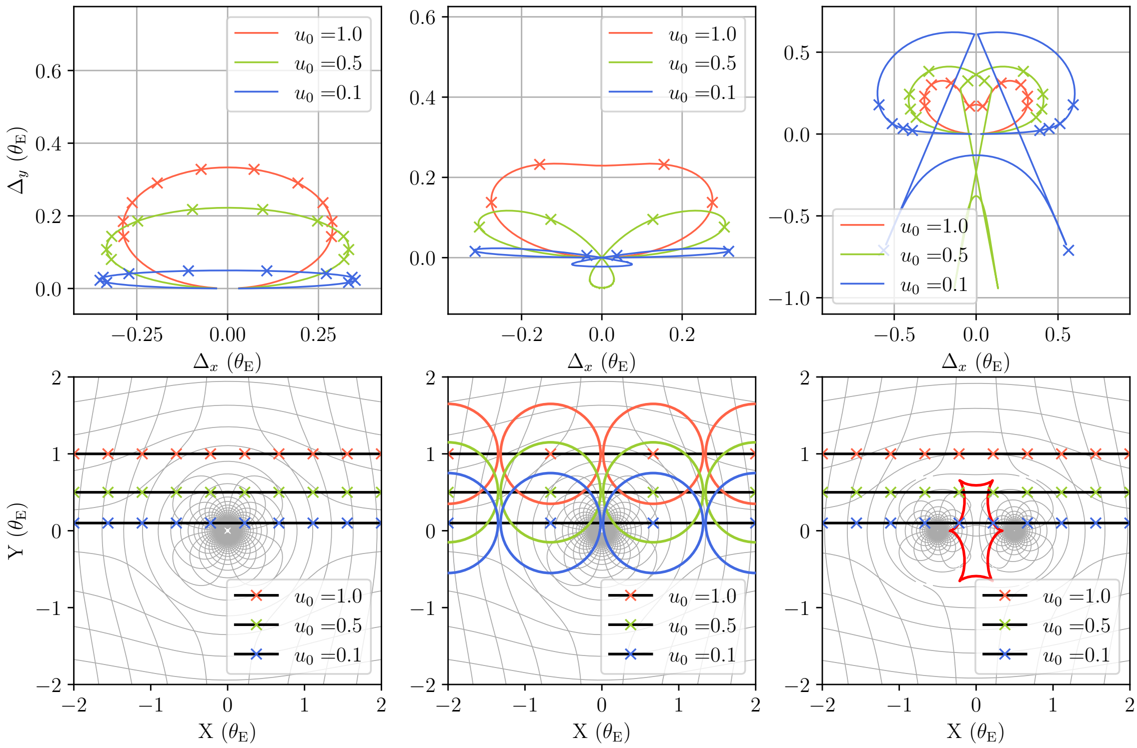

FIGURE 1.10: The source centroid offsets for a PSPL model (left), FSPL model (middle) and binary lens model (right) are shown on the top row. On the bottom row is shown the trajectory of the source for three different impact parameters: $u_0 = 0.1$, $u_0 = 0.5$ and $u_0 = 1.0$. The grid-lines on the bottom row are shown in their lensed form to illustrate the position scale of the lens potential. For the finite source model, the circular disk of the source, with a radius of $\rho = 0.65$, is indicated over several test locations across the source's trajectory. For the binary model, the parameters $s = 1.0$, $q = 1.0$ and $\alpha = 0°$ were used for simplicity, with the resonant caustic shown in red in the bottom right diagram. The effect of introducing finite source effects and lens binarity on the centroid offset tracks is significant, with "clover" structure appearing for the finite source scenario and sudden jumps as the source passes over the resonant caustic for the binary lens scenario. Both the PSPL and binary lens scenarios use 10 sample locations and the finite source 4 locations, equally space along the source's trajectory in the bottom row, with their equivalent locations indicated on the top row.

space. The passage of the source near cusps also has a noticeable although continuous effect on the offset trajectory. In figure 1.10, an example of the centroid offset under PSPL, FSPL and binary lensing conditions for various minimum impact parameters is shown.

1.9 Outline

The scientific work comprising this thesis will begin with chapter 2, where we shall describe a new simulation tool MaBμlS-2, which will then be used to compare the Besançon Galactic model with empirical data from the OGLE-IV survey. A rigorous definition of the microlensing optical depth, mean Einstein radius crossing time and event rate will be discussed and a sky map of each of those parameters produced and compared with real data. A modified version of the MaBμlS-2 simulation code will then be used once again in chapter 3 to make predictions of free-floating planet (FFP) event rates to inform a possible future mission which would involve the upcoming Euclid and Roman space telescopes, taking full advantage of finite source and parallax effects to acquire direct mass measurements of Earth and Jupiter mass FFPs. Chapter 4 will begin with a further usage of MaBμlS-2, comparing a distribution of effective event timescales to observations by the K2C9 Kepler Space Telescope microlensing campaign, before continuing with a full analysis of a binary microlensing event discovered in K2C9 which will yield a new exoplanet discovery. In the final chapter, we shall explore in depth the mathematics of binary and multi-lens caustics and use it to explore the detectability of Earth by alien civilisations via microlensing. We will finish the final chapter by examining methods of speeding up these advanced multi-lens calculations and bench-marking them with current methods. Let us now begin with the first chapter to lay the ground work for the MaBμlS-2 simulation code.

Chapter 2

MaBμlS-2

This chapter is based on the paper *MaBμlS-2: high-precision microlensing modelling for the large-scale survey era* (Specht et al., 2020).

Due to the resources invested, effort should be taken to maximise the science return for a microlensing survey. Precisely where a telescope, either ground-based or space-based, should be directed, will depend on the structure of the Galaxy; areas of the sky with maximal lens and source objects will naturally yield a higher microlensing event detection rate and as such, it is of great import that we are equipped with an accurate Galactic model of stellar properties, such as their mass distribution, initial mass functions (IMFs) and kinematics. From such a Galactic model, we can then simulate the regions of the sky, from Earth's vantage point, which yield the greatest number of microlensing events for a given survey telescope's specification and survey science goals.

Such telescopes include the upcoming Vera Rubin Observatory in Chile (Sajadian & Poleski, 2019) as well as the Nancy Grace Roman and Euclid space telescopes (Bachelet & Penny, 2019), which show promise for delivering significantly more microlensing data than has been collected thus far. The total number of microlensing events detected since the inception of the method is of the order 10^4 and with the advent of these next generation telescopes, this number could reach 10^5 for optimised surveys.

The reverse is also true; past microlensing surveys such as MOA-II (Sumi et al., 2013) and OGLE-IV (Mróz et al., 2019) have helped inform and confirm Galactic models which forward our understanding of the cosmos. MaBμlS-2 is the successor to the Manchester-Besançon Microlensing Simulator (MaBμlS), developed by Awiphan et al. (2016), which employed the Besançon Galactic model to simulate the microlensing optical depth, rate-weighted average event timescale, event rate per source star and event rate per square degree per year in a $20^\circ \times 20^\circ$ region centred on the Galactic bar and aligned on Galactic coordinates l and b. The original work identified evidence of a deficit of stars in the Galactic bar, which was found by Sumi & Penny (2016) to be caused primarily by an underestimation of stellar counts in the MOA-II analysis.

MaBμlS-2 uses the same Galactic model but makes several improvements over the original version. Of note is the event selection criterion, which now implements event signal-to-noise considerations, as well as a formal treatment of finite source effects. The generation of the microlensing parameter maps was also streamlined and parallelised, employing the resources of a multi-node computer cluster (HYDRUS) to reduce computation time from months to hours or days. Both versions of MaBμlS have used online tools to present simulation results by allowing a selection of parameter ranges in source magnitude and event timescale to include in the parameter map. MaBμlS-2 improves on the accuracy of the map generation from the simulation results and allows the user to screen events for their lens-source relative proper motion as an additional selection parameter.

2.1 The Besançon Galactic Model

The calculation of accurate microlensing parameters is impossible to achieve analytically and requires a detailed treatment of Galactic structure and interstellar extinction. The Besançon Galactic Model (BGM) generates a synthetic population of stars drawn from four Galactic components, namely a thin disk, thick disk, bar and halo. Initially developed by Robin et al. (2003) and first employed in the calculation of microlensing parameter maps by Kerins et al. (2009), the BGM has been continually updated as new data from stellar surveys are collected. The version used in MaBμlS-2 is BGM1307, also developed by Annie Robin, which is the same version employed by legacy MaBμlS thus allowing for a more faithful analysis of the improvement in simulation accuracy between the two versions of MaBμlS.

The choice of version was also justified by the close matching of the stellar proper-motion distribution in Galactic coordinates, μ_l and μ_b, to empirical data from the Hubble Space Telescope (HST) presented in Clarkson et al. (2008). This comparison was made by generating stars with BGM1307 along two lines of sight, $(l, b) = (1.1°, -2.7°)$ and $(l, b) = (1.35°, -2.7°)$ with a combined solid angle of 1.44 degrees^2. As the BGM can generate apparent magnitude data in user specified wavelength bands, the Sloan r and i filters were used to simulate the HST F814W and F606W bands. The Johnson Cousins H-band magnitude was also generated, which was used to restrict the source population to stars satisfying $H < 25$. The synthetic stars were drawn from the thin disk and Galactic bar populations and a subset of these were chosen to be disk proxy and bar proxy stars to model the population sample from the HST kinematics analysis. Figure 2.1 shows how this selection process was performed and follows similar criteria to Penny et al. (2019), who performed the analysis on BGM1106; stars with $17 \leq r \leq 20$ were considered for proxy stars, while the criterion $r - i \leq 0.8$ was used to select the 35 disk proxies from this subset and $r - i > 0.8$ for the 120 bar proxies.

As shown in figure 2.2, there is good agreement between the predictions of BGM1307 and empirical data, as shown by the 1σ contours of the proper motion distributions for both proxy groups. The proper motions of stars in the HST analysis were calculated relative to the centroid of the bar's distribution, hence the inclusion of an offset in the axes of the plot. For the bar's kinematics, the distribution widths were found to be $(\sigma_l, \sigma_b) = (3.12, 2.20)$ mas year^{-1}, compared to $(3.0, 2.8)$ mas year^{-1}from HST data. The

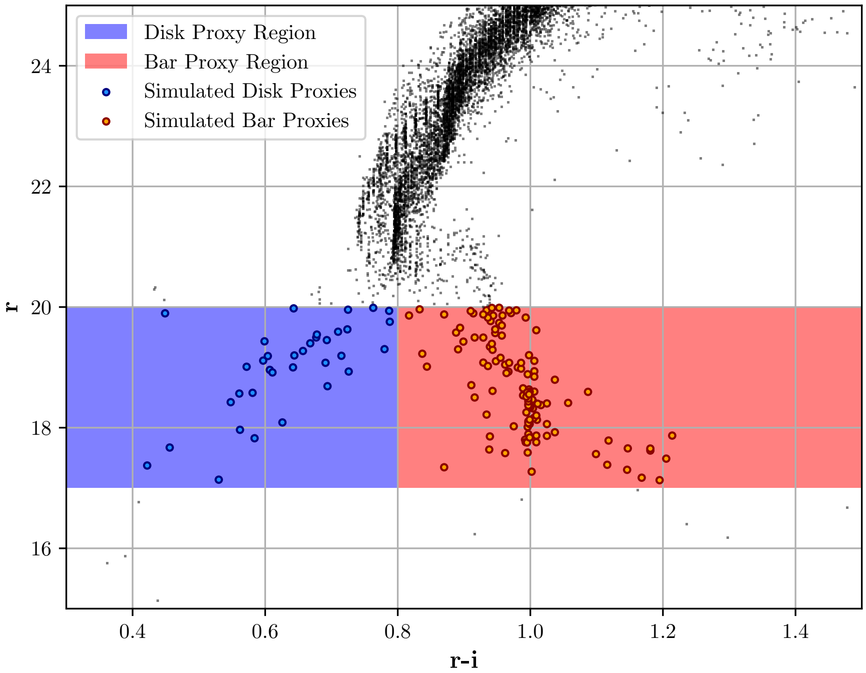

FIGURE 2.1: The colour-magnitude diagram for all source stars generated by BGM1307 for the HST comparison is shown above in the Sloan r filter and $r - i$ colour. Black dots are source stars that did not make the proxy selection cut. The bifurcation of the distribution begins at $r = 20$. The blue rectangular region shows the selection area for disk proxy stars, while the red area shows the equivalent for bar proxy stars. The blue and red outlined circles show the locations of the 35 disk proxies and 120 bar proxies, respectively, selected with these criteria.

disk proxy population's centroid was located at $(\mu_l, \mu_b) = (2.58, -0.61)$ mas year^{-1}, compared to $(3.24, -0.81)$ mas year^{-1}from HST data, with a width of $(\sigma_l, \sigma_b) = (2.23, 1.28)$ mas year^{-1}, compared to $(2.2, 1.3)$ mas year^{-1}from HST data. This is a marked improvement over version 1106, which showed a large over-prediction in the bar's distribution width in galactic longitude, as well as a noticeable negative centroid offset in Galactic latitude for the disk population's kinematics relative to HST measurements.

A comparison was also made with Gaia data (Arenou et al., 2017). Some disagreement between BGM1307 and Gaia data was found in the form of an over prediction of star counts by the model, although this is due primarily to incompleteness of Gaia catalogues for faint stars. This over prediction, however, also extended to bright stars in the bulge region, predominantly at low Galactic latitudes around $|b| < 2°$.

We shall now turn our attention to the individual components comprising the Galaxy in BGM1307. Each component is described by a stellar mass distribution ϕ, a stellar initial mass function (IMF) $\zeta(M)$ and a 3D velocity dispersion σ_{UVW}. Each is capable of producing stars that can act as either lens or source objects for the purposes of microlensing, although some components are more significant in this regard than others.

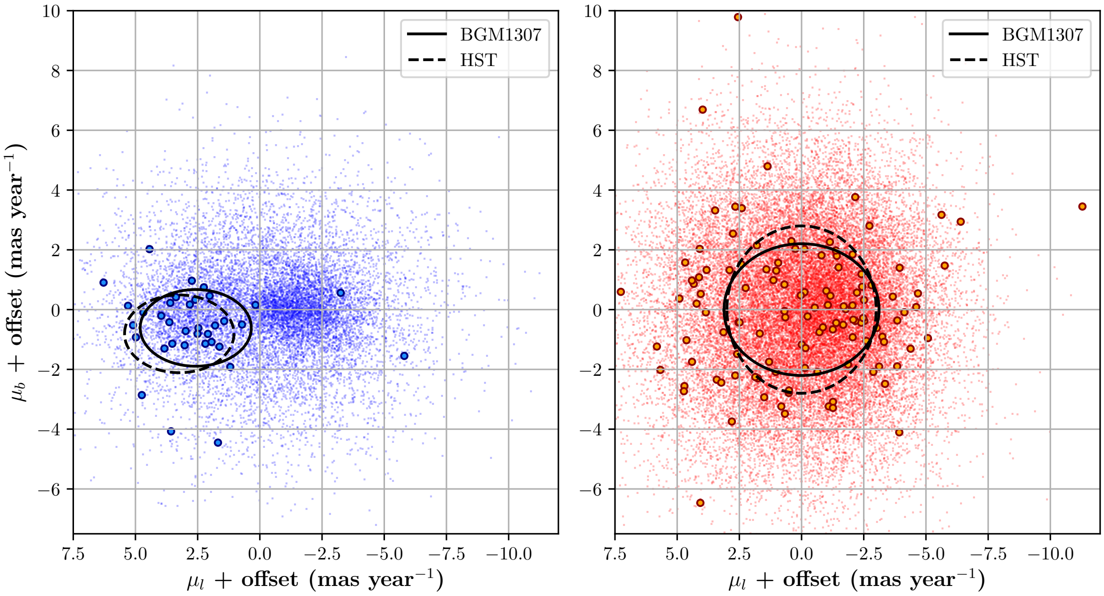

FIGURE 2.2: The proper motion distributions in Galactic coordinates are shown for both disk (left) and bar (right) populations. Small blue and red dots represent synthetic source stars drawn respectively from the generated thin disk and Galactic bar populations which did not satisfy the proxy star selection criteria. The circles represent the same proxy stars from figure 2.1. Solid black lines represent the 1σ contours of the proxy star distributions, while the dashed lines represent the 1σ contours from the HST data in Clarkson et al. (2008). The widths of the BGM and HST bar distributions are $(3.12, 2.20)$ and $(3.0, 2.8)$ mas year^{-1}. The widths of the corresponding disk distributions are $(2.23, 1.28)$ and $(2.2, 1.3)$ mas year^{-1}and centroid locations $(2.58, -0.61)$ and $(3.24, -0.81)$ mas year^{-1}, respectively.

2.1.1 The Thin Disk

One of the most important Galactic components by contribution to the microlensing rate is the thin disk (Robin et al., 2012). It has a relatively young population of stars, including the Sun, which is assumed to have a peculiar velocity relative to the local standard of rest (LSR) of $v_{\odot} = (11, 12, 7)$ km s^{-1} as determined by Schönrich et al. (2010). The LSR is assumed to have a rotational velocity of 240 km s^{-1} which is extracted from the Galactic rotation curve presented in Caldwell & Ostriker (1981). The mass density distribution of stellar material in the thin disk is characterised by two ellipsoids with axis ratios ϵ: a main body with a scale radius $R_d = 2170$ pc, truncated at 14 kpc and a central hole with scale radius $R_h = 1330$ pc in cylindrical polar coordinates. These two structures are modelled by exponentials of the form

$$\phi(r,z) = \phi_0 \left\{ exp\left(-\frac{1}{2}\sqrt{\frac{1+4a^2}{R_d^2}} \right) - exp\left(-\frac{1}{2}\sqrt{\frac{1+4a^2}{R_h^2}} \right) \right\}, \tag{2.1}$$

$$a^2 = r^2 + \left(\frac{z}{\epsilon}\right)^2. \tag{2.2}$$

The disk is further subdivided into seven age groups, each with their own velocity dispersions, luminosity functions and stellar effective temperature distributions. The velocity dispersions reflect the secular evolution of Galactic kinematics following work from Gomez et al. (1997), with an average of $\sigma_{UVW} = (30, 20, 13)$ km s^{-1} and up to a maximum of $(43, 28, 18)$ km s^{-1}. The star formation rate (SFR) and IMF is assumed to be constant across the disk, with an IMF given by

$$\zeta(M) \propto \begin{cases} M^{-1.6}, & 0.079 M_{\odot} \leq M < 1 M_{\odot} \\ M^{-3}, & M \geq 1 M_{\odot} \end{cases}. \tag{2.3}$$

2.1.2 The Thick Disk

The thick disk component is populated by older stars, generated by the model as a single burst around 10 Gya. While it extends to higher Galactic latitudes than the thin disk, it is also less dense overall and plays a lesser role in microlensing at lower latitudes, but becomes a significant contributor around $|b| > 9°$. The shape of the stellar mass distribution is given by the product of a radial exponential with scale radius $h_R = 2355.4$ pc and a broken quadratic/exponential function with scale height $h_z = 533.4$ pc and break distance $\xi = 658$ pc in the vertical direction (Robin et al., 2014). It is normalised to the density of the solar neighbourhood ϕ_0 and centred at the solar coordinates $(r_{\odot}, z_{\odot})$ through

$$\phi(r,z) = \phi_0 exp\left(\frac{r_{\odot} - r}{h_R} \right) \begin{cases} 1 - \left(\frac{z^2}{\xi(2h_Z + \xi)} \right), & z \leq \xi \\ \frac{2h_z}{2h_z + \xi} exp\left(\frac{\xi - |z - z_{\odot}|}{h_z} \right), & z > \xi \end{cases}. \tag{2.4}$$

The luminosity function of the thick disk was extracted from Bergbusch & Vandenberg (1992) using an isochrone of 10 Gyr. Its IMF was modelled by a power law beginning at $0.154M_\odot$ via

$$\zeta(M) \propto M^{-1.5}. \tag{2.5}$$

Like the thin disk, the thick disk is described by a rotational velocity, in this case taken to be 176 km s^{-1}, with a velocity dispersion of $\sigma_{UVW} = (67, 51, 42)$ km s^{-1}.

2.1.3 The Bar

The Galactic bar is arguably the most important component with respect to microlensing, due to its high mass density. It can provide both plentiful source and lens objects from which microlensing events can be generated and is predominant at Galactic latitudes $|b| < 5^\circ$. Its age is taken to be 8 Gyr and as such, is dominated by older, red stars by comparison to the thin disk. Its density distribution takes the form of a triaxial ellipsoid, with axis lengths $x_0 = 1.46$ kpc, $y_0 = 0.49$ kpc and $z_0 = 0.3$ kpc, with its x coordinate axis rotated by 12.89° relative to the Sun-Galactic centre axis, as determined by Robin et al. (2012). To further control its shape, the parameters $C_\parallel = 0.5$ and $C_\perp = 3.007$ are used to influence the 'disky' or 'boxy' nature of the ellipsoid, respectively. The distribution is given in galactocentric Cartesian coordinates by the product of a hyperbolic function and a Gaussian cutoff in the x-y plane, with a cutoff radius of $R_C = 3.43$ kpc via

$$\phi(x, y, z) = \phi_0 sech^2\big(-R_s(x, y, z)\big) f_c\Big(\sqrt{x^2 + y^2}\Big), \tag{2.6}$$

$$R_s(x, y, z)^{C_\parallel} = \left(\left[\frac{x}{x_0}\right]^{C_\perp} + \left[\frac{y}{y_0}\right]^{C_\perp}\right)^{\frac{C_\parallel}{C_\perp}} + \left(\frac{z}{z_0}\right)^{C_\parallel}, \tag{2.7}$$

$$f_c(R_{xy}) = \begin{cases} 1, & R_{xy} \leq R_C \\ exp\left(-\left(\frac{R_{xy}-R_C}{0.5\ \mathrm{kpc}}\right)^2\right), & R_{xy} > R_C \end{cases}. \tag{2.8}$$

The IMF of the bar is given by a broken power law and begins at $0.15M_\odot$ as

$$\zeta(M) \propto \begin{cases} M^{-1.5}, & 0.15M_\odot \leq M < 0.7M_\odot \\ M^{-2.35}, & M \geq 0.7M_\odot \end{cases}. \tag{2.9}$$

Its kinematics were derived from an N-body simulation (Gardner et al., 2014), with a velocity dispersion of $\sigma_{UVW} = (150, 115, 100)$ km s^{-1}, the largest of all the components.

2.1.4 The Halo

Due to its low average density, the halo component does not contribute a significant quantity of potential lens stars around the Galactic bulge and only becomes significant at high latitudes. Furthermore, as stars in the halo are generated with an age of 14 Gyr, most have magnitudes greater than 18 and hence do not typically qualify for microlensing sources. This extreme age also leads to low metallicities of $[Fe/H] = -1.78$, as described in Robin et al. (2014). The density distribution for the halo takes the form of an ellipsoid with axis ratio $\epsilon = 0.768$, with a power law profile given by

$$\phi(r,z) = \phi_0 \left(r^2 + \left(\frac{z}{\epsilon} \right)^2 \right)^{-1.695}. \tag{2.10}$$

Its IMF begins at stellar masses above $0.085 M_\odot$ and is described by a single power law,

$$\zeta(M) \propto M^{-1.5}, \qquad M > 0.085 M_\odot. \tag{2.11}$$

The kinematics of the halo, much like the bulge and unlike the thin and thick disks, does not feature a rotational velocity. As such, the halo has the second highest velocity dispersion of $\sigma_{UVW} = (131, 106, 85)$ km s^{-1}.

2.1.5 Adding Low Mass Objects

Due to the lower mass limits of Galactic bar, thick disk and halo components, synthetic catalogues generated by BGM1307 do not include the lowest mass M dwarfs, nor do any components include brown dwarfs which are not modelled by BGM1307. In spite of this, both types of objects can still act as lenses and indeed the lowest mass red dwarfs vastly outnumber the most massive and brightest stars due to the slopes of the IMFs. As such, it was important to include these objects in the MaBμlS-2 simulation. For the bar, thick disk and halo components, their IMFs were extended down to the hydrogen burning limit of $0.079 M_\odot$ and the resulting integrals over the extended regions were compared with the corresponding integrals over the original IMFs to determine the amount of new stars required to generate. As these stars are not expected to be sources for microlensing purposes, they were assigned magnitudes of 99. Their kinematics and locations were inherited, at random, from another star in their respective components.

As for brown dwarfs, no firmly established mass function exists. To implement these objects, a mass function power law slope was fitted to OGLE-IV timescale data (Mróz et al., 2019) using a χ^2 minimisation of 258 sample locations in the OGLE-IV field. Calculations were made in power law slope intervals of 0.1 between -0.9 and 1.0. This approach was taken in the previous version of MaBμlS by Awiphan et al. (2016) using MOA-II data, which retrieved an IMF slope of -0.4, while the MaBμlS-2 minimisation retrieved a value of 0.1, as shown in figure 2.3. The discrepancy was attributed to the mismatch between the low timescale regime of the $\langle t_{\mathrm{E}} \rangle$distribution derived from MOA-II data in Sumi et al. (2013) and OGLE-IV data in Mróz et al. (2019), illustrated in figure 2.4. This difference manifested as a significant excess in OGLE timescale relative to MOA, averaging to 3.6 days, over the intersection of the MOA-II and OGLE-IV fields, but with a notable deficit

Data	τ_0	a
MaBμlS-2 all sources	1.78 ± 0.04	0.35 ± 0.01
OGLE-IV all sources	1.48 ± 0.05	0.35 ± 0.02
MOA-II RCG sources	1.38 ± 0.21	0.40 ± 0.17
MOA-II all sources	1.98 ± 0.14	0.44 ± 0.07

TABLE 2.1: The exponential profile fits for optical depth maps in the $|l| < 5°, b < 0°$ region using the normalisation τ_0 and scale size a from equation 2.12.

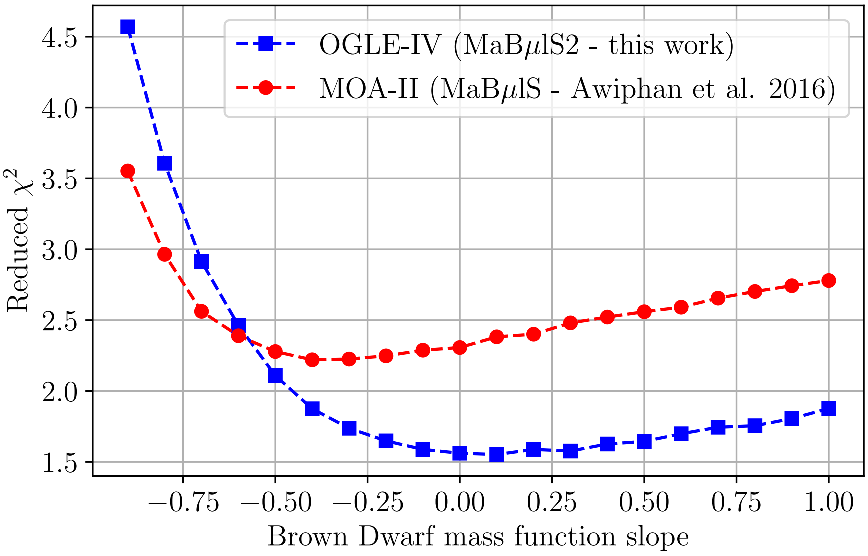

FIGURE 2.3: The reduced χ^2 minimisation for brown dwarf mass function slope for legacy MaBμlSwith MOA-II data and the new MaBμlS-2 with OGLE-IV data is shown. MaBμlS-2 shows superior performance across the parameter space beyond -0.6 and achieves a lower reduced χ^2 at minimum of 1.5 compared to the legacy's -0.4.

in the $2° < l < 4°$ region. To investigate this discrepancy further, an exponential optical depth profile with normalisation τ_0 and scale size a of the form

$$\tau(b) = \tau_0 e^{a(3-|b|)} \tag{2.12}$$

was fitted to the $b < 0°, |l| < 5°$ region of the optical depth maps of the MaBμlS-2 simulation, OGLE-IV data, MOA-II RCG sources and MOA-II all sources. The results show a stronger agreement in scale size between MaBμlS-2 and the MOA-II RCG profile compared to the MOA-II all sources exponential, suggesting that blending could play a role in the reported timescale discrepancy. This analysis also showed a marked improvement in the minimum reduced χ^2 value between the new MaBμlS-2 of 1.5 and the legacy version of 2.2, reflecting improvements in the simulation accuracy.

2.1.6 Synthetic Catalogue Generation

Each of the four Galactic components in the model contribute to the generation of stars in the output of the BGM code, which comes in the form of synthetic catalogues of stars.

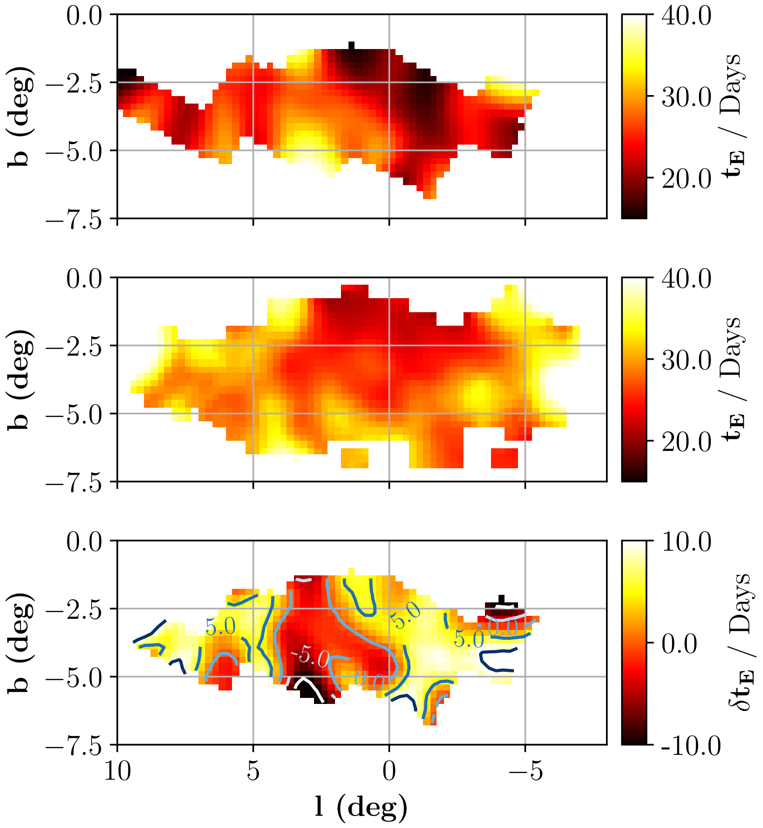
0.0
−2.5
−5.0
−7.5
b (deg)
40.0
30.0
20.0
tE / Days
0.0
−2.5
−5.0
−7.5
b (deg)
40.0
30.0
20.0
tE / Days
0.0
−2.5
−5.0
−7.5
b (deg)
5.0
-5.0
0.0
5.0
5.0
10.0
0.0
-10.0
δtE / Days
10
5
0
−5
l (deg)

FIGURE 2.4: On the top is shown the MOA-II timescale map, with the $b < 0°$ portion of the OGLE-IV timescale map shown in the middle and the difference between the two (OGLE-IV - MOA-II) is shown on the bottom. Contours at 5-day intervals are shown on the difference map, where it is evident that OGLE-IV exceeds the MOA-II timescale in most regions except for $2° < l < 4°$.

Magnitude Bracket	Magnitude Range
1	$0 \leq K < 15$
2	$15 \leq K < 20$
3	$20 \leq K < 24$
4	$24 \leq K < 99$

TABLE 2.2: The magnitude brackets used for each of the four catalogues generated for each line of sight in the MaBμlS-2 simulation. Only stars in brackets 1 → 3 were considered as lens and source stars, while objects in bracket 4, which encompasses the post-BGM generated low mass red and brown dwarfs, were considered only as lenses.

BGM1307 uses a 3-dimensional interstellar extinction map, calibrated using 2MASS survey data (Marshall et al., 2006) and has a resolution of 0.25°. Hence, over the $20^\circ \times 20^\circ$ field simulated by MaBμlS-2, a total of $80 \times 80 = 6400$ catalogues were generated, one for each line of sight covering 0.0625°^2}. Due to the immense scale of the Galaxy and the billions of stars it contains, it is necessary to strictly control the quantity of stellar data the model generates. As an input to the BGM synthesis code, one can pass a list of locations in the sky and a corresponding square solid angle Ω_{cat} over which to generate stars in order to reduce star counts in crowded regions, or boost them in sparse regions. Naturally, the maximum size of Ω_{cat} was limited to 0.0625°^2} to prevent sampling regions of space already simulated in adjacent lines of sight.

Furthermore, simply restraining all stars along a line of sight to a single solid angle privileges the lowest mass stars which dominate in star count due to their IMF values. To compensate for this and hence sufficiently sample brighter stars which dominate the microlensing source population, each line of sight was subdivided into four magnitude brackets, defined by the stars K-band magnitude, shown in table 2.2. The solid angles for each were adjusted to produce roughly 10,000 stars per bracket. This ultimately yielded 40,000 stars per line of sight and a quarter of a billion stars in total.

2.2 Microlensing Parameters

Now that the nature of the input to the MaBμlS-2 simulation has been established, let us now consider the output. There are four different microlensing parameter maps that MaBμlS-2 can generate, each of which will be discussed in the following sections. These maps can be used to make predictions about the microlensing event rate to inform upcoming microlensing surveys, or they can be compared to empirical data in order to verify the accuracy of the Besançon model. In this work, we assume a maximum normalised impact parameter $u_t = 1$ as a threshold for selecting microlensing events, which is typical for ground-based surveys, although in principle, this can be easily extended to $u_t = 3$ or higher for space-based surveys with superior signal-to-noise constraints.

2.2.1 The Microlensing Optical Depth

The microlensing optical depth τ is analogous to the optical depth in other areas of astronomy. It quantifies, for a particular source star, what fraction of the local sky will generate a microlensing event, from our vantage point. Analogously, the optical depth can also be viewed as the probability that a source star is undergoing a microlensing event at any particular time. Typical values for optical depth when dealing with stellar mass lenses are on the order $10^{-7} \rightarrow 10^{-5}$, as evident in figure 2.5. Assuming a continuous mass distribution $\phi(D_l)$ between the observer and the source, the microlensing optical depth is given by

$$\tau = \frac{4\pi G}{D_{\mathrm{s}}c^2} \int_0^{D_{\mathrm{s}}} \phi(D_{\mathrm{l}}) D_{\mathrm{l}} (D_{\mathrm{s}} - D_{\mathrm{l}}) dD_{\mathrm{l}}. \tag{2.13}$$

From equation 2.13, we can see that the optical depth is a probe of the mass distribution of lens objects along the line of sight to the particular source. In reality, we do not deal with a continuous mass distribution due to the complexity of Galactic structure and must instead iterate over the synthetic stars generated by BGM1307. We must also average over all N_s possible source stars for the survey we are interested in modelling. We must also define a sensitivity region, which is a circular region in the sky for a particular valid lens-source pair, inside of which the source would be magnified sufficiently to produce a microlensing event in the survey. The radius of this region is $u_{\mathrm{max}}\theta_{\mathrm{E}}$, where u_{max} is a normalised impact parameter which depends on the source magnitude and the normalised source radius ρ and represents the furthest multiple of θ_{E} the source can pass to the lens while still generating a detectable microlensing event. The value of u_{max} is also capped to be at most the survey's maximum threshold u_t. Ensuring that only lenses satisfying $D_l < D_s$, the discreet calculation for optical depth is given by

$$\tau = \pi \frac{\sum_s^{N_s} \frac{1}{\Omega_s} \sum_l^{N_l} u_{\mathrm{max}}^2 \theta_{\mathrm{E}}^2 \frac{1}{\Omega_l}}{\sum_s^{N_s} \langle w^2 \rangle \frac{1}{\Omega_s}}, \tag{2.14}$$

where the solid angles Ω_s and Ω_l are the solid angles of the catalogues from which the source and lens object are drawn from, respectively, and $\langle w^2 \rangle$ is the weight for a particular source object, which lies between $[0, 1]$ and quantifies the contribution of each source to the optical depth. This value will be 1 for fully resolved sources but will dip below 1 for sources which are only visible during magnification. Such sources are detected primarily via the method of difference image analysis (DIA, Alard (2000)) and are known as *DIA sources*. The pth moment of the weight parameter for a particular source is

$$\langle w^p \rangle = \frac{\sum_l^{N_l} w^p \mu_{\mathrm{rel}} D_{\mathrm{l}}^2 \theta_{\mathrm{E}} \frac{1}{\Omega_l}}{\sum_l^{N_l} \mu_{\mathrm{rel}} D_{\mathrm{l}}^2 \theta_{\mathrm{E}} \frac{1}{\Omega_l}}, \tag{2.15}$$

where the value $w^p = min(u_{\mathrm{max}}, 1)$ is the weight of a single lens-source pair. For optical depth, the second moment is used to account for the quadratic factor of u_{max}in the numerator of equation 2.14.

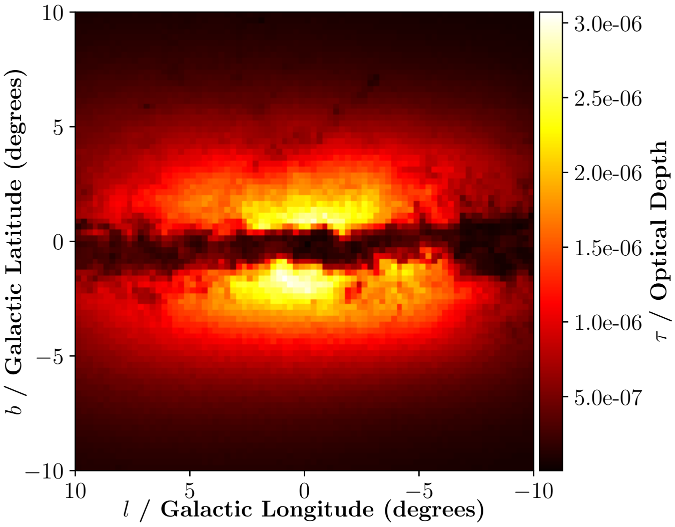

FIGURE 2.5: The microlensing optical depth in the Johnson Cousins I-band filter is shown over the entire MaBμlS-2 simulated field. The signal-to-noise threshold at peak magnification is required to be at least 50, with a telescope limiting magnitude of $m_{\mathrm{lim}} = 21$. The brightest regions coincide with the influence of the Galactic bar, while the dark region around $|b| < 1^{\circ}$ is the result of interstellar extinction from Galactic dust.

2.2.2 The Average Einstein Radius Crossing Time

Another important microlensing parameter is the rate weighted average Einstein radius crossing time, $\langle t_{\mathrm{E}} \rangle$, also known as the event timescale. While the optical depth acts as a probe of the Galactic mass distribution, the average timescale can act as a proxy for the typical lens mass along a particular line of sight, as well as a more direct probe of μ_{rel}. It follows similar logic to the calculation of optical depth with some key differences,

$$\langle t_{\mathrm{E}} \rangle = \frac{\sum_s^{N_s} \frac{1}{\Omega_s} \sum_l^{N_l} w D_{\mathrm{l}}^2 \theta_{\mathrm{E}}^2 \frac{1}{\Omega_l}}{\sum_s^{N_s} \langle w \rangle \frac{1}{\Omega_s} \sum_l^{N_l} \mu_{\mathrm{rel}} D_{\mathrm{l}}^2 \theta_{\mathrm{E}} \frac{1}{\Omega_l}}. \tag{2.16}$$

Note that u_{max} does not enter into the numerator of equation 2.16, as we are not interested in the time taken for a source to cross the radius of the microlensing sensitivity region, but a single Einstein radius instead.

A parameter which varies inversely with $\langle t_{\mathrm{E}} \rangle$ is the rate weighted relative proper motion, $\langle \mu_{rel} \rangle$. This parameter only depends on the lens mass by its weighting from θ_{E}, via

$$\langle \mu_{\mathrm{rel}} \rangle = \frac{\sum_s^{N_s} \frac{1}{\Omega_s} \sum_l^{N_l} w \mu_{\mathrm{rel}}^2 D_{\mathrm{l}}^2 \theta_{\mathrm{E}} \frac{1}{\Omega_l}}{\sum_s^{N_s} \langle w \rangle \frac{1}{\Omega_s} \sum_l^{N_l} \mu_{\mathrm{rel}} D_{\mathrm{l}}^2 \theta_{\mathrm{E}} \frac{1}{\Omega_l}}, \tag{2.17}$$

and acts as a useful measure of Galactic kinematics. In cases where the user of the MaBμlS-2 simulation may be interested in events where the lens and source objects separate measurably over time, a high value of $\langle \mu_{rel} \rangle$ can be enforced to yield an event rate for such scenarios. Typical values for $\langle t_{\mathrm{E}} \rangle$ can range from hours for planetary mass lenses up

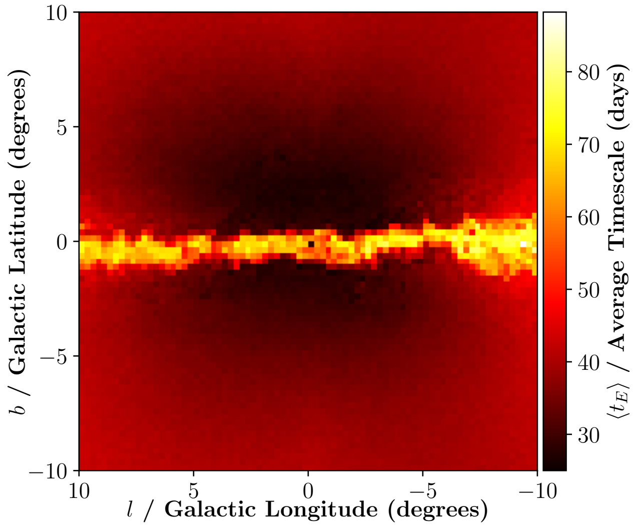

FIGURE 2.6: The average microlensing timescale is shown across the MaBμlS-2 field, using the same configuration and selection criteria as figure 2.5. Much like the optical depth, the Galactic bar and Galactic dust play key roles in shaping its structure, but in the case of the timescale, the roles are reversed, with the high μ_{rel} from sources and lenses in the bar reducing the timescale and the dust bar restricting source objects to the disk with low μ_{rel} and increasing the timescale.

to years for the most massive lenses with small μ_{rel}, with stellar mass lenses producing events lasting several weeks, as shown in figure 2.6.

2.2.3 The Microlensing Event Rate

The final two parameters considered in the MaBμlS-2 simulation are the event rate per source star per year, Γ_* and event rate per square degree per year, $\Gamma_\circ$, with typical values shown in figure 2.7. The value of Γ_* is important for informing surveys interested in monitoring particular kinds of stars, while $\Gamma_\circ$ provides a more holistic view on event rates over areas of the sky. The calculation of event rate does not involve any new summations over lenses and sources and is instead a function of τ and $\langle t_{\text{E}} \rangle$ through

$$\Gamma_* = \frac{2}{\pi} \frac{\tau}{\langle u_{\max} t_{\text{E}} \rangle}, \tag{2.18}$$

$$\Gamma_\circ = \frac{2}{\pi} \frac{\tau N_*}{\langle u_{\max} t_{\text{E}} \rangle}, \tag{2.19}$$

where the parameter $\langle u_{\max} t_{\text{E}} \rangle$ is the average of the timescale multiplied by $u_{\max}$ and the value N_* represents the rate weighted number of sources, indexed with s, considered in the calculation of τ and $\langle t_{\text{E}} \rangle$,

$$N_* = \sum_{s=1}^{N_s} \langle w \rangle. \tag{2.20}$$

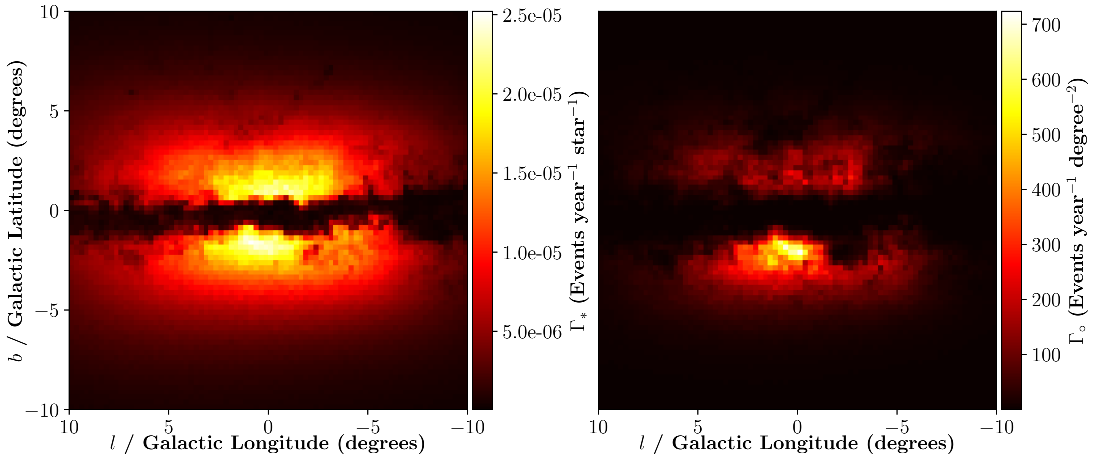

FIGURE 2.7: On the left is shown the microlensing event rate per source star per year, again using the same configuration and selection criteria as figure 2.5, with values on the order of 10^{-5}. Its structure is much the same as the optical depth, with a higher contrast due to the presence of $\langle t_\mathrm{E} \rangle$ in its denominator. On the right is shown the event rate per square degree per year which depends on the total source star count and is much more sensitive to Galactic dust, peaking in the hundreds of events per year near Baade's window before falling off dramatically outside.

Note that the value of $\langle u_\mathrm{max} t_\mathrm{E} \rangle$ is equivalent to $\langle t_\mathrm{E} \rangle$ in the case where $u_t = 1$ as is the case for the MaBμlS-2 simulation.

2.3 Improvements on Legacy MaBμlS

2.3.1 Error Estimation

Major improvements in the estimation of the error on each of the microlensing parameters were made in the MaBμlS-2 simulation code. In the legacy version, all valid source stars were distributed into two bins and the differences between their optical depth and timescale values were taken to be approximations for the standard deviation on those values and a reasonable estimate of the values' errors. While computationally straightforward, this method of error estimation ignores the variance caused by lens parameters. To account for this, a new method was developed which, for each source s, distributed lenses into ten bins and calculated the standard deviation σ_{X_s} on parameter X, which was either τ or $\langle t_\mathrm{E} \rangle$. Once evaluated, the source contributions, $X_s \pm \sigma_{X_s}$ with weights $\langle w \rangle_s$, were distributed into a further ten bins, denoted by i, to produce $X_i \pm \sigma_{X_i}$ with weights $\langle w \rangle_i$. The final error on parameter X is given by

$$\sigma_X = \sqrt{\frac{\sum_i (X_i^2 + \sigma_{X_i}^2)\langle w \rangle_i}{\sum_i \langle w \rangle_i} - \left(\frac{\sum_i X_i \langle w \rangle_i}{\sum_i \langle w \rangle_i}\right)^2}. \tag{2.21}$$

The rates Γ_* and $\Gamma_\circ$ which depend on τ and $\langle t_\mathrm{E} \rangle$from equations 2.18 and 2.19, have errors given by

$$\sigma_\Gamma = \Gamma\sqrt{\left(\frac{\sigma_\tau}{\tau}\right)^2 + \left(\frac{\sigma_{\langle t_\mathrm{E}\rangle}}{\langle t_\mathrm{E}\rangle}\right)^2}. \tag{2.22}$$

Typical estimates of the error on τ and $\langle t_\mathrm{E}\rangle$ are on the order of 5% near the bulge, but increase in the dust bar beyond 10%, contingent on the parameter ranges chosen for evaluation, which will increase the error estimate as fewer lens-source pairs are accepted. Figure 2.8 shows, for each parameter map in the Johnson-Cousins *I*-band filter, its corresponding error map as a percentage.

2.3.2 Finite Source Effects

For microlensing events in the large angular source size or low mass lens regime, the value of ρ becomes significant enough that the PSPL model is insufficient to calculate the value of u_max, as high magnifications are no longer achievable, even for $u = 0$. Conversely, in some finite source cases, higher magnifications can be achieved at larger impact parameters due to the closer proximity of some parts of the source to the lens. These discrepancies with the PSPL model were not formally represented in the legacy MaBμlS, where events with $\rho > 1$ were discarded and all other cases treated as point sources. In order to represent this regime in MaBμlS-2, a more formal treatment of finite source effects was introduced.

In the PSPL case, equation 1.16 can be reversed to obtain an expression for $u_\mathrm{max}$as a function of A_min,

$$u_{max} = \sqrt{2\left(\frac{A_{min}}{\sqrt{A_{min}^2 - 1}} - 1\right)}. \tag{2.23}$$

In order to introduce u_max as a function of ρ, a numerical finite source calculation must be performed. A fast method developed by Lee et al. (2009) integrates the PSPL magnification over a circular source with a linear limb darkening profile for a specified impact parameter u. Although efficient for a finite source calculation, the amount of lens-source pairs with significant source radii in the MaBμlS-2 simulation is on the order of 10^6 or greater, dependent on the filter wavelength, making a real-time computation impractical. To deal with this, a 100×100 grid of u_max values was generated before running the MaBμlS-2 simulation, which then performed a simple linear interpolation over this grid when necessary.

Simply generating u_max as a function of A_min and ρ leaves a grid that is mostly empty. This is because finite source effects fundamentally limit the magnification achievable by a source. In the point source regime, the magnification tends to infinity as the impact parameter tends to zero; in the finite source regime however, the circular disk of the source is transformed into an Einstein ring at $u = 0$ with a cutoff magnification A_cut given by the finite source magnification for $u = 0$ from equation 1.24, assuming a uniform surface brightness. Magnifications greater than this are not possible and would rule out lens-source pairs that must surpass this to satisfy event selection criterion. In order to utilise

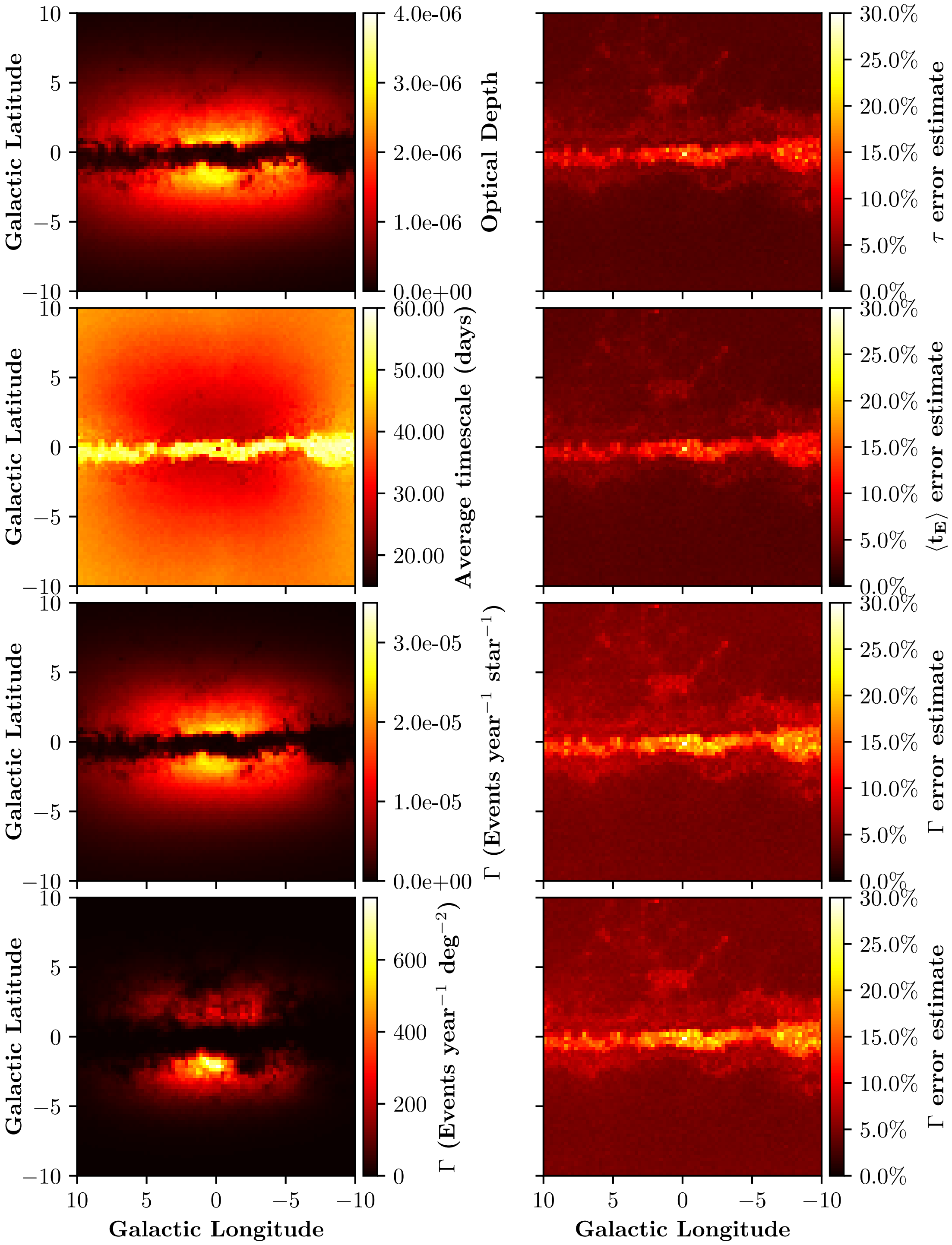

FIGURE 2.8: From top to bottom are shown the optical depth τ, average event timescale $\langle t_E \rangle$, event rate per source star Γ_* and event rate per square degree $\Gamma_\circ$ on the left and their associated error maps on the right, all using a signal-to-noise at peak magnification requirement of $S/N \geq 50$ and a survey limiting magnitude of $m_{\text{lim}} = 21$. The filter chosen for parameter evaluation is the Johnson-Cousins I-band filter.

the grid space most efficiently, a proxy parameter for magnification α, was devised which not only scales the cutoff magnitude to the top of the grid, but also uses a logarithmic transformation to reduce the gradient of the distribution to be more even across the grid. It takes the form

$$\alpha = \frac{\ln(A_{\text{min}} - A_{\text{base}} + 1)}{\ln(A_{\text{cut}} - A_{\text{base}} + 1)}, \tag{2.24}$$

where A_{base} is the magnification at the bottom of the grid, which was chosen to be $A(u = 3) = 1.017$ to allow for higher values of u_t in the case of space-based surveys. The result of applying the α transformation is shown in figure 2.9, from which it is evident that while finite source effects limit the maximum magnification achievable, they can also boost the value of u_{max} leading up to A_{cut}, which is the result of certain parts of the source being sufficiently close to the lens as to dominate over the more distant parts of the lens.

For $\rho \geq 1$, the surface brightness profile of the source star can be important. A liner limb darkening model was used, with $S(u')$ as described in equation 1.28 in section 1.5. The value of β from equation 1.28 depends both on the filter wavelength and stellar surface temperature T_{eff}. To this end, limb darkening data from Claret & Bloemen (2011) was fitted for each of the Johnson-Cousins *UBVRIJHK* filters as a function of T_{eff} using an Akima interpolant (Akima, 1970). The interpolant was then sampled in real time for each source and used to modify the u_{max} result for each lens-source pair. Unfortunately, as there is no analytical equivalent of equation 1.24 with a linear limb darkening surface brightness profile, an approximation of the effect was used by calculating an effective source radius ρ_{eff} via

$$\rho_{\text{eff}} = \beta\rho + (1 - \beta)\rho_{\text{max}}, \tag{2.25}$$

$$\rho_{\text{max}} = 1.30234 \times \left(e^{\frac{\rho}{2}} - 1\right). \tag{2.26}$$

The value of ρ_{eff} was then used to sample the u_{max} grid.

2.3.3 Event Selection Criterion

For the original MaBμlS, possible lens-source pairs were selected as valid microlensing events if the source magnitude m_s was brighter than the survey's limiting magnitude m_{lim}, defined as the magnitude which for a combination of exposure time t_{exp} and zero-point magnitude m_{zp} yielded a photometric precision of 4%. In MaBμlS-2, a more advanced method employed by Ban et al. (2016) was implemented which uses a fixed signal-to-noise (at peak magnification) event selection criterion accounting for flux contributions from unresolved stars under the point spread function (PSF) of the source star as well as a wavelength dependent uniform sky background, which more faithfully models the event selection criteria of real microlensing surveys. The PSF full width at half maximum was assumed to be seeing-limited at a value of $\theta_{\text{FWHM}} = 1$ arcsec, giving a PSF solid angle of $\Omega_{\text{PSF}} = 0.785$ arcsec^2. A Poisson model of photon noise was used to

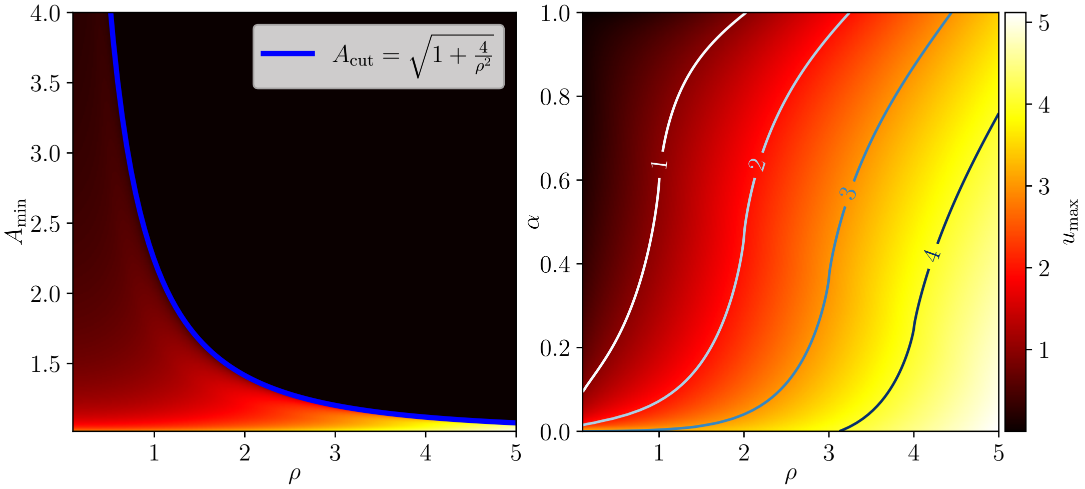

FIGURE 2.9: The distribution of $u_{\rm max}$ as a function of $A_{\rm min}$ and ρ is shown on the left, with the analytical form of $A_{\rm cut}(\rho)$ shown in blue. Above this line, $u_{\rm max}$ is zero, illustrating the need for more efficient usage of space. To the right is the same distribution, scaled using the α transformation from equation 2.24. Any points with $\alpha > 1$ yield $u_{\rm max} = 0$. The integer contours of the $u_{\rm max}$ distribution are also shown to illustrate the small gradient produced by the logarithmic transformation.

describe these contributions. The total source photons $N_{\rm src}$ collected by the telescope at peak magnification is given by

$$N_{\rm src} = t_{\rm exp} A(t_0) 10^{-0.4(m_{\rm s} - m_{\rm zp})}, \tag{2.27}$$

where $A(t_0)$ is the minimum magnification threshold $A_{\rm min}$ from section 2.3.2. $N_{\rm src}$ is the most computationally expensive of the components, as it must be computed for each source. The contribution from the uniform sky background $N_{\rm sky}$ is parameterised by the sky brightness $\mu_{\rm sky}$ in magnitudes per arcsec^2, which depends on the wavelength used, as shown in table 2.3. It is the least computationally expensive component, computed only once per wavelength band. As we are only concerned about the background light collected under the source's PSF, we arrive at

$$N_{\rm sky} = t_{\rm exp} \Omega_{\rm psf} 10^{-0.4(\mu_{\rm sky} - m_{\rm zp})}. \tag{2.28}$$

The final component $N_{\rm BG}$ comes from the background contribution of all other unresolved stars under the source's PSF, which may be unable to produce microlensing events outside of the DIA regime, but which still contribute to the photon noise for the source star in question. This is acquired by using all sources other than the source s' of the microlensing event for a line of sight to calculate an average background light, given by

$$N_{\rm BG} = t_{\rm exp} \Omega_{\rm psf} \sum_{s=1, s \neq s'}^{N_s} 10^{-0.4(m_{\rm s} - m_{\rm zp})} \frac{1}{\Omega_s}, \tag{2.29}$$

where Ω_s is the source catalogue size, which accounts for the four magnitude brackets from table 2.2. Like $N_{\rm src}$, $N_{\rm BG}$ is a function of each source per line of sight. These three

Johnson-Cousins Filter	μ_{sky} (mag arcsec^{-2})
U	22.28
B	22.64
V	21.61
R	20.87
I	19.71
J	16.50
H	14.40
K	13.00

TABLE 2.3: Tabulated above are the sky backgrounds for each filter used in equation 2.28.

components contribute to the signal-to-noise S/N,

$$S/N = \frac{N_{\mathrm{src}}}{\sqrt{N_{\mathrm{src}} + N_{\mathrm{sky}} + N_{\mathrm{BG}}}}. \tag{2.30}$$

Using equations 2.27 and 2.30, an expression for A_{min} as a function of the chosen signal-to-noise threshold is obtained,

$$A_{\mathrm{min}} = \frac{(S/N)^2 10^{0.4(m_{\mathrm{s}} - m_{\mathrm{zp}})}}{2t_{\mathrm{exp}}} \left(1 + \sqrt{1 + \frac{4(N_{\mathrm{BG}} + N_{\mathrm{sky}})}{(S/N)^2}}\right). \tag{2.31}$$

The MaBμlS-2 simulation supports signal-to-noise thresholds of 25, 50 and 100 to account for varying levels of strictness between surveys.

2.4 Online Tool Functionality

The results of the MaBμlS-2 simulation are available as an online tool[1]. The user may generate maps of optical depth, average timescale and event rate in any of the Johnson-Cousins *UBVRIJHK* filters, over any region interior to $|l|, |b| < 10^\circ$ and select for events between source magnitude limits, event timescale bounds and lens-source relative proper motion bounds. The MaBμlS-2 simulation generates, as output, data files containing the numerator and denominator of equations 2.14 and 2.16 as well as the associated error and weighted source counts for each of the 6,400 lines of sight. The output files are distinguished by their upper limits on m_{s}, t_{E} and μ_{rel}, allowing for integrals over these parameter ranges to be calculated by calculating the difference between the output of a data file with a larger upper limit from a file with a lower upper limit.

These upper limits represent the 3-dimensional bin edges of the parameter space, of which there are ten bins in m_{s}, ten in t_{E} and five in μ_{rel}, giving a total of 500 data files for both $\langle t_{\mathrm{E}} \rangle$ and τ per Johnson-Cousins filter and signal-to-noise threshold. The bin edges in m_{s} are uniformly distributed between 12 and 23 magnitudes. For the timescale bin edges, it was important to account for the linear weight dependence of a single lens-source pair to τ on that pair's timescale. As such, the 10th percentiles of the product of

---

[1] `http://www.mabuls.net/`

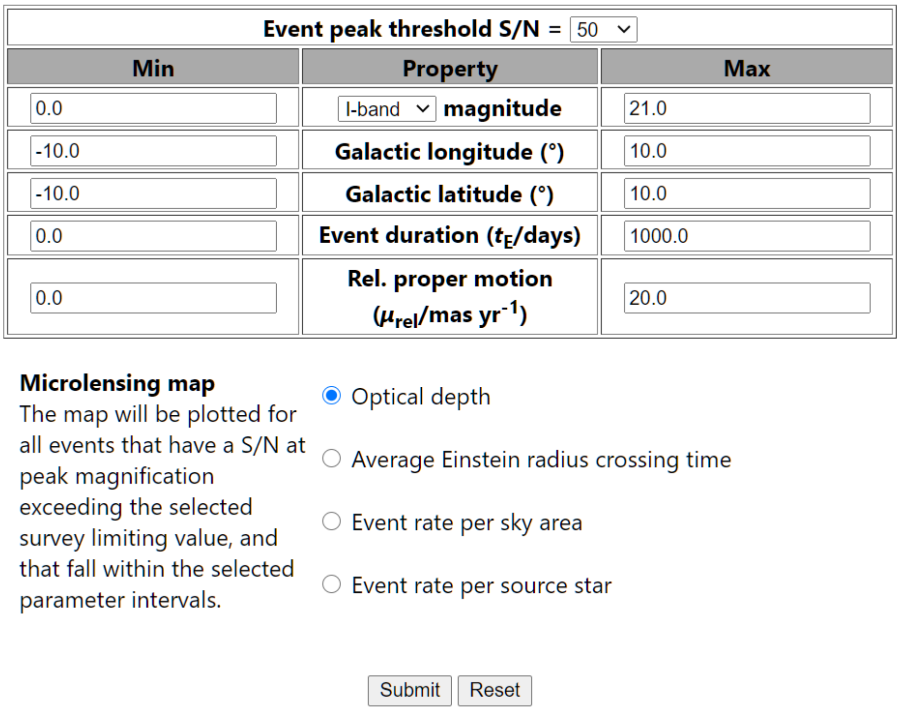

Event peak threshold S/N = 50

Min	Property	Max
0.0	I-band magnitude	21.0
-10.0	Galactic longitude (°)	10.0
-10.0	Galactic latitude (°)	10.0
0.0	Event duration (t_E/days)	1000.0
0.0	Rel. proper motion (μ_{rel}/mas yr^{-1})	20.0

Microlensing map
The map will be plotted for all events that have a S/N at peak magnification exceeding the selected survey limiting value, and that fall within the selected parameter intervals.

- ● Optical depth
- ○ Average Einstein radius crossing time
- ○ Event rate per sky area
- ○ Event rate per source star

FIGURE 2.10: Shown is the interface for the MaBμlS-2 online tool. The discreet parameters, signal-to-noise and Johnson-Cousins filter are available in drop-down menus, while the continuous variables, m_s, t_E and μ_{rel} are available as entry fields. The selection of map type is visible at the bottom.

the I-band t_E distribution with timescale were calculated, up to 1000 days and used as the bin edges. For μ_{rel}, the 20th percentiles of the I-band μ_{rel} distribution were calculated, up to 20 mas year^{-1} and used as the bin edges.

To produce the final product, interpolation must be performed as the user may specify magnitude, timescale and proper motion cuts along a continuous parameter space. In general, a bound will lie within a 3-dimensional bin, meaning both the upper and lower bounds must be interpolated within their respective bins. This leads to a sexilinear (6-dimensional) interpolation between $2^6 = 64$ integrals, three for the lower and three for the upper bound. Simplifications are made when the user specifies a cut that lies on a bin edge in any dimension. The result is a computationally efficient map generation method.

2.5 Comparison with OGLE-IV survey results

A test of the MaBμlS-2 simulation was performed by comparing results to that of the OGLE-IV survey, detailed in Mróz et al. (2019), which used a homogeneous sample of 8,000 microlensing events to construct maps of τ, $\langle t_E \rangle$ and Γ. This is in contrast to the original MOA-II results from Sumi et al. (2013), which attempted a similar analysis with a sample of 474 events. This increase in sample size of a factor 17 highlights the significance of this opportunity to test the Besançon model and MaBμlS simulation code. Figure 2.11 shows each of the parameter maps for τ, $\langle t_E \rangle$, Γ_* and $\Gamma_\circ$ over the I-band range $14 < I < 21$ and for $t_E < 300$ days. For a successful comparison between the

MaBμlS-2 simulation and the OGLE-IV survey, a $u_{\rm max}$ interpolation grid more faithful to the event selection criteria of the survey was necessary. The criterion used in the study required a time integrated signal-to-noise value $S/N_{3\sigma}$ summed over all fluxes greater than 3σ above a flat baseline to be greater than 32, defined as

$$S/N_{3\sigma} = \sum_i \frac{F_i - F_{\rm base}}{\sigma_i}\delta_i \geq 32, \tag{2.32}$$

$$\delta_i = \begin{cases} 1, & \frac{F_i - F_{\rm base}}{\sigma_i} > 3 \\ 0, & \text{else} \end{cases} . \tag{2.33}$$

A time integrated signal-to-noise requires knowledge of the cadence of the survey and the event timescale for the lens-source pair. As such, a 3-dimensional $u_{\rm max}$ interpolation grid was constructed, parameterised by the normalised source radius ρ, source magnitude $m_{\rm s}$ and the ratio of the cadence to the event timescale x, ignoring limb-darkening for simplicity. To estimate the value of $S/N_{3\sigma}$, each grid point needed to first calculate the time range over which the instantaneous signal-to-noise from equation 2.30 (evaluated at an arbitrary time as opposed to $t = t_0$ from equation 2.27) was greater than three. After this had been acquired numerically using a root-finding algorithm, a second root finding was performed, uniformly sampling the lightcurve at 11 locations (one at $t = t_0$ and five for each of the lightcurve's tails) and scaling the result to match the normalised cadence x. This was a computationally expensive operation, but once compiled, $u_{\rm max}$ could be easily sampled from this grid at run-time when generating the parameter maps. The results are shown in figure 2.12, which deviate from the equivalent maps using a signal-to-noise at peak magnification event selection, as in figure 2.8.

The residual between OGLE-IV and MaBμlS-2 was calculated to show the discrepancy between the data and the model. To highlight the statistical significance of the residual, it was normalised to the joint error, as shown in figure 2.13. To estimate the error on the residual at a particular (l, b), the standard deviation of all points within a donut shaped region was used, with an inner and outer radius $r_{\rm inner}$ and $r_{\rm outer} = 3r_{\rm inner}$ respectively. The inner radius prevents correlating the error calculation with the residual value itself and the outer radius prevents sampling the parameter map in locations not representative of the residual value. For the residual in τ, Γ_* and $\Gamma_\circ$, a value of $r_{\rm inner} = 15'$ was used, while the lower resolution $\langle t_{\rm E} \rangle$ map used a value of $r_{\rm inner} = 30'$.

An accurate model would have a 1-dimensional distribution of normalised residuals that closely matches a unit Gaussian with a mean of zero, which is achieved by τ, $\langle t_{\rm E} \rangle$ and Γ_*, with a notable under-prediction in $\Gamma_\circ$. A Gaussian width greater than unity, as evident in the first three parameter maps respectively, is a consequence of spatial variation across the map, such as from the over-prediction in Γ_* in the bulge and under-prediction elsewhere. This is in comparison to the legacy MaBμlS, shown in figure 2.14, optimised on MOA-II data, which models τ well, but shows an under-prediction in $\langle t_{\rm E} \rangle$ and over-predictions in Γ_* and $\Gamma_\circ$ as well as much stronger spatial variations. The discrepancy in $\langle t_{\rm E} \rangle$, which propagates to the event rates, most prominent at positive latitudes, is likely a result of the steeper brown dwarf mass function slope, which favours smaller timescales.

The largest tension between the MaBμlS-2 simulation and empirical data lies in the $\Gamma_\circ$ distribution, with a mean offset of 0.93 units, almost a full standard deviation. This deviation is most obvious outside the bulge, while the discrepancy reverses inside the bulge, showing a small over-prediction. Multiple factors could contribute to this tension; firstly, a source weighting insufficiently faithful to the conditions present in the OGLE-IV survey would directly impact $\Gamma_\circ$, which is proportional to the source weights, leaving other parameters less affected due to the presence of the source weights in the normalisation terms. Another origin of this tension could come from inaccuracies in the stellar IMFs, which dictate the average lens mass. The optical depth is independent of lens mass for a fixed $\phi(D_\mathrm{L})$, while the timescale obeys $t_\mathrm{E} \propto \sqrt{M}$; this is in contrast to source luminosity, which has a dependency upward of $L \propto M^4$, which would propagate to the calculation of N_* from equation 2.20.

2.6 MaBμlS-2 in Summary

The MaBμlS-2 simulation is a robust tool for probing Galactic structure and informing future microlensing surveys. It has improved significantly on its predecessor, MaBμlSby improving the event selection criteria, streamlining the simulation code through multiprocessing, implementing a rigorous error estimation and allowing for user selected parameter map cuts in the μ_rel parameter space. These additions and improvements allowed for a much more successful comparison to empirical data from OGLE-IV than the equivalent, much smaller sample MOA-II analysis from the original MaBμlS. Care was also taken to model the brown dwarf population to improve the low timescale tail of the t_E distribution, with a superior $\chi^2_\mathrm{red} = 1.5$ minimisation, yielding a mass function slope of 0.1, in contrast to the original, which achieved a $\chi^2_\mathrm{red} = 2.2$ and slope of -0.4, a discrepancy which was attributed to the differing survey characteristics and event selection between MOA-II and OGLE-IV.

With a successful prediction of the τ, $\langle t_\mathrm{E} \rangle$ and Γ_* maps when put to the test against empirical data, the MaBμlS-2 simulation has reinforced the precision of the Besançon Galactic model, falling short only in the $\Gamma_\circ$ map, where an under-prediction in event rate is evident outside of the Galactic bulge.

There are multiple avenues for extending this tool, such as allowing for cuts by lens brightness, which would further aid in breaking the microlensing degeneracy discussed in section 1.5 and 1.6. Although this tool uses finite source effects in evaluating the signal-to-noise event selection criterion, it does not mandate the detection of finite source effects; as such, the tool could be extended to allow the user to choose such a setting, which could further narrow the sample of viable microlensing events. Finally, using a general time integrated signal-to-noise criterion (such as employed specifically to compare with the OGLE-IV survey results in this work), while computationally slower due to the higher dimensionality of the u_max grid, would provide a more accurate estimation of event detectability, biasing more strongly in favour of longer timescale events.

The success of MaBμlS-2 has prompted further usage as an application in informing upcoming microlensing missions by the Euclid and Roman space telescopes, including modifications to incorporate the aforementioned finite source effect detection, work to which we shall now discuss in the next chapter.

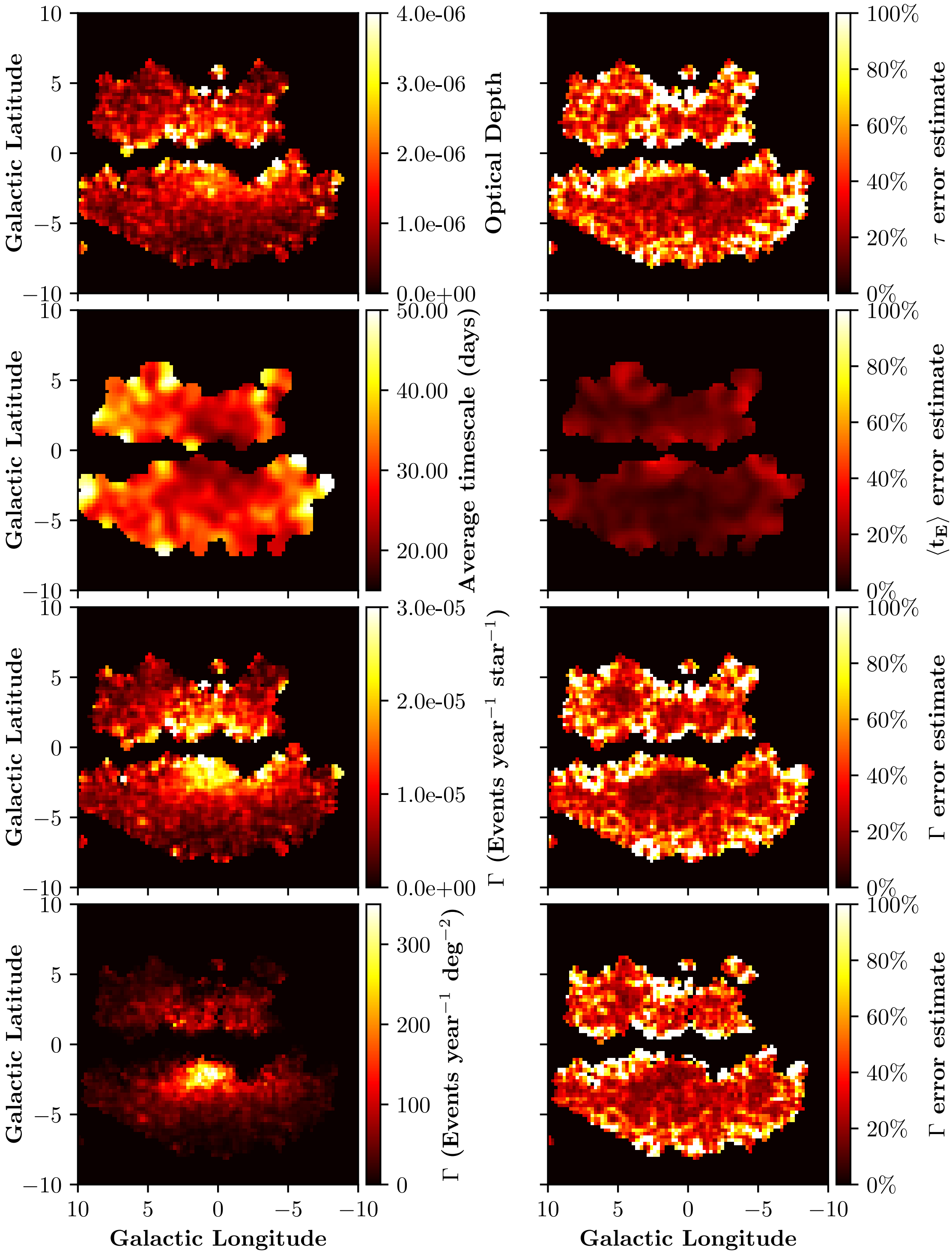
Galactic Latitude
10
5
0
−5
−10
Optical Depth
4.0e-06
3.0e-06
2.0e-06
1.0e-06
0.0e+00
τ error estimate
100%
80%
60%
40%
20%
0%
Average timescale (days)
50.00
40.00
30.00
20.00
⟨t_E⟩ error estimate
Γ (Events year−1 star−1)
3.0e-05
2.0e-05
1.0e-05
0.0e+00
Γ error estimate
Γ (Events year−1 deg−2)
300
200
100
0
Galactic Longitude
10
5
0
−5
−10

FIGURE 2.11: The OGLE-IV 8,000 event survey microlensing maps are shown in the left column with associated error maps on the right. Black regions indicate locations with no data.

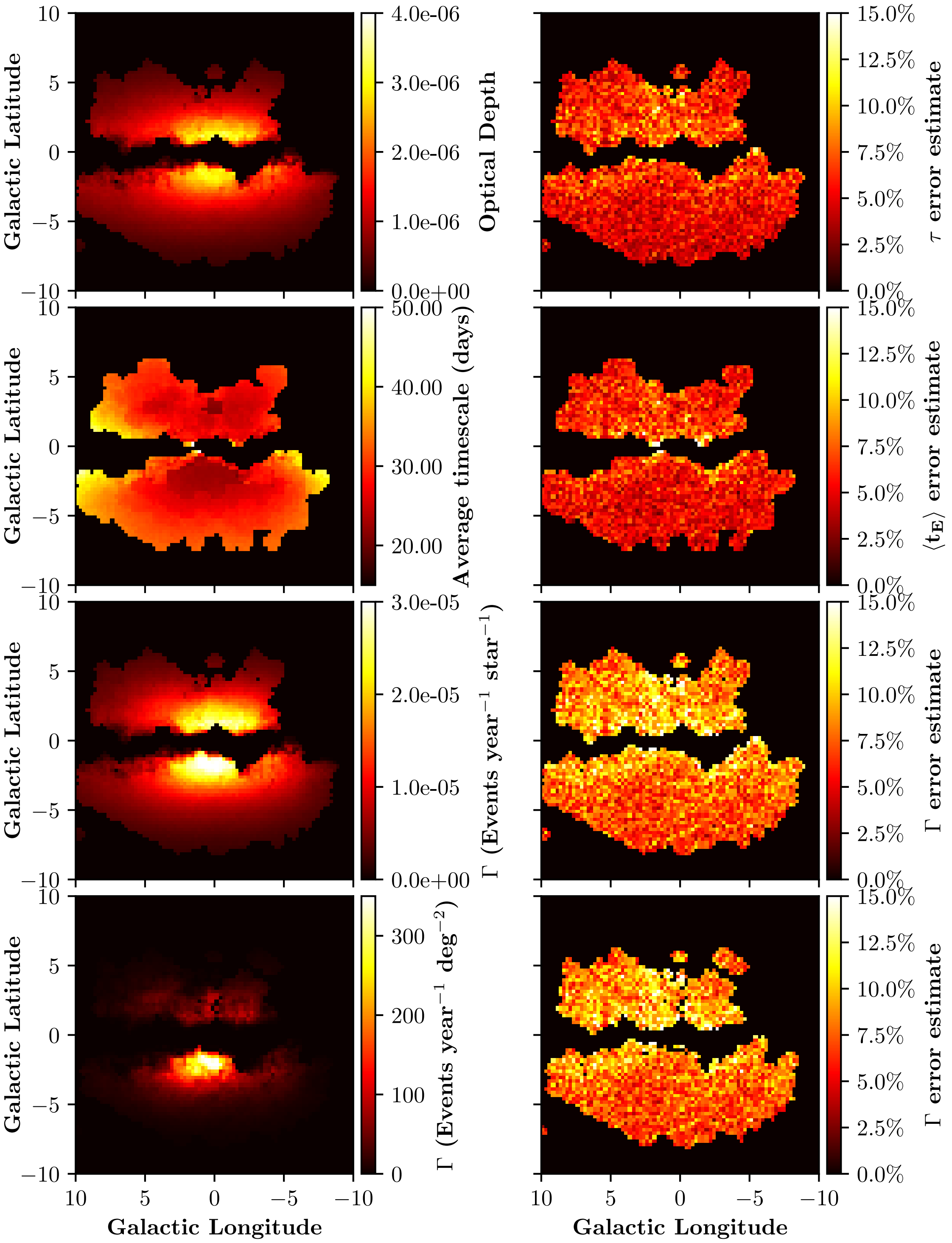
Galactic Latitude
Galactic Longitude
10
5
0
−5
−10
Optical Depth
4.0e-06
3.0e-06
2.0e-06
1.0e-06
0.0e+00
Average timescale (days)
50.00
40.00
30.00
20.00
Γ (Events year⁻¹ star⁻¹)
3.0e-05
2.0e-05
1.0e-05
0.0e+00
Γ (Events year⁻¹ deg⁻²)
300
200
100
0
τ error estimate
⟨t_E⟩ error estimate
Γ error estimate
15.0%
12.5%
10.0%
7.5%
5.0%
2.5%
0.0%

FIGURE 2.12: The I-band MaBμlS-2 parameter maps using equation 2.32 as the event selection criterion. The timescale map shows sharp contours where the cadence of the OGLE-IV survey changes. Sudden drops in timescale indicate that the cadence is high enough to resolve smaller timescale events. Source magnitudes were constricted between $14 < I < 21$ and timescales were kept $t_{\rm E} < 300$ days to represent the cuts made in the survey.

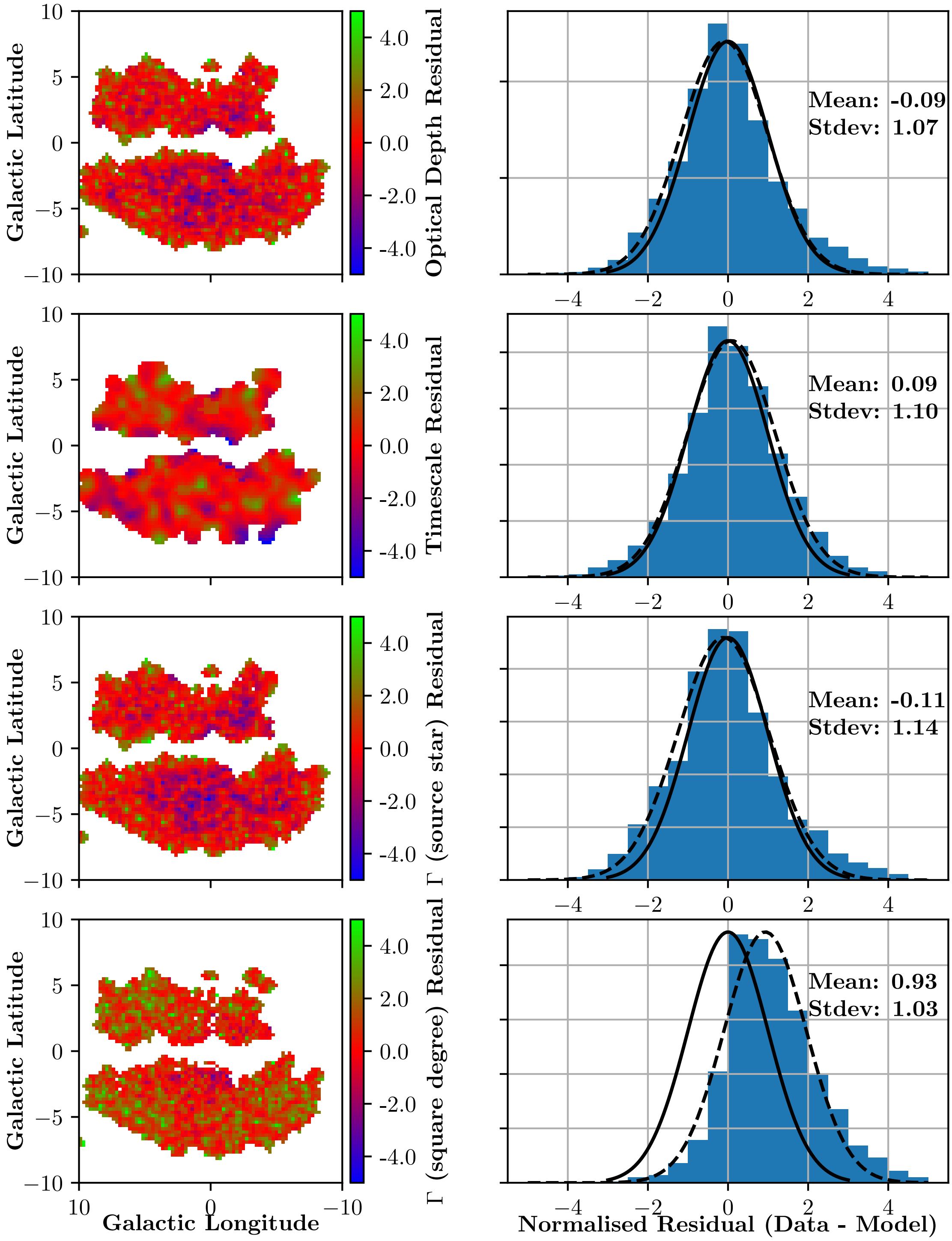

FIGURE 2.13: On the left is shown the residual between the OGLE-IV 8,000 event maps and the MaBμlS-2 equivalent, normalised to the error. Green regions suggests an under-prediction by the model, red suggests a good match and blue suggests an over-prediction by the model. Over-predictions tend to appear near the bulge, while under-predictions appear outside. The histograms to the right show the 1-dimensional distribution of residuals, with the means and standard deviations listed for the fitted Gaussians.

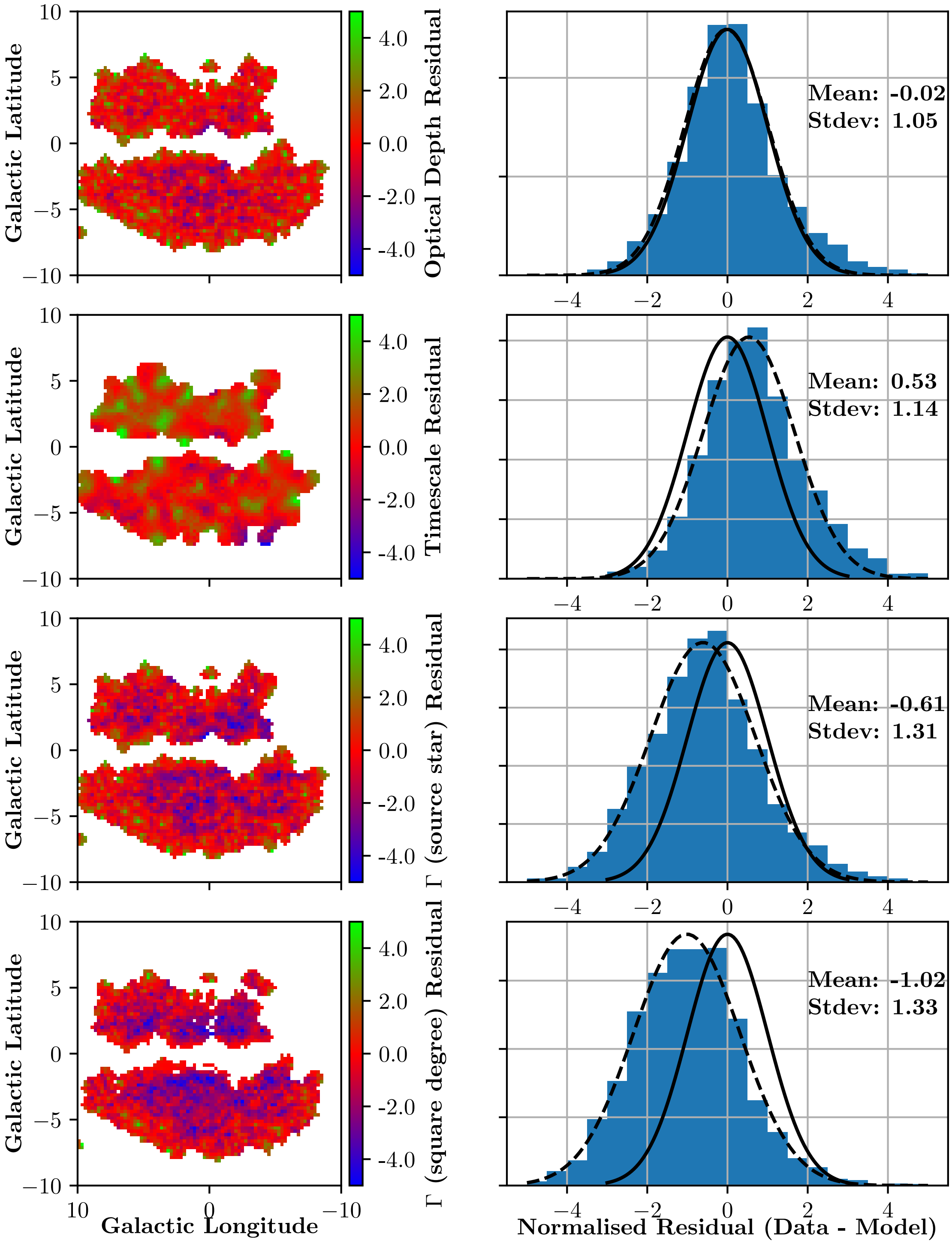

FIGURE 2.14: Same as figure 2.13, but comparing the legacy MaBμlS to OGLE-IV data. In this case there are much more powerful over-predictions near the bulge as well as some regions outside. This is attributed to the under-prediction in timescale rather than optical depth which shows good agreement with a slight over-prediction in the bulge.

Chapter 3

Detecting FFPs From Space

In this chapter, we will discuss the work done specifically on FFP detection rates in the work *Euclid-Roman joint microlensing survey: Early mass measurement, free floating planets, and exomoons* (Bachelet et al., 2022), of which the writer is a coauthor.

The tantalising possibility of large scale microlensing surveys by the upcoming EUCLID (Laureijs et al., 2010; Racca et al., 2016) and Nancy Grace Roman (formerly WFIRST and henceforth referred to as ROMAN, Goullioud et al. (2012)) space telescopes offers a unique opportunity to discover many new cold exoplanets, both bound to their host stars and unbound as free floating planets (FFPs). Assuming both telescopes will be orbiting the Sun-Earth L2 Lagrange point, these microlensing surveys could be combined to provide a space-based parallax measurement by monitoring an overlapping region of the sky. In cases where a measurement of finite source effects can be made, this would lead to a direct mass measurement of the lens object, allowing for a systematic attempt to characterise the FFP mass distribution and normalisation and place bounds on the FFP occurrence rate throughout the Galaxy.

Due to the significance of such a joint survey and given the immense resources invested in both telescopes, it is of utmost importance that the science return of such a survey is maximised. To this end, the MaBμlS-2 simulation code was adapted to produce event rate maps of the Galactic centre, particularly near Baade's Window, to predict the number of FFPs such a survey could detect with both a parallax signature and finite source measurement present in their lightcurves.

3.1 Space Telescopes

The NASA ROMAN Telescope's science goals include a study of dark energy, general infrared astrophysics and a dedicated exoplanet hunt using the microlensing method. The exoplanet survey will make use of ROMAN's Wide Field Instrument (WFI) and 2.4m mirror, specifically in the W146 infrared filter, covering a broad spectrum of $0.927 \rightarrow 2.00\mu m$, which is used in this work. The full width at half maximum of the filter's point spread function (PSF) is $\theta_{\rm PSF} \sim 0.12''$, with a corresponding solid angle of $\Omega_{\rm PSF} = 0.0456''^2$. The exposure time for each image will be $t_{\rm exp} = 46.8$s with a survey cadence of 15 min. The

TABLE 3.1: The parameters Ω_{psf}, m_{zp}, t_{exp} and μ_{sky} used in MaBμlS-2 from equations 2.27, 2.28 and 2.20 for the ROMAN W146, EUCLID VIS and NISP-H filters are tabulated below.

Filter	Ω_{psf}	m_{zp}	t_{exp} (sec)	μ_{sky}	Cadence (min)	Season (days)	Pixel Size (arcsec)
W146	0.0456	27.62	46.8	21.5	15	2×72	0.11
VIS	0.0254	25.58	270	21.5	60	2×30	0.10
NISP-H	0.159	24.92	54	21.4	60	2×30	0.30

sky brightness in W146 is $\mu_{\text{sky}} = 21.5$, with a zero-point magnitude (the magnitude at which one expects to receive a single count per second) of $m_{\text{zp}} = 27.62$ (Penny et al., 2019). The active field of view of the WFI is 0.28deg^2 and has a pixel size of 0.11″ (Spergel et al., 2015). The exoplanet campaign will consist of a pair of 72 day observing season annually. As of writing, ROMAN has a launch date in 2025.

Much like ROMAN, ESA's EUCLID Space Telescope aims to study dark energy, particularly with a focus on understanding the accelerating expansion of the universe via measurements of weak gravitational lensing and galaxy clustering. EUCLID's primary science goals do not include a dedicated microlensing campaign, although such a campaign is being considered as an additional science program a few years after its launch in 2022, allowing it, ideally, to overlap with ROMAN's microlensing exoplanet survey. EUCLID is equipped with a 1.2m mirror and two main instruments: the Visible Imager (VIS) (Cropper et al., 2016) and the Near-Infrared Spectrometer and Photometer (NISP) (Euclid Collaboration et al., 2022). The VIS filter covers wavelengths $0.55 \rightarrow 0.90\mu m$ across the optical spectrum, while the NISP instrument may select between either Y, J or H filters; this work focuses on the NISP-H filter. The VIS instrument has the longest exposure time out of the filters investigated in this analysis, at $t_{\text{exp}} = 270$s and also has the smallest pixel and PSF size at 0.10″ and 0.09″ respectively, in comparison to the NISP-H filter at 0.30″ and 0.22″, with an exposure time of $t_{\text{exp}} = 54$s. Of the two filters, VIS has the higher zero point magnitude with $m_{\text{zp}} = 25.58$ compared to NISP-H at 24.92, although due to its shorter wavelength, VIS struggles to penetrate Galactic dust while NISP-H largely ignores it. The EUCLID cadence is one hour, with observing seasons like ROMAN coming in two per annum, although with a smaller time window of 30 days per season (Penny et al., 2013). Details of both the EUCLID and ROMAN filters involved in this analysis are shown in table 3.1.

3.2 Free Floating Planets

The existence of gravitationally unbound exoplanet candidates has been known for more than two decades and was first reported in Oasa et al. (1999), which found objects with masses $M < 0.012 M_{\odot}$. Three further candidates were reported in Zapatero Osorio et al. (2000), with predicted masses in the range $5 < M < 15 M_{\text{Jup}}$. Although planetary in mass, the discoveries of these FFPs has been primarily driven by infrared imaging, relying on emissions due to the internal heat of the planet, suggesting a strong selection bias in

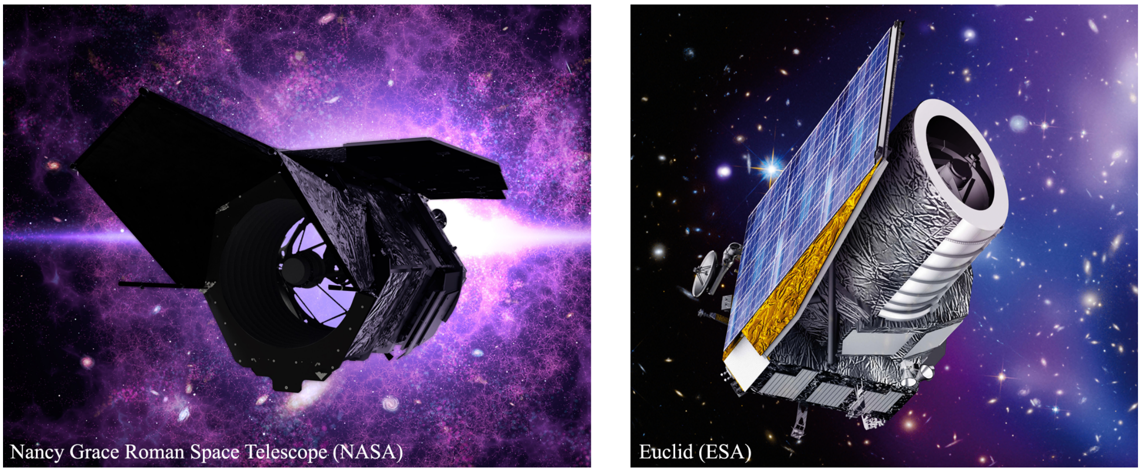

FIGURE 3.1: The Nancy Grace Roman Space Telescope (left, *credit: NASA*) and EUCLID Space Telescope (right, *credit: ESA*) are pictured.

favour of young FFPs at the largest planetary mass scales where direct imaging of thermal radiation is feasible. This method is in contrast to the direct imaging method discussed in section 1.2, which is used for bound exoplanets which also reflect light and receive heat from their host stars. In reality, the mass distribution of the Galactic FFP population is not well constrained, with planetary formation models predicting a significantly higher abundance of Earth mass FFPs, between $0.3 \rightarrow 1 M_{\oplus}$ (Ma et al., 2016; Barclay et al., 2017). Two popular theories of the origin of FFPs are the core-collapse model (Padoan & Nordlund, 2002; Hennebelle & Chabrier, 2008) involving a scaled down version of the stellar formation and the dynamical scattering model (Veras & Raymond, 2012), involving gravitational scattering from close encounters of planets in a bound system, or by the intrusion of other stars from a dense birth cluster, resulting in the ejection of one of the planets into interstellar space. Recent work by Miret-Roig et al. (2022) suggests that the core-collapse model is insufficient by a factor seven to explain the abundance of FFPs observed through direct imaging and that dynamical scattering, among other possibilities, may be contributing to the Galactic FFP population.

Detecting FFPs instead via their gravitational microlensing signature allows for the detection of FFPs with significantly lower masses, likely down to Earth mass, as well as FFPs at further distances, potentially kiloparsecs away from the Solar System. Although no dedicated FFP microlensing survey has been yet conducted with the capacity to directly measure FFP masses, several surveys have been conducted that characterise the event timescale distribution of detected microlensing events and exhibit a low timescale excess which could be attributed to an FFP population, although this is contentious. The first such investigation was conducted by Sumi et al. (2011), which analysed 474 high quality events from the MOA-II microlensing survey. The resulting timescale distribution was consistent with either a power-law or log-normal FFP mass distribution, with a best fit of $1.8^{+1.7}_{-0.8}\, M_{\rm Jup}$ mass FFPs per main sequence star. This hypothesis was later contested by Mróz et al. (2017), which used a sample of 2617 microlensing events from the OGLE-IV survey and found no statistically significant timescale excess consistent with a

Jupiter mass FFP population with occurrence rates proposed by the Sumi study, with a best fit of 0.05 Jupiter mass FFPs per main sequence star. It did however find tentative evidence of an Earth mass FFP population, consistent with a normalisation of 10 FFPs per main sequence star. Throughout this work, we shall investigate the expected mass-measured event rates of the Sumi and Mróz models consisting of Dirac delta FFP mass distributions centred on Jupiter and Earth masses, with normalisations of 2 and 10 FFPs respectively, under a joint microlensing survey between EUCLID and ROMAN.

3.3 Modifying MaBμlS-2

In chapter 2, we described how the BGM population synthesis model can be used to make predictions about the microlensing event rate, among other parameters. While this simulation improved much on past work, for example by considering finite source effects in an estimation of the requisite signal-to-noise, it falls short of being adequate for assisting in the search for FFPs by microlensing. As we are primarily interested in characterising the FFP mass distribution shape and normalisation, we will need to be able to measure the lens mass. The equation 1.5 for θ_E is insufficient to acquire M_L without relying on first order effects, namely the finite source and microlensing parallax phenomena. Using equations 1.21 and 1.32, we can express the lens mass in terms of parameters we can measure or fit to a lightcurve,

$$M_\mathrm{L} = \frac{\theta_*}{\kappa \pi_\mathrm{E} \rho}. \tag{3.1}$$

Another crucial factor to consider when maximising the science return from a microlensing survey is the field location. Baade's window, due to the relatively small amount of obscuring dust, is a popular location for microlensing searches and as such, was the central location for the bespoke MaBμlS simulation, with $11 \times 17 = 187$ lines of sight spanning $-1.5 < l < 2.5^\circ$ and $-2.5 < b < 0^\circ$. This choice has been reinforced by the results of Specht et al. (2020) and Awiphan et al. (2016), which show the highest event rates in this region, albeit without finite-source and parallax detection constraints. Given the 40,000 stars per line of sight specification from chapter 2, this provides approximately 150 billion simulated lens source pairs for consideration within this region of the sky, allowing for a high precision analysis of FFP event rate.

While each of these source stars have magnitudes calculated in the Johnson-Cousins *UBVRIJHK* filters, neither the ROMAN W146 nor EUCLID VIS magnitudes are available options for the output of BG1307. The approximation of VIS was simply taken to be the Johnson-Cousins R band due to its similarity, whereas calculating the ROMAN telescope's W146 magnitude was more involved due to its large bandwidth. To do this, an approximation was made by using a combination of the Johnson-Cousins H and J bands by considering the integrated transmission curves of H, J and W146, shown in figure 3.2. These were combined in flux units and converted back into the W146 magnitude m_w146 via

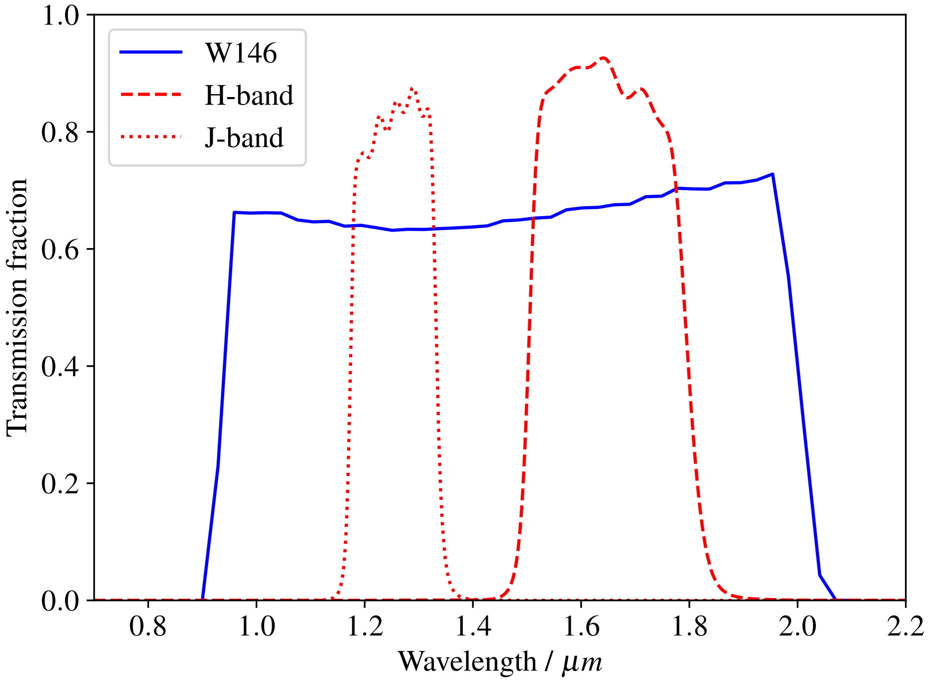

FIGURE 3.2: The W146 filter, showing its transmission curve (blue) superimposed with the Johnson-Cousins H (dashed red line) and J (dotted red line). The data used to compile ROMAN's W146 transmission curve is made available by NASA online at `https://roman.gsfc.nasa.gov/science/Roman_Reference_Information.html`

$$m_{\mathrm{w146}} = -2.5log_{10}(10^{-0.4m_J} + 10^{-0.4m_H}) + \delta_m, \tag{3.2}$$

where $\delta_m = -0.647$ represents the magnitude difference induced by the differing integrals of the transmission curves.

3.3.1 Signal-to-noise criteria

Much like the standard MaBμlS-2, a general signal-to-noise event selection criterion is required to screen out lens-source pairs that cannot be detected by the survey optics. For this analysis, a time integrated signal-to-noise criterion was employed, mandating that a microlensing event produce at least a $\Delta\chi^2 > 125$ between a constant baseline flux model and a FSPL (finite source, point lens) model. In addition to this, to screen out events with large ρ which may pass this criteria without producing a significant peak, it was also required that 6 points reach a signal-to-noise of greater than 3σ from the baseline flux.

A precompiled 3-dimensional u_{max} grid incorporating these criteria was produced, with sampling parameters m_{s}, ρ and $\frac{t_{\mathrm{cad}}}{t_{\mathrm{E}}}$, using a resolution of 20 points on each axis. The axis ranges are shown in table 3.2.

Parameter	Minimum	Maximum	Grid spacing
ρ	0	5	Linear
m_s	16	25	Linear
t_{cad}/t_E	10^{-2}	1	Logarithmic

TABLE 3.2: The signal-to-noise u_{max} grid parameters are listed with their axis ranges and grid spacing distribution. Each axis was sampled with a resolution of 20 points.

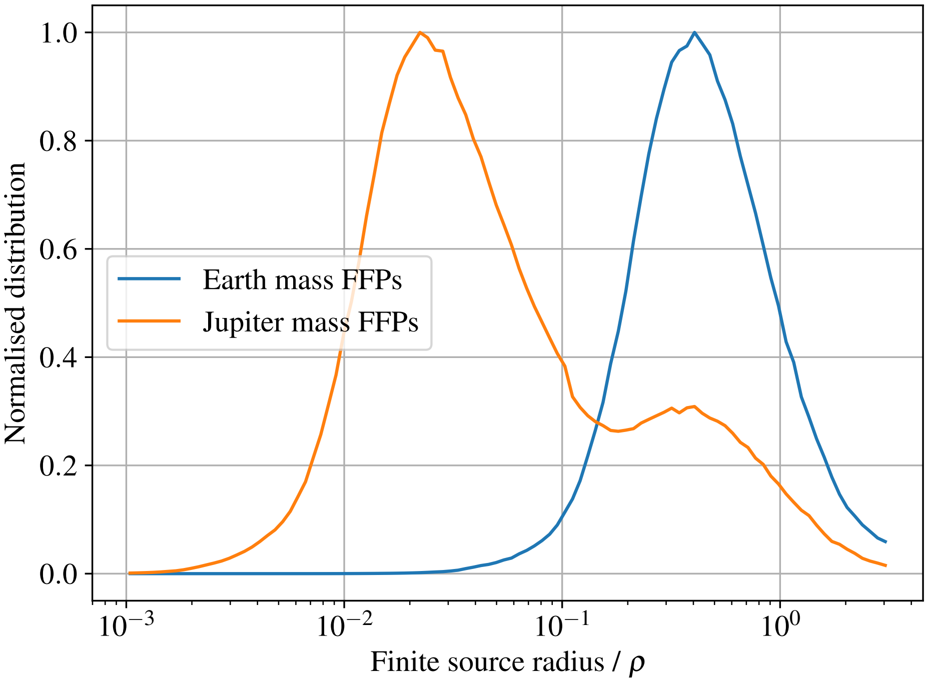

FIGURE 3.3: Shown are the distributions of ρ assuming Earth mass (blue line) and Jupiter mass (orange line) FFPs, weighted using the rate-weight parameter w^p from equation 2.15. The offset in ρ of the peaks of each distribution is, as expected, equal to $\sqrt{M_J/M_\oplus}$ as the Einstein radius is proportional to $\sqrt{M_L}$. Of note is the second mode of the Jupiter distribution centred around $\rho = 0.5$, which represents the population of lens-source pairs both in the Galactic bar, where the relatively small distance between them reduces θ_E. As it is difficult for large finite source radii to meet the minimum magnification requirements demanded by the signal-to-noise selection criterion, the Earth equivalent of the bar-bar population is suppressed.

Parameter	Minimum	Maximum	Grid spacing
ρ	10^{-5}	5	Logarithmic
m_s	16	25	Linear
$t_\mathrm{cad}/t_\mathrm{E}$	10^{-2}	1	Logarithmic
N_BG	100	10^6	Logarithmic

TABLE 3.3: The parameter ranges for the finite source detection u_max grid. The event timescale was normalised to the cadence of the particular telescope (either EUCLID or ROMAN), allowing for a determination of the number of number of data-points within t_max either side of t_0. Each axis had a resolution of 10 grid points.

3.3.2 The finite source measurement

Although MaBμlS-2 uses finite source effects when calculating the required signal-to-noise of an event to meet selection criteria, it does not mandate that finite source effects be detected. To accommodate this new requirement and hence only allow for microlensing events that could realistically yield a direct θ_E measurement, a $\Delta\chi^2$ of greater than 100 between a PSPL model and finite source model was mandated. Implementing this as a feature of the MaBμlS-2 simulation involved constructing a new 4-dimensional u_max grid, with sampling parameters ρ, t_E and N_BG (the background photon count from equation 2.29) logarithmically distributed and m_s linearly distributed, with a resolution of 10 points on each axis. Parameter ranges are tabulated in table 3.3. The grid was then built by iterating over the 3D parameter space and numerically solving for u_max to produce a $\Delta\chi^2 = 100$ between the PSPL and finite source lightcurves. As both microlensing models tend to a magnification of 1 for large impact parameters, the χ^2 was only evaluated over a time range of

$$t_\mathrm{max} = 2t_\mathrm{E} \times max(1, \rho). \tag{3.3}$$

As the cadence t_cad of the telescopes did not in general divide evenly into the event timescale, 11 lightcurve samples were taken on the right side of the lightcurves from $t = t_0 \rightarrow t = t_\mathrm{max}$, doubling the resulting χ^2 for each point to include the contribution from the symmetrical left sides (excluding the central point at $t = 0$) and then scaling the result by a factor $f = \frac{t_\mathrm{max}}{10 \times t_\mathrm{cad}}$.

3.3.3 Introducing a parallax measurement

The other critical component required to obtain a lens mass measurement is the microlensing parallax. To this end, a 5σ detection of π_E was mandated, using the Fisher information matrix method employed by Bachelet et al. (2018) and Mogavero & Beaulieu (2016). This method allows for an analytical estimate of a covariance matrix of the microlensing parameters used in the parallax model, by evaluating the elements of the Fisher information matrix M, summed over k data-points. Each element of the Fisher matrix involves the derivatives of the observed source flux F, given by

$$F = F_{\mathrm{s}}A(t) + F_b, \tag{3.4}$$

where F_{s} is the non-blended baseline source flux and F_b is the blending flux. Derivatives of F are with respect to the microlensing parameters θ_x for a parallax model, where x denotes the index of a matrix row or column, through

$$M_{i,j} = \sum_{k=1}^{N} \frac{\partial F_k}{\partial \theta_i} \frac{\partial F_k}{\partial \theta_j} \frac{1}{\sigma_k^2}, \tag{3.5}$$

with the parameter σ_k^2 representing the error on the flux for data-point k. The covariance matrix, containing the estimated errors of each parameter assuming they are Gaussian distributed, is then acquired by inverting M. It is from this covariance matrix that we can then acquire an estimate for the error on the microlensing parallax, as

$$\sigma_{\pi_{\mathrm{E}}}^2 = \frac{\sigma_{\pi_{\mathrm{E,E}}}^2 + \sigma_{\pi_{\mathrm{E,N}}}^2}{2} - \frac{\sqrt{(\sigma_{\pi_{\mathrm{E,E}}}^2 - \sigma_{\pi_{\mathrm{E,N}}}^2)^2 + 4cov(\sigma_{\pi_{\mathrm{E,E}}}, \sigma_{\pi_{\mathrm{E,N}}})^2}}{2} \tag{3.6}$$

Enforcing the 5σ detection of π_{E} is then simply achieved by requiring $\frac{\pi_{\mathrm{E}}}{\sigma_{\pi_{\mathrm{E}}}} > 5$. Although a useful metric of parallax detectability, this constraint must be implemented over hundreds of billions of lens-source pairs, which is not a computationally tractable operation to perform during the production of the modified MaBμlS-2 event rate maps of the region of interest. To account for this, another u_{max} grid was produced, this time using six input parameters: the EUCLID (either the VIS or NISP filters) and ROMAN source magnitudes m_{E} and m_{W146}, the event timescale t_{E}, the normalised source radius ρ, the magnitude of the microlensing parallax and the angle ϕ between the projected baseline and the $\hat{\mu}_{\mathrm{rel}}$ vector. A numerical root finding algorithm was then performed to compile this six-dimensional u_{max} grid before running the simulation, much like the signal-to-noise and finite source detection u_{max} grids. The parameter ranges and grid spacings are listed in table 3.4. To produce the simulated lightcurves from both telescopes for this calculation, the magnification using a finite source model in the case of $\rho > 0$ or PSPL model in the case of $\rho = 0$ was evaluated using the cadences of each telescope listed in table 3.1.

3.4 Results

To illustrate the effect of introducing more event selection criteria on the total FFP event rate, the modified MaBμlS-2 simulation was performed with four configurations: using only the signal-to-noise (S/N) selection criteria, the S/N and finite source detection criteria, the S/N and parallax signature detection criteria and the final simulation using the S/N, finite source and parallax signature detection criteria, with only the latter configuration allowing for a direct mass measurement of the lens as discussed in sections 1.5 and 1.6.

Parameter	Minimum	Maximum	Grid spacing	No. Grid Points
$m_{\rm E}$	16	25	Linear	10
$m_{\rm W146}$	16	25	Linear	10
ρ	0	5	Linear	5
$t_{\rm E}$	0.02	6	Linear	10
$\pi_{\rm E}$	10^{-4}	1	Logarithmic	10
ϕ	0	2π	Linear	5

TABLE 3.4: The parameter ranges for the parallax detection $u_{\rm max}$ grid are shown, as well as the number of grid points used. Due to the high number of dimensions, the grid resolution was reduced to 5 grid points on axes which produced only gradual and smooth changes in $u_{\rm max}$, resulting in a more accurate $u_{\rm max}$value when linearly interpolated. For other axes, the resolution was kept at 10 points in the case that the variation in $u_{\rm max}$was less accurately evaluated using linear interpolation at run-time.

After the modified MaBμlS-2 simulation had been run, event rate maps for each line of sight in the region of interest were produced. Although at that stage the most significant computational work had been completed, the task still remained to optimise for the ideal field placement locations for EUCLID and ROMAN. Due to the complexity of optimising both telescope's field locations simultaneously, we used the ROMAN field locations acquired by Penny et al. (2019) for ROMAN's proposed Cycle-7 science mission. This configuration uses seven contiguous fields, each with curved borders to account for the instrument's curved focal plane, oriented in the Galactic coordinate system to maximise the $1M_\oplus$ FFP detection rate, as shown in figure 3.5. The field centroid locations found are listed in table 3.5 and used in this work.

Optimising the EUCLID field locations was then necessary to maximise the FFP detection rate within the intersection of both the EUCLID and ROMAN fields. The shape of an individual EUCLID field was taken to be rectangular, with a width of 0.38° and height of 0.36°. As we do not know a-priori the EUCLID field orientations, to demonstrate that a joint EUCLID-ROMAN microlensing survey would still be able to generate significant science even with misaligned fields it was decided that EUCLID fields would be oriented in the Ecliptic coordinate system, inducing a 60° rotation relative to the ROMAN fields. To produce a large enough overlap between the fields of the two telescopes, it was decided to use four contiguous EUCLID field placements.

The optimisation process was performed in four stages, one for each of the field locations; to begin with, each of the four fields were distributed approximately evenly across the area already covered by the ROMAN fields, although not contiguously. A function was then used which, given four input locations, produced four output locations which obeyed contiguity, a process illustrated in figure 3.4. This function worked by keeping the first location stationary, and then sequentially placing the other fields such that they were moved the minimum distance possible to touch the previously placed fields. To optimise the field locations, the derivative-less Nelder Mead method was used, taking the l and b coordinates of each field as optimisation parameters, making for a total of 8 parameters. For each iteration of the optimisation, the contiguity function was used before the event rate map was sampled at a resolution of 0.02° with bicubic interpolation

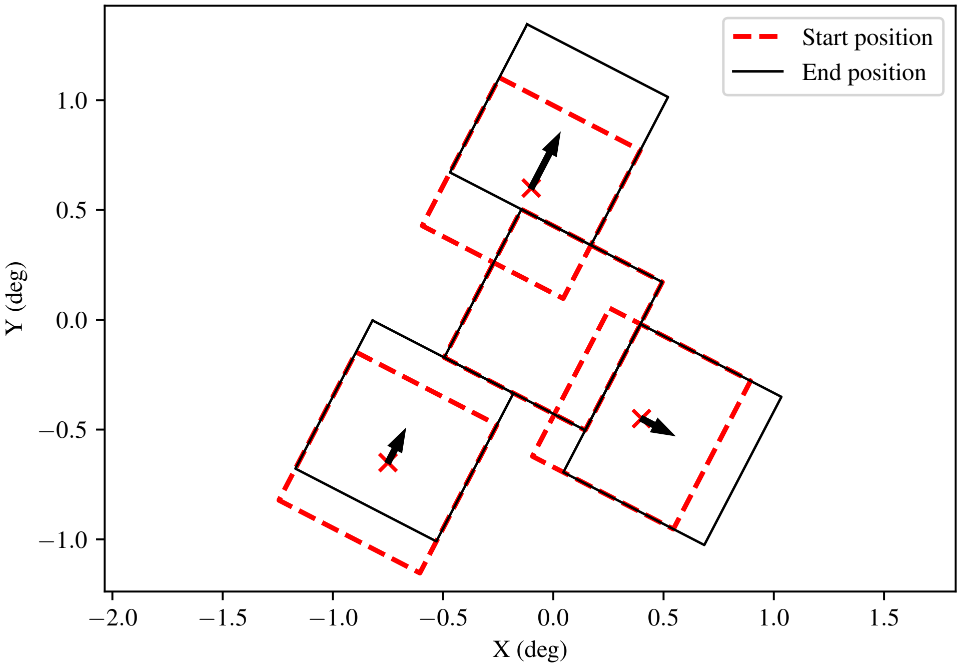

FIGURE 3.4: Illustration of the contiguity enforcing algorithm. Fields are initially placed at guess locations, outlined with red dashed edges. A single field is chosen as a primary field, retaining its initial position. Other fields are then shifted along an axis the shortest distance possible to their final positions outlined with a solid black line, such that they touch any previously adjusted fields and form a contiguous region. The black arrows indicate the position deltas added to each field in order to enforce this contiguity.

l (deg)	0.60	0.19	1.01	1.01	1.41	-0.22	1.41
b (deg)	-1.64	-1.64	-1.64	-0.85	-0.85	-1.64	-1.64

TABLE 3.5: Centroid locations of the ROMAN Cycle-7 fields in Galactic (l, b) coordinates, evaluated in the work done by Penny et al. (2019).

across the area of the intersection of the EUCLID and ROMAN fields. The high resolution was necessary to correctly resolve the intersection shape, as any sample falling outside of this intersection did not contribute to the total evaluated rate for that configuration.

As the contiguity enforcing function produces different results depending on the input order of the four test field locations, the optimisation was performed $4! = 24$ times, once for every arrangement of starting locations. The best performing configuration was then selected out of each of these 24 results. As the MaBμlS-2 simulation produced the highest rates in the EUCLID NISP (H) filter, the Earth mass FFP rate map constrained by all three event selection criteria in the NISP filter was selected as the fiducial event rate map used for EUCLID field optimisation, with results shown in table 3.6.

l (deg)	0.79	1.14	1.57	-0.03
b (deg)	-1.56	-0.89	-1.64	-1.60

TABLE 3.6: Centroid locations of the EUCLID fields in Galactic (l, b) coordinates selected after optimisation.

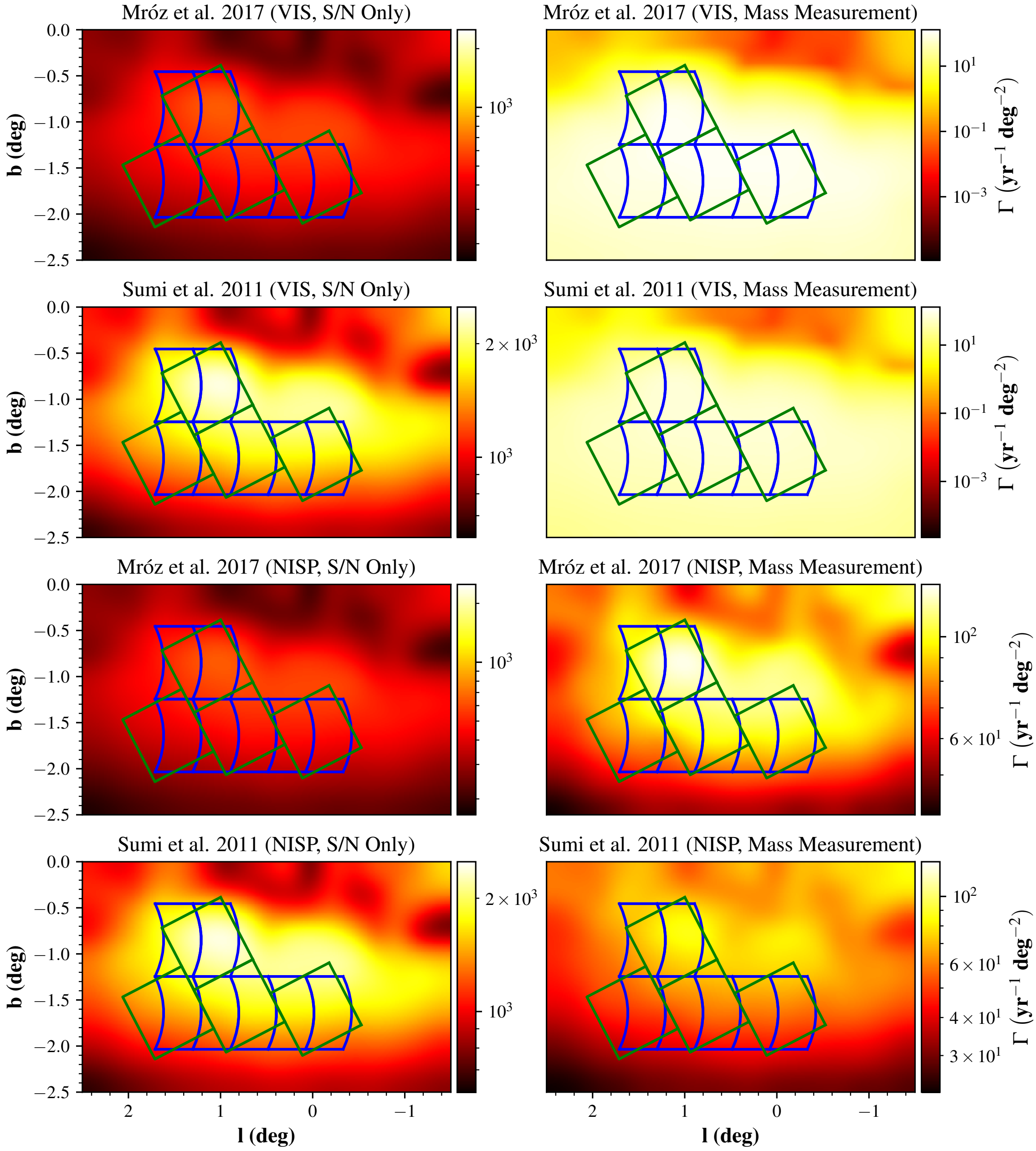

FIGURE 3.5: Various FFP event rate maps produced by MaBμlS-2 are shown, with the event rate displayed on a logarithmic scale. The ROMAN fields are drawn with blue lines, while the EUCLID fields are drawn in green. On the left column, rate maps using only the signal-to-noise event selection criterion are shown, while the right column displays rate maps using all event selection criteria allowing for a direct mass measurement. The top two rows show rate maps using EUCLID's VIS filter and ROMAN's W146, while the bottom two rows use EUCLID's NISP (H) filter. Earth mass FFP maps following the Mróz model are shown on rows one and three, with the Jupiter mass Sumi model displayed on rows two and four.

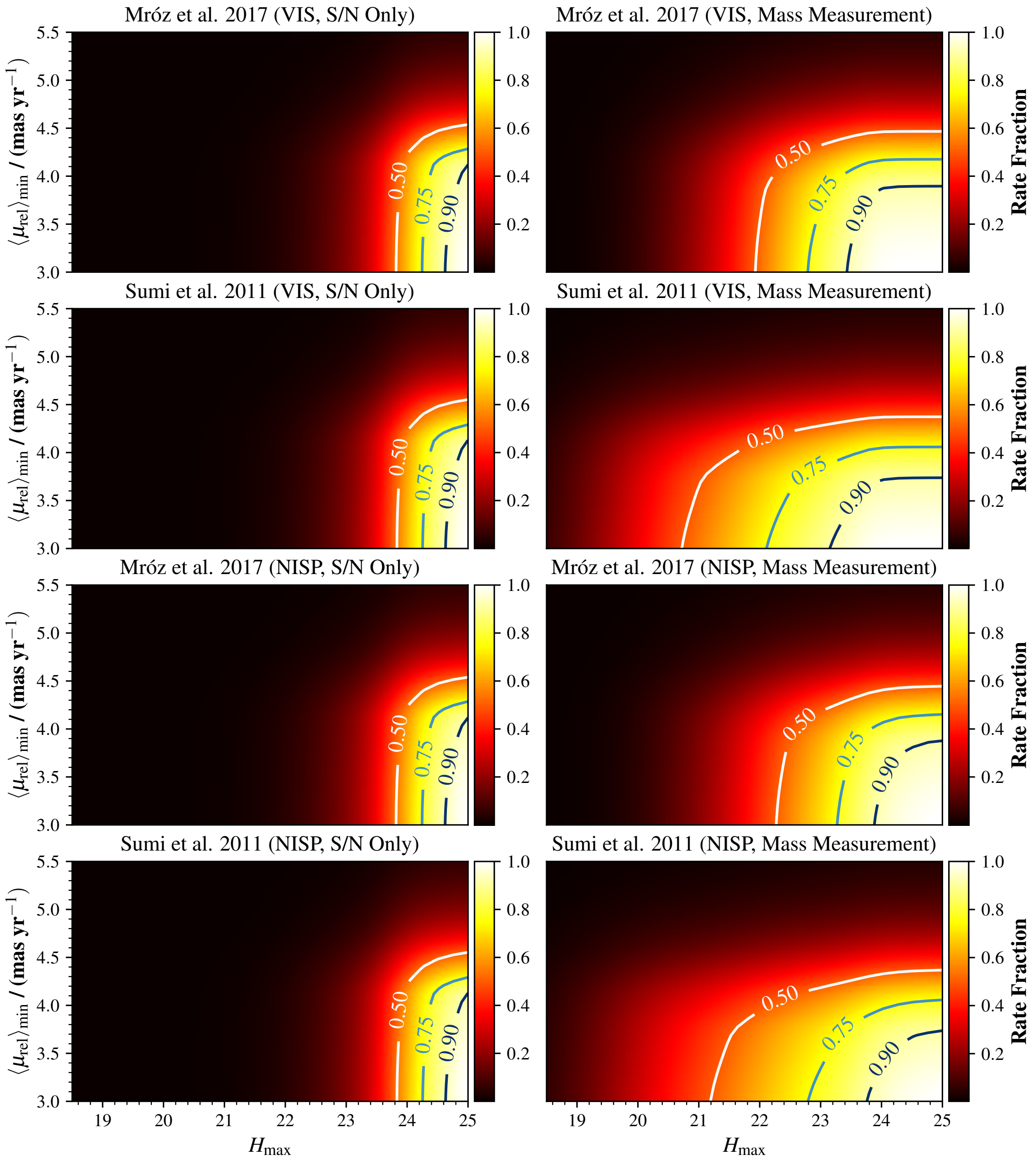

FIGURE 3.6: The cumulative event rate fraction distributions are shown, with each distribution corresponding to the rate map of the same row and column from figure 3.5. On the x-axis is the maximum H-band magnitude of source stars, with the minimum expected lens-source proper motion $\langle\mu_{\rm rel}\rangle_{\rm min}$ on the y-axis. For reference, the 50, 75 and 90 percentile boundaries are shown.

Model	Filter Combination	S/N	S/N + Parallax	S/N + Finite Source	Mass Measurement
Jupiter mass	W146 + VIS	490	450	18	18
Sumi (2011)	W146 + NISP (H)	490	450	19	19
Earth mass	W146 + VIS	130	110	28	28
Mróz (2019)	W146 + NISP (H)	130	110	31	31

TABLE 3.7: The annual FFP detection rates are shown tabulated for each model, combination of filters and combination of simulated event selection criteria. Numbers represent the total detections over the two 30 day observing seasons of the EUCLID telescope, coinciding with the two 72 day observing seasons of ROMAN, per annum. The finite source detection bottleneck is obvious as most events should produce a 5σ parallax signature, but do not allow for a mass measurement. The difficulty of detecting finite source effects among more massive lenses is also highlighted in this table, given the contrast in rates between the signal-to-noise (S/N) only and mass measurement columns for Jupiter and Earth mass FFPs.

The FFP event rates with the ROMAN and optimised EUCLID fields are shown in figure 3.5, with results for each scenario tabulated in table 3.7. From the rate maps, it is clear that the Sumi model, with two Jupiter mass FFPs per main sequence star produces a significantly higher event rate compared to the Mróz model (ten Earth mass FFPs per main sequence star) when considering only the signal-to-noise criteria, by a factor ~ 4. This is in line with expectations from the PSPL model, which predicts a factor $\sqrt{M_\text{J}/M_\oplus} \approx 18$ in favour of the Jupiter mass FFP model, assuming the same FFP occurrence. This discrepancy diminishes and somewhat reverses when introducing the finite source detection criteria, with the Mróz model performing better by a factor 1.5 compared to the Sumi model (although worse by a factor three when accounting for occurrence rates). This is primarily due to the fact that the detection of finite source effects depends on $\frac{u_0}{\rho}$ approaching unity or less, rather than any dependence on the size of θ_E, which compensates for the discrepancy in optical depth at the different FFP mass scales. Although marginal, the EUCLID NISP filter produced a higher event rate compared to the VIS filter. This is due to the higher wavelength of the NISP H filter allowing for more visibility through Galactic dust, which compensates for NISP's lower exposure time.

Another analysis performed was to consider how the cumulative event rate changes as a function of maximum H-band magnitude and minimum expected relative proper motion $\langle\mu_\text{rel}\rangle_\text{min}$. From figure 3.6, we can see that the structure of the cumulative rate is invariant to FFP mass in the case that only the signal-to-noise selection is used, with stars brighter than $m_H = 23.8$ at typical μ_rel contributing 50% of the total event rate. This is in contrast to the mass measurement yielding event rates, which show an offset of $\delta m_H = 1$ between the Sumi and Mróz, with the Sumi model producing 50% of events around $m_H = 21.2$ for typical μ_rel and the Mróz model $m_h = 22.2$. This discrepancy is due primarily to the finite source detection criterion, as a large ρ induces a greater $\delta\chi^2$ between a PSPL and FSPL model for the same u_0, thus requiring a brighter source to meet the criterion.

Of note is the effect of the parallax criterion and its minimal effect on the mass-measurable event rate, given that the finite source detection represents a much greater bottleneck. This implies that even without a finite source measurement, $\sim$ 90% of FFP events will still yield a 5σ $\pi_{\rm E}$ measurement, the distribution of which can be used to help constrain the FFP mass function and normalisation.

We can compare these results with the work of Ban (2020), which calculated event rates for the EUCLID and ROMAN space telescopes, as well as the Vera Rubin Observatory on Earth, along a single line of sight at $(l, b) = (1, -1.75)$. In that work, two event selection criteria were employed: a signal-to-noise at event peak of $S/N > 50$ and a parallax detection of greater than 5σ, determined by the maximum differential amplitude between the lightcurves from the two telescopes and the corresponding error. Although finite source effects were taken into account when calculating the peak signal-to-noise value, no finite source measurement was required when evaluating the final event rate. As such, we can compare the results from this work which also ignore finite source effects, and considering occurrence rates of only a single FFP per main sequence star. We find good agreement among Earth mass FFPs, with a rate of 5.2 events per annum for this work, and 4.9 for Ban's work. This is in stark contrast however, when comparing Jupiter mass FFPs with this work predicting a rate of 104 events per annum, compared to only 31 events for Ban's work. This difference is explained primarily by the differing signal-to-noise criteria, as this work considers a time integrated signal-to-noise, which prefers longer time scale events such as those produced by heavier, Jupiter mass FFPs. The differences in the parallax detectability criterion are similar, with this work considering the full series of photometry, while Ban's work considers only the greatest difference in observed flux between lightcurves, although this discrepancy ultimately played a smaller role in the final reported event rates between the two studies.

A further comparison can be made with the detection rates reported in Johnson et al. (2020), which models the FFP event rate for ROMAN across a range of masses between $0.1M_{\oplus} < M < 10^3 M_{\oplus}$. Although Johnson did not study parallax, the detection of finite source effects was considered. Of note is the cumulative event rate for each FFP mass model as a function of $\frac{\rho}{u_0}$, which suggests that for the fraction of Earth mass FFP events in this work with measureable finite source effects (approximately 20%), our event selection criteria allows for $\frac{\rho}{u_0} \sim 0.3$. This is also consistent with the Jupiter event rate, with only 4% exhibiting finite source effects in this work and $\sim$ 5% for a $300M_{\oplus}$ FFP in Johnson's study. Another point of comparison is the predicted event rate using only signal-to-noise event selection criteria. Johnson reports, for six 72 day ROMAN observing seasons at an FFP occurrence of one per main sequence star, a cumulative event rate of 88.3 Earth mass FFPs. Correcting for FFP occurrence and observation time, this work predicts 93.6 Earth mass FFPs, a 6% increase. For Jupiter mass FFPs, this work predicts 1764 events, while Johnson predicts 2200, a 20% decrease. This difference is driven primarily due to the difference in event selection criteria, with Johnson using a more strict threshold of $\Delta\chi^2 > 300$ and the Galactic model employed to produce the FFP lenses. The former factor tends to favour the rates in this work, while the effect of the latter is harder to discern due to the complexity of the Besançon model, but is likely responsible for the larger Jupiter mass detection rate.

With potentially dozens of FFP mass measurements per annum of a joint EUCLID-ROMAN mission, it is clear that the next generation of microlensing surveys offer a unique opportunity to characterise the FFP mass distribution, or in the case of a smaller occurrence rate than proposed by the Sumi or Mróz models, provide bounds on the mass distribution to a precision greater than can be achieved through direct imaging. As such, this proposed mission has the potential to discover the existence of a new component to our Galaxy, which will provide a deeper insight into the formation of planets around the cosmos.

In spite of this promise, one key question remains on the feasibility of such a mission: how realistic is a dedicated, purely space-based microlensing survey? We shall now consider the results of a previous such example by an unlikely protagonist, the Kepler Space Telescope (KEPLER), famous for its hoard of exoplanets detected via the transit method. The fact that a space-based observatory not optimised for microlensing science, running on faulty reaction wheels, has been used for a dedicated microlensing mission is surprising and its results shall be discussed in chapter 4.

Chapter 4

Exoplanets From Kepler K2 Campaign 9

From the 22nd April until the 2nd July 2016, during the KEPLER K2 science mission, the telescope performed a two part microlensing survey of the Galactic Bar (Henderson et al., 2016), the 9th campaign of the K2 mission (K2C9). This particular survey covered a 3.9deg^2 region, with its superstamp shown in figure 4.1, the results of which were analysed by McDonald et al. (2021) in the work *Kepler K2 Campaign 9 - I. Candidate short-duration events from the first space-based survey for planetary microlensing*, of which the writer is a coauthor. The primary aim of this study was to search for FFP candidates, with the initial work done by Ian McDonald involving passing the 3,752,652 lightcurves found by K2C9 through a rigorous filtering pipeline to remove transient events caused by phenomena such as cosmic rays and asteroids, as well as removing lightcurves with a low signal-to-noise. From the initial sample of lightcurves extracted from the survey, 8,808 short timescale microlensing events satisfying $u_0 < 5$ and $0.06 < t_\mathrm{E} < 10$ days were found (assuming a PSPL model). After a thorough filtering process, five events were found which had not been previously detected in other microlensing surveys, with nine events having already been discovered by OGLE and a further 13 having been discovered previously by KMTNet. One of the five novel events exhibited a binary caustic crossing anomaly, indicating a potential bound object rather than an FFP, which we shall discuss shortly. Another event, also discovered by KMTNet, exhibited a lightcurve better described by a cataclysmic variable. This left a total of 25 short timescale FFP candidate events detected by K2C9.

One factor complicating the analysis of K2C9 photometry, is a problem inherent to any survey done during KEPLER's K2 mission. This is the increased residual angular momentum of KEPLER caused by the failure of half of its reaction control wheels. Under K2 conditions, the telescope maintains its roll orientation using differential photon pressure from the Sun on its solar panels; however due to the continued degradation of its reaction wheels, maintaining a constant pointing direction remains difficult and the consequences of this are borne on the quality of the collected photometry, manifesting as periodic flux variations on top of the variation induced by the microlensing event's magnification.

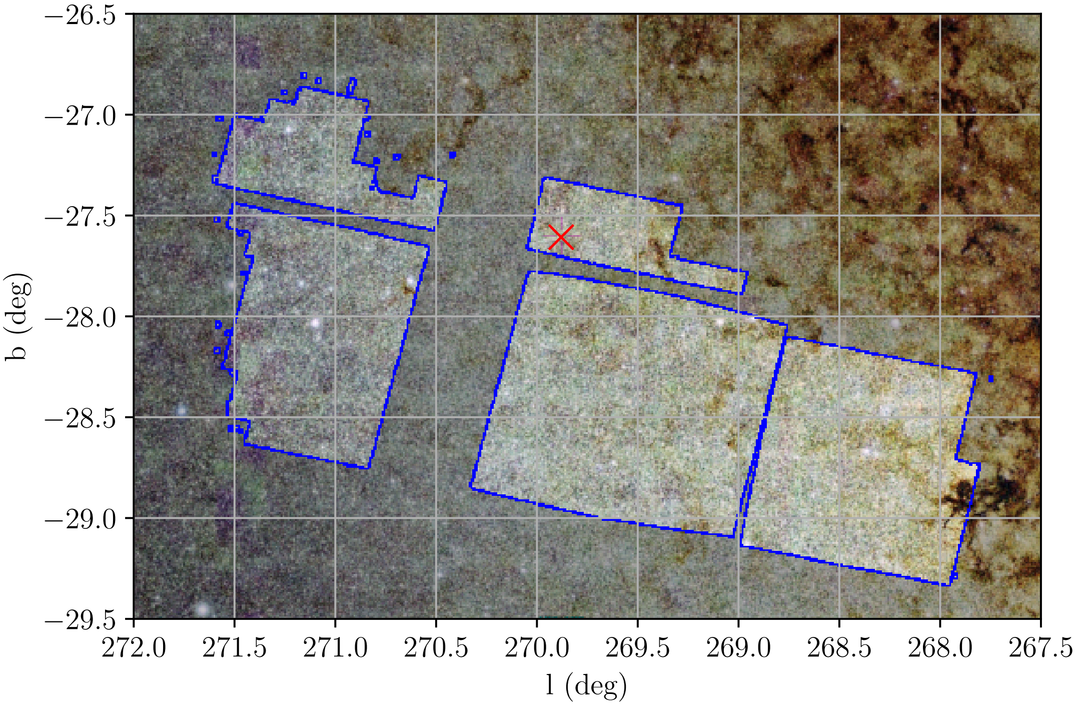
−26.5
−27.0
−27.5
−28.0
−28.5
−29.0
−29.5
b (deg)
272.0
271.5
271.0
270.5
270.0
269.5
269.0
268.5
268.0
267.5
l (deg)

FIGURE 4.1: Shown is the K2C9 superstamp inside which the survey's events were found, superimposed over a 2MASS image of the Galactic center aligned in equatorial coordinates, extracted using the *Aladin* tool (Bonnarel et al., 2000). The boundary of the superstamp is outlined in blue, with the exterior darkened for contrast. The location of K2-2016-BLG-0005, a planetary binary event found solely by KEPLER, is marked with a red cross for reference.

A second difficulty of analysing candidate microlensing events using KEPLER is the angular size of the detector pixels, which for KEPLER is 3.98″, compared to OGLE's Las Campanas Observatory with 0.26″ per pixel or the KMTNet observatories at 0.4″ per pixel, a salient contrast highlighting KEPLER's lack of optimisation for microlensing surveys. A consequence of these comparatively large pixel sizes is the introduction of significant levels of blending from other source stars under the target pixel. This means it is often not possible to fit a standard PSPL model to extract $t_{\rm E}$ in an attempt to characterise timescale distribution of the event sample as a proxy for the FFP mass distribution. A degeneracy between u_0 and $t_{\rm E}$ appears and events are typically only detected when $u_0 \ll 1$ in order for the event peak to appear above the photon noise generated by the blending flux. To characterise such events, we must instead use a degenerate model, using the parameters

$$t_{\rm eff} = u_0 t_{\rm E}, \tag{4.1}$$

$$F' = \frac{F_0}{u_0}, \tag{4.2}$$

where $t_{\rm eff}$ is the effective timescale, F_0 the un-magnified base flux and F' the effective base flux. The observed flux, in the limit of $u_0 \to 0$ is thus given by

$$F(t) = \frac{F'}{\sqrt{1 + \frac{(t-t_0)^2}{t_{\rm eff}^2}}}. \tag{4.3}$$

Using this degenerate PSPL model, the $t_{\rm eff}$, t_0 and F' were fit by the writer to 21 of the 26 FFP candidate lightcurves from K2C9. For the events found by both KMTNet and OGLE, the lightcurves and corresponding degenerate models are shown in figures 4.2 and 4.3 respectively, with best fit model parameters for all 25 candidates recorded in table 4.1, with the remaining lightcurve likely caused by a cataclysmic variable and hence excluded from this analysis.

The significance of these results becomes more apparent when modelling the distribution of $t_{\rm eff}$ using MaBμlS-2 and the Besançon Galactic model. Much like modelling a comparison with the OGLE-IV survey in chapter 2 and the FFP analysis using the EUCLID and ROMAN survey characteristics in chapter 3, another bespoke simulation was used to model the expected $t_{\rm eff}$ distribution of K2C9. Using values from Koch et al. (2004) which predict a photometric precision of 14ppm after a 6.5 hour exposure of a 12th magnitude star, this yields a flux count of $2.1 \times 10^5 e^- s^{-1}$ (Van Cleve & Caldwell, 2016) and zero-point magnitude of $m_{\rm zp} \sim 25.3$. Using an exposure time of $t_{\rm exp} = 1620$s (Penny et al., 2017), a signal-to-noise at event peak of $S/N > 50$ was mandated. A more involved time integrated signal-to-noise criterion was decided against, primarily due to the fact that inaccuracies between the simulation and empirical data are driven by the lack of detection efficiency calculations, which are more complex and go beyond the scope of this work, hence the more simplified event selection adopted by Specht et al. (2020) for use by the

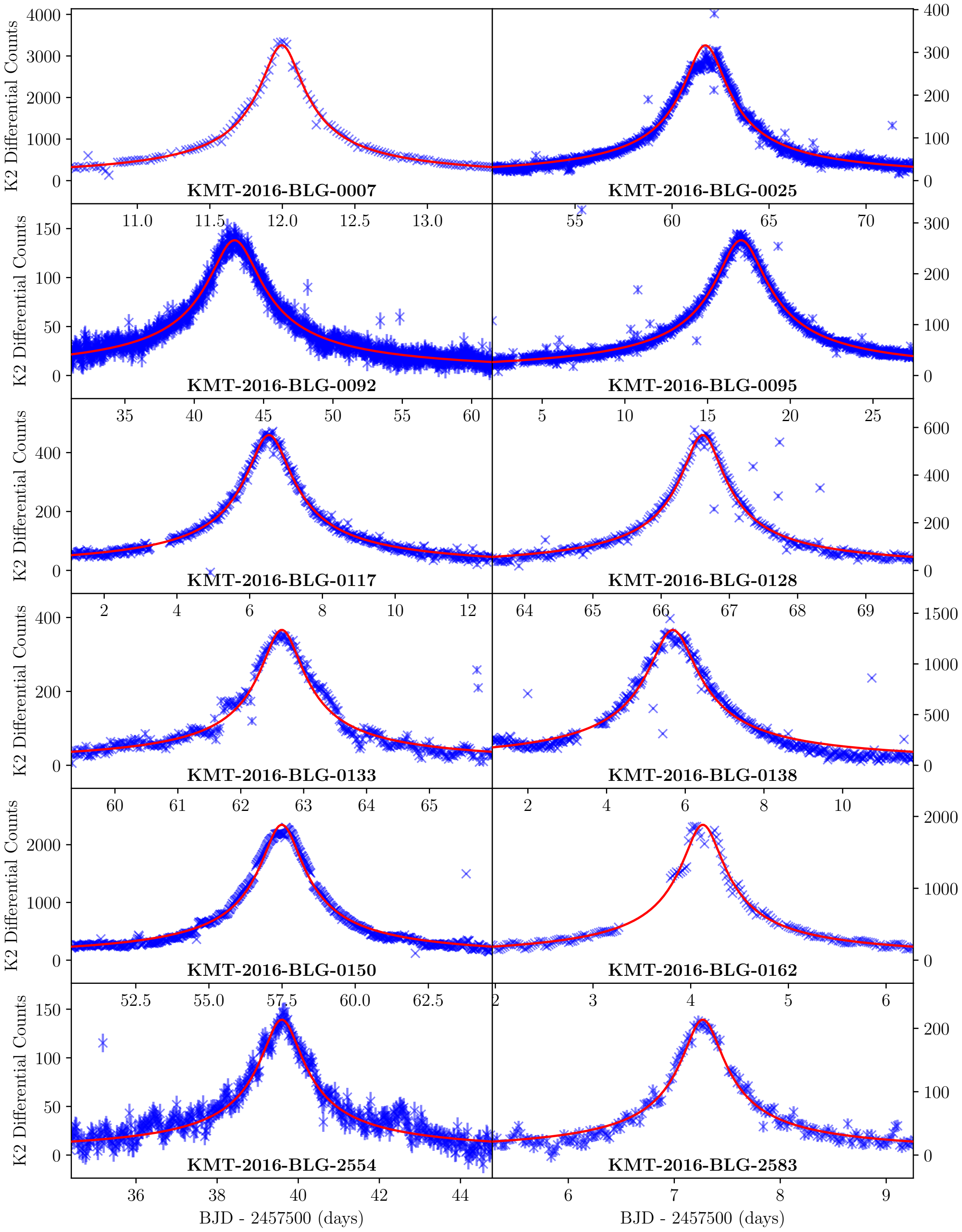

FIGURE 4.2: The K2C9 photometry for the 12 FFP candidate events which were also found by KMTNet are shown in blue with associated errorbars, along with the degenerate model from equation 4.3 overlayed in a solid red line. The particular KMTNet event name is shown at the bottom of each plot.

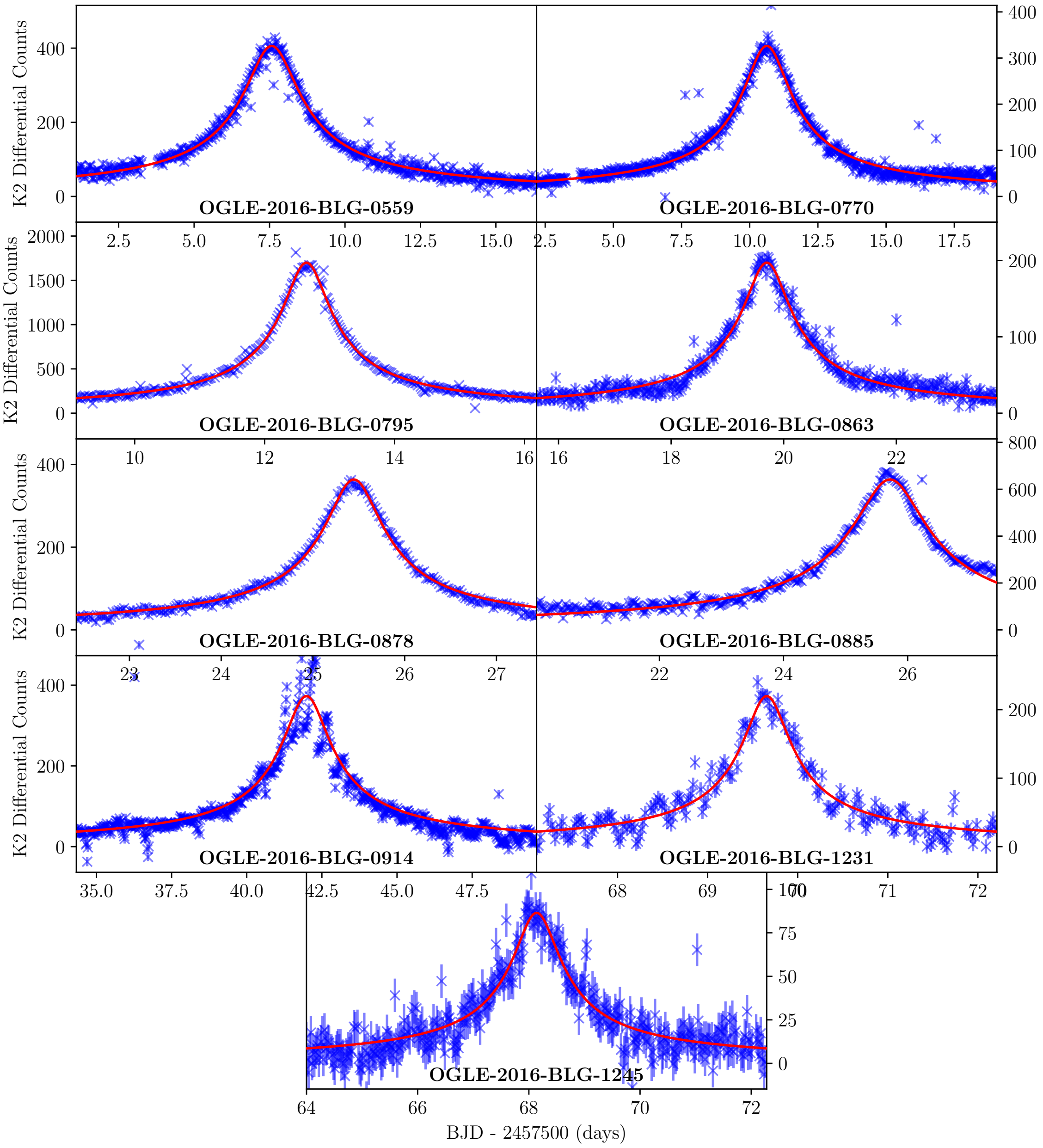

FIGURE 4.3: Same as figure 4.2, but for the nine events found by OGLE. The effect of KEPLER's deteriorating pointing stability is evident in photometry for OGLE-2016-BLG-0914, where the recorded flux fluctuates wildly as the source star passes over the varying response profile of a pixel.

Event Name	t_{eff} (days)	t_0 (BJD - 2450000)	F' (counts)
K2C9-2016-BLG-0001	$0.0535^{+0.0037}_{-0.0034}$	$7511.4562^{+0.0040}_{-0.0041}$	$119.5^{+4.8}_{-4.7}$
-0002	$0.0168^{+0.0009}_{-0.0008}$	$7544.5050^{+0.0009}_{-0.0009}$	$313.5^{+10.0}_{-9.6}$
-0003	$0.0616^{+0.0083}_{-0.0072}$	$7522.9878^{+0.0059}_{-0.0061}$	$75.0^{+5.5}_{-5.2}$
-0004	$0.0360^{+0.0042}_{-0.0037}$	$7558.0645^{+0.0036}_{-0.0035}$	$109.3^{+7.3}_{-7.0}$
OGLE-2016-BLG-0559	$0.8778^{+0.0055}_{-0.0051}$	$7507.5719^{+0.0050}_{-0.0051}$	$406.1^{+1.5}_{-1.5}$
-0770	$0.8439^{+0.0066}_{-0.0065}$	$7510.6247^{+0.0065}_{-0.0064}$	$326.5^{+1.5}_{-1.5}$
-0795	$0.3542^{+0.0010}_{-0.0010}$	$7512.6433^{+0.0010}_{-0.0010}$	$1700.9^{+2.9}_{-2.9}$
-0863	$0.4088^{+0.0064}_{-0.0063}$	$7519.6990^{+0.0065}_{-0.0065}$	$197.3^{+1.8}_{-1.8}$
-0878	$0.3025^{+0.0033}_{-0.0032}$	$7525.4461^{+0.0032}_{-0.0033}$	$363.6^{+2.3}_{-2.3}$
-0885	$0.5693^{+0.0034}_{-0.0035}$	$7525.7154^{+0.0030}_{-0.0030}$	$641.8^{+2.2}_{-2.2}$
-0914	$0.7657^{+0.0061}_{-0.0061}$	$7541.9867^{+0.0060}_{-0.0060}$	$373.1^{+1.8}_{-1.8}$
-1231	$0.2555^{+0.0056}_{-0.0055}$	$7569.6563^{+0.0061}_{-0.0061}$	$220.0^{+2.9}_{-2.9}$
-1245	$0.4140^{+0.0177}_{-0.0165}$	$7568.1393^{+0.0166}_{-0.0170}$	$86.5^{+2.2}_{-2.1}$
KMT-2016-BLG-0007	$0.1451^{+0.0002}_{-0.0002}$	$7511.9962^{+0.0002}_{-0.0002}$	$3259.4^{+3.4}_{-3.4}$
-0025	$1.0980^{+0.0067}_{-0.0068}$	$7561.7135^{+0.0069}_{-0.0067}$	$316.7^{+1.2}_{-1.1}$
-0092	$1.8584^{+0.0209}_{-0.0215}$	$7542.9063^{+0.0203}_{-0.0215}$	$138.1^{+0.9}_{-0.9}$
-0095	$1.5041^{+0.0096}_{-0.0096}$	$7517.0269^{+0.0091}_{-0.0092}$	$266.1^{+1.0}_{-1.0}$
-0117	$0.6150^{+0.0038}_{-0.0037}$	$7506.5315^{+0.0036}_{-0.0038}$	$459.8^{+1.6}_{-1.6}$
-0128	$0.3085^{+0.0022}_{-0.0021}$	$7566.6109^{+0.0022}_{-0.0022}$	$568.5^{+2.4}_{-2.4}$
-0133	$0.3346^{+0.0035}_{-0.0035}$	$7562.6527^{+0.0039}_{-0.0039}$	$366.6^{+2.4}_{-2.3}$
-0138	$0.6113^{+0.0016}_{-0.0016}$	$7505.6835^{+0.0017}_{-0.0017}$	$1335.2^{+2.0}_{-2.1}$
-0150	$0.7195^{+0.0011}_{-0.0011}$	$7557.4914^{+0.0012}_{-0.0012}$	$2346.0^{+2.2}_{-2.2}$
-0162	$0.2155^{+0.0007}_{-0.0007}$	$7504.1241^{+0.0006}_{-0.0006}$	$1884.7^{+3.6}_{-3.5}$
-2554	$0.5190^{+0.0115}_{-0.0109}$	$7539.5950^{+0.0121}_{-0.0120}$	$139.3^{+1.0}_{-1.0}$
-2583	$0.1986^{+0.0043}_{-0.0043}$	$7507.2694^{+0.0048}_{-0.0048}$	$213.8^{+2.8}_{-2.7}$

TABLE 4.1: The best fit parameters for the K2C9 FFP candidate events found by the pipeline described in McDonald et al. (2021), using the flux model from equation 4.3. Events are sequestered by survey, with K2C9 events at the top, OGLE in the middle and KMT at the bottom.

general tool.

The K2C9 campaign was simulated over a region approximating the survey's superstamp near the Galactic bar for three different models: a purely stellar and Brown dwarf mass population and the Mróz and Sumi FFP population models examined in chapter 3. For each model, two scenarios were investigated, namely a short timescale simulation using the constraint $0.06 < t_{\mathrm{E}} < 10$ days and another with unbound t_{E}. In all scenarios, the threshold maximum impact parameter u_t was set to one. To simulate a t_{eff} value, a u_0 value was uniformly sampled in the range $0 \rightarrow 1$ for each valid lens-source pair. The output of these simulations came in the form of a relative event rate as a function of t_{eff}, with the peak event rate for the unbound models normalised to unity. The results of these simulations are shown in figure 4.4, overlayed with the fitted t_{eff} of the novel K2C9, KMTNet and OGLE-IV short timescale events.

As expected, all short timescale simulations terminate at 10 days, with a maximum rate of $t_{\mathrm{eff}} \simeq 10 \times \langle u_0 \rangle = 5$ days, consistent with a mean $u_0 = 0.5$ due to uniform sampling, while the t_{eff} distribution of unconstrained models continues further to the right of the figure. The FFP models are shown superimposed on top of the regular stellar mass models to illustrate their contributions to the total event rate. Although without a proper measurement of t_{E} and by extension M_{L}, it is not possible to characterise the mass distribution of K2C9 short timescale events, they are nonetheless consistent with the relative predicted rates of the Mróz model for the novel K2C9 events and the Jupiter mass Sumi model for jointly detected OGLE- and KMTNet-K2C9 events. To extend this work, a more rigorous analysis taking into account the detection efficiency of FFPs that closely models the pipeline employed by McDonald et al. (2021) will be required to more thoroughly vet the 22 events.

4.1 K2-2016-BLG-0005

Now that we have examined the work done to search for FFP candidates using KEPLER, we shall now return to the remaining event discovered in the K2C9 data which showed evidence of lens binarity: K2-2016-BLG-0005, which was studied in a follow up paper, *Kepler K2 Campaign 9: II. First space-based discovery of an exoplanet using microlensing* (Specht et al., 2022). This event showed a well sampled caustic crossing anomaly on top of an underlying PSPL curve during the first subcampaign of K2C9, the analysis of which involved a complicated fitting process. Its location is indicated in figure 4.1 with a red cross, at RA = 17h59m31.16s, Dec = $-27°36'26.90''$.

The 30 minute observing cadence of K2C9 resulted in a total of 1,150 data points sampled over the duration of the K2-2016-BLG-0005 event, shown in figure 4.5. The caustic crossing event begins around $t = BJD - 2450000 = 7515$ days and ends shortly after $t = 7519$ days, with the caustic entry reaching a lower peak magnification than the exit; a subtle but salient fact when fitting a binary model, due to the magnification map structure of the differing caustic topologies. Over this time period, KEPLER gathered 180 data points.

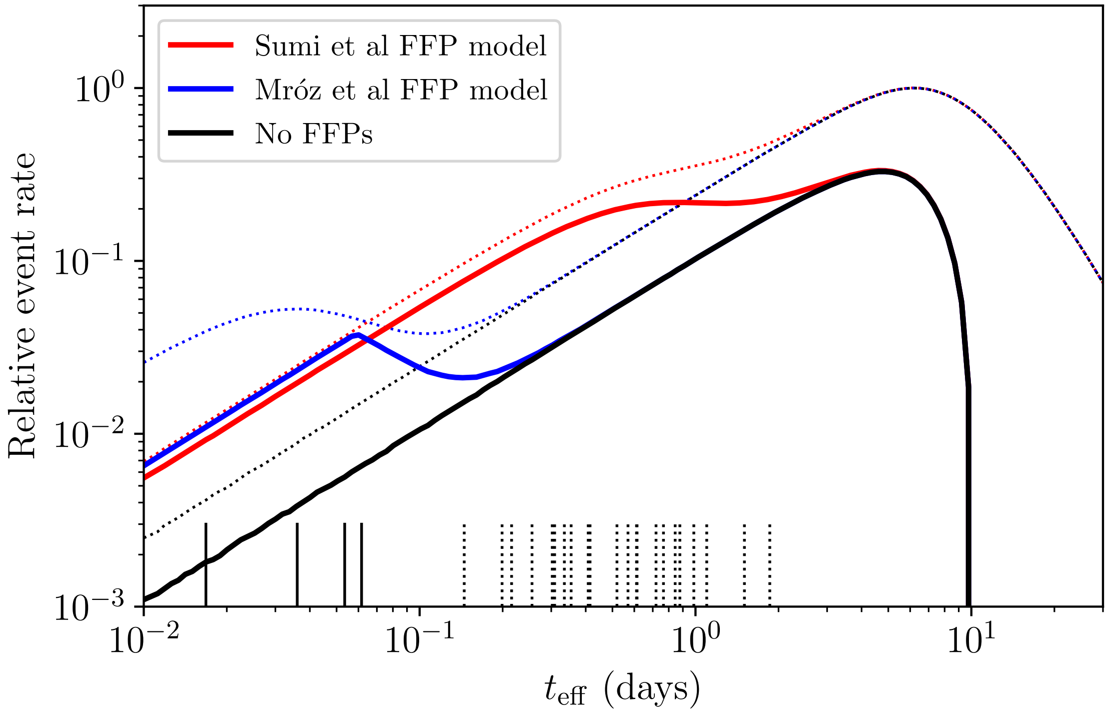

FIGURE 4.4: The relative event rates of various models are shown, assuming K2 survey optics and $u_{\rm t} = 1$. The solid lines show the event rates for events with $0.06 < t_{\rm E} < 10$days, while the dotted lines show the equivalent for the full distributions. At the bottom of the figure, four vertical lines representing all candidate FFP events from K2C9 not previously discovered by other surveys mark their effective timescales, while the dotted vertical lines represent the 22 $t_{\rm eff}$ of events found previously by OGLE and KMTNet.

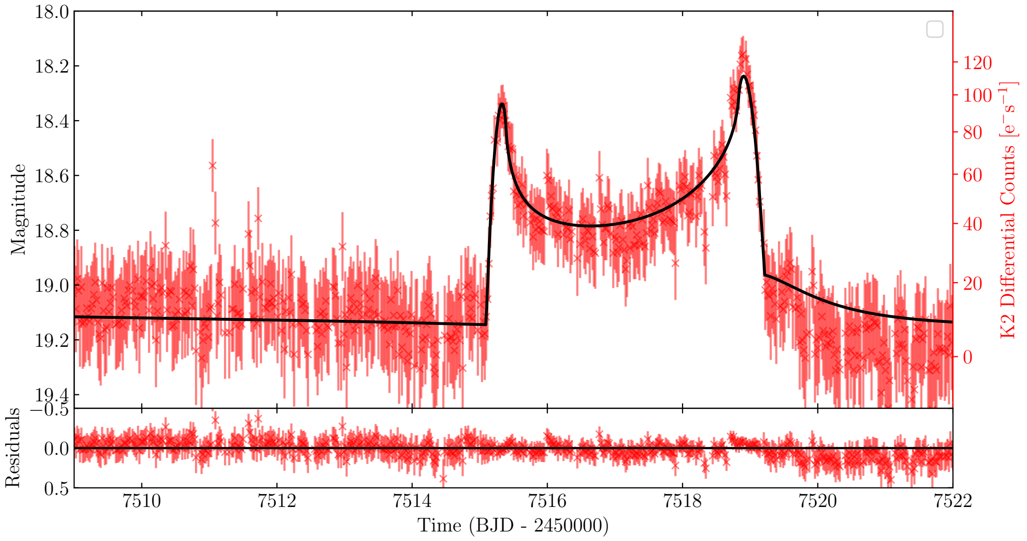

FIGURE 4.5: The K2C9 photometry gathered for the K2-2016-BLG-0005 event, with associated errorbars, is shown on top of the best fit binary model (black solid line). Time is recorded in terms of Barycentric Julian Date (BJD), which represents a small correction on the Julian date by accounting for the Earth's motion about the Earth-Sun barycentre. On the bottom are shown the residuals of the data relative to the model. The K2 flux scale is shown on the right, which has a complicated non-linear, non-logarithmic scaling which terminates at a magnitude of $m = 19.3$.

Although the high cadence of K2C9 aids in the characterisation of the binary model and the evaluation of ρ, which is essential for obtaining a lens mass measurement, a parallax signature is still required. To this end, photometry from five ground-based surveys of K2-2016-BLG-0005 was obtained, allowing for a space-based measurement of the microlensing parallax $\pi_{\rm E}$. The surveys contributing to the ground-based photometry were OGLE (Udalski et al., 2015), KMTNet (Kim et al., 2016), MOA (Bond et al., 2001), CFHT (the Canada-France-Hawaii Telescope, Zang et al. (2018)) and UKIRT (the United Kingdom Infrared Telescope, Shvartzvald et al. (2017)). The superposition of all ground-based datasets is shown in figure 4.6, where it is clear that the binary model is different due to the space-based parallax effect. The caustic crossing is shorter, with a duration of $\sim$ 2 days and a notable cusp approach around $t = 7512.5$ days lasting a day. The cusp approach is well sampled by KMTNet, while the caustic crossing itself is more sparse. Both features of the anomaly span a different time range from the KEPLER dataset, over 7511 days $< t <$ 7518 days. As all ground-based photometry was extracted using a difference image analysis (Alard, 2000), the photometric error was underestimated. This was corrected for by using techniques discussed in Skowron et al. (2016) for the OGLE-IV dataset and Yee et al. (2012) for all other datasets.

Data from OGLE was collected during the OGLE-IV survey in the Johnson-Cousins I band filter and spanned $7425 < t < 7692$, with a total of 1642 data points and median uncertainty of 0.116 magnitudes. OGLE's Las Campanas Observatory has a $1.3m$ diameter mirror and a field of view of 1.4deg^2. Over the anomaly timespan for the ground model,

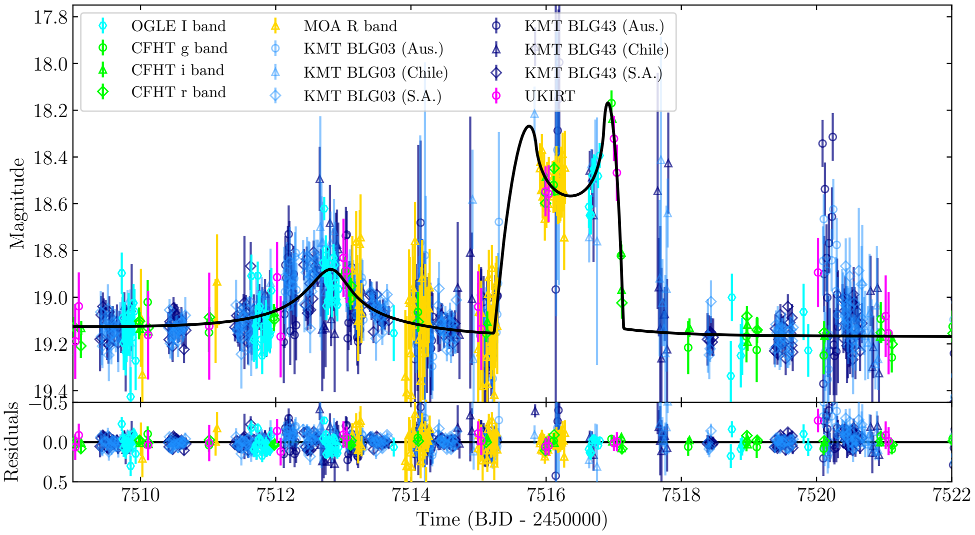

FIGURE 4.6: Same as figure 4.5, but for the ground photometry. In black is shown the ground-based binary model, which is markedly different due to the large baseline between KEPLER and the Earth. This difference allows for a more precise measurement of the microlensing parallax, given the short timescale features of the binary caustic crossing. Note the shorter width of the caustic crossing, as well as the secondary peak to the left around $t = 7512.5$ days, which represents a caustic cusp approach of the source; another important marker when constraining the binary model with parallax.

OGLE produced 45 datapoints.

The CFHT telescope was used in tandem with KEPLER from the onset of the K2C9 survey to provide supplementary data that could assist in a space-based parallax measurement. Photometry came from three different filters, namely the CFHT g, r and i bands. The telescope, situated atop Mauna Kea in Hawaii, has a $3.58m$ diameter mirror, a field of view of 0.94deg^2 and resolution of 0.187″ per pixel. CFHT gathered 183 data points across each of the three filters used, with 29 epochs within the binary anomaly timespan.

The contribution from the KMTNet microlensing survey came from three separate telescopes in the Southern hemisphere, one each in Australia, Chile and South Africa (Kim et al., 2018b). In addition to each observatory, data for K2-2016-BLG-0005 was distributed over two KMT fields, KMT-BLG-03 and KMT-BLG-43. This gave a total of six contributions from KMTNet to the ground-based lightcurve, totalling 4,634 datapoints with 369 epochs within the anomaly timespan. Each telescope in the KMT Network has a $1.6m$ diameter mirror, a field of view of 4deg^2 and angular resolution of 0.4″ per pixel. Observations are made in the Johnson-Cousins I band filter.

For the MOA contribution, 3703 data points were collected, with 84 epochs inside the anomaly timespan. The Mt. John Observatory uses a $1.8m$ telescope, covering a 2.2deg^2 field of view at a resolution of 0.58″ per pixel. The filter used is the MOA_R band.

The final photometry contribution to the ground-based data comes from UKIRT. Like CFHT, the UKIRT telescope is located on Mauna Kea, and features the largest mirror used

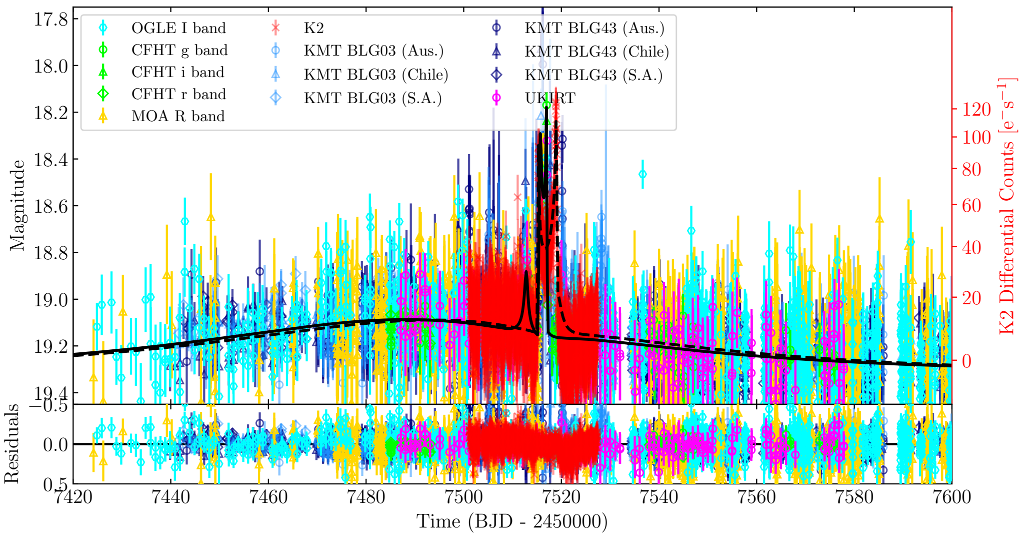

FIGURE 4.7: The K2-2016-BLG-0005 event is shown in its entirety, including the larger PSPL trend from the primary lens, with all photometry contributions from both ground-based observatories and KEPLER. The best fit ground-based model is shown as a solid black line, with the satellite model in a dashed black line. It is evident on this scale how powerful a caustic crossing can be in its contribution to a microlensing event, given the large magnification of the anomaly relative the peak of the underlying PSPL curve.

for data collection of K2-2016-BLG-0005 at 3.8m. It also has the smallest field of view, at 0.19deg^2 and a resolution of 0.4″ per pixel. A total of 139 measurements were taken over the duration of the event in the near-infrared Johnson-Cousins H band, with 11 epochs inside the anomaly timeframe. The super position of all photometry used in this analysis is shown across

4.2 The binary parameterisation

Given the small width of the caustic crossing, on the order of a few days, compared to the timescale t_E of the underlying PSPL event, the fitting process was performed using an alternative "planetary" parameterisation of the binary model, akin to the "*Caustic Region of INfluence*" (CROIN) parameterisation used by Penny (2014), which recasts the familiar s, q and α into a new set of parameters, namely the minimum impact parameter to the planetary caustic normalised to the planetary Einstein radius $u_{0,\mathrm{pl}}$, the time of closest approach of the source to the centre of the planetary caustic, $t_{0,\mathrm{pl}}$ and the planetary Einstein radius crossing time $t_{\mathrm{E,pl}}$. This casting of the binary parameterisation in terms of proximity to the planetary caustic results in a faster fitting process when the secondary (planetary) lens is small compared to the primary (host star), giving finer control over trajectory of the source. This also allows for a much more straight forward choice of initial binary parameters, with the value of $t_{0,\mathrm{pl}}$ chosen to be centred, by visual inspection, on the caustic crossing anomaly in the lightcurve, $t_{\mathrm{E,pl}}$ chosen to be the width of the caustic

TABLE 4.2: Details on the ground-based telescopes used in the analysis of K2-2016-BLG-0005. The median error in magnitudes is also included.

Telescope/Field	Diameter (m)	Camera FOV (deg^2)	Pixel scale (arcsec/pix)	Filter	No. epochs (7511-7518)	Median Error
CFHT Maunakea	3.58	0.94	0.187	g	9	0.274
				i	10	0.113
				r	10	0.162
KMT Aus./BLG03	1.6	4.0	0.40	I	78	0.210
KMT Aus./BLG43				I	81	0.174
KMT Chile/BLG03	1.6	4.0	0.40	I	40	0.216
KMT Chile/BLG43				I	40	0.196
KMT S.Africa/BLG03	1.6	4.0	0.40	I	72	0.195
KMT S.Africa/BLG43				I	58	0.178
MOA Mt. John	1.8	2.2	0.58	MOA_R	84	0.528
OGLE Las Campanas	1.3	1.4	0.26	I	45	0.116
UKIRT Maunakea	3.8	0.19	0.40	H	11	0.247

anomaly and $u_{0,\mathrm{pl}}$ simply set to zero to force the binary model to pass directly over the planetary caustic.

Although this parameterisation is useful for the fitting process, it was still necessary to convert back to the standard s, q and α formalism (as defined in section 1.7) at runtime due to incompatibilities with the code used and also for presenting results due to the familiarity of the scientific community with the standard formalism. The conversion is also dependent on the topology used (either close or wide), as the wide topology only features a single planetary caustic co-linear with the binary axis, while the close model features two off-axis caustics, with both caustics requiring a different, more complex conversion. Regardless of the topology chosen, some parameters are used throughout:

$$\gamma = \frac{t_{\mathrm{E,pl}}}{t_{\mathrm{E}}}, \tag{4.4}$$

$$v = u_0 + \gamma u_{0,\mathrm{pl}}, \tag{4.5}$$

$$\tau = \frac{t_{0,\mathrm{pl}} - t_0}{t_{\mathrm{E}}}, \tag{4.6}$$

$$u' = \sqrt{v^2 + \tau^2}, \tag{4.7}$$

$$q = \gamma^2 \tag{4.8}$$

For the wide model, the conversions for s and α are given by

$$s = \frac{1}{2}\left(u' + \sqrt{u'^2 + 4}\right), \tag{4.9}$$

$$\alpha = 360^\circ - \frac{180^\circ}{\pi} \times \arcsin\left(\frac{v}{u'}\right). \tag{4.10}$$

The first close solution, where the trajectory of the source takes it over the lower planetary caustic, requires more parameters to be defined,

$$\delta = u'^2 + 2 + 4(4\gamma^2 + 1)(u'^2 - 1), \tag{4.11}$$

$$\beta = \arctan\left(\frac{\tau}{u_0}\right), \tag{4.12}$$

$$s = \sqrt{-\frac{u'^2 + 2\sqrt{\delta}}{2(u'^2 - 1)}}, \tag{4.13}$$

$$\eta = \frac{2\gamma}{s\sqrt{1+s^2}}, \tag{4.14}$$

$$\theta = \arctan\left(\frac{s\eta}{1-s^2}\right), \tag{4.15}$$

$$\alpha = 90^\circ + \frac{180^\circ}{\pi} \times (\theta + \beta). \tag{4.16}$$

The final conversion was required for the second close topology model, where the source trajectory takes it across the upper planetary caustic, but also approaches the lower planetary caustic from the right, albeit typically too far to produce a notable cusp approach. A few more parameters were defined for this final conversion, which also involved updating the parameter u_0 to a new value given by $u_{0,\mathrm{new}}$, via

$$\nu = \frac{16q}{\tau^2 + (u_{0,\mathrm{pl}} - u_0)^2}, \tag{4.17}$$

$$s = \sqrt{\frac{\sqrt{4\nu+1} - 1}{2}}, \tag{4.18}$$

$$\alpha = 90^\circ - \frac{180^\circ}{\pi} \times \arctan\left(\frac{u_{0,\mathrm{pl}} - u_0}{\tau}\right), \tag{4.19}$$

$$u_{0,\mathrm{new}} = \left(s + \frac{1}{s} - \frac{\eta}{\tan(\pi - \alpha_{\mathrm{rad}})}\right) \sin(\pi - \alpha_{\mathrm{rad}}) - u_{0,\mathrm{pl}}, \tag{4.20}$$

where $\alpha_{\mathrm{rad}} = \frac{180^\circ}{\pi} \times \alpha$ is simply the source trajectory angle relative to the binary axis, converted from degrees into radians. Throughout this chapter, parameters from both binary parameterisations will be used depending on the context.

4.3 The fitting process

Numerous tools were used to fit the binary microlensing model to the event's photometry. The process of iteratively refining the model was performed by `MulensModel`, a tool used to simulate and fit data to microlensing events (Poleski & Yee, 2019). `MulensModel` itself uses the `VBBinaryLensing` (VBBL) code to evaluate the magnification of a binary lens with finite source effects (Bozza et al., 2018); a contour integration method relying on Green's theorem (Bozza, 2010) to evaluate the boundaries of the multiple images of the source produced by binary lensing. The calculation of the source boundaries relies on an efficient root finding algorithm by Skowron & Gould (2012). From the boundaries of each image, VBBL provides an accurate estimation of the magnification, which in this context is the ratio of the cumulative area of each image to that of a standard circular source. VBBL can also evaluate magnifications with a limb-darkening model, which was used in this analysis, although this significantly increased computation time and informed the precise fitting strategy as discussed in this section.

Acquiring the best fit binary microlensing model involved multiple stages. Each stage involving the `MulensModel` fitting process is characterised by a set of starting parameters with associated Gaussian distribution widths, along with the total number of iterations and random walkers used. For stages designed to acquire good initial guesses for later refinement, a setup with more random walkers with fewer iterations was used. The product of total iteration count and random walker count was contingent on the complexity of the model being fitted for at that particular stage, in order to produce results in an acceptable timeframe.

As the binary anomaly (the caustic crossing and cusp approach) only concerns a small part of the overall lightcurve, the first stage involved fitting a PSPL model to the ground-based data only, by omitting datapoints between 7511 days $< t <$ 7518 days. This provided the initial starting values for u_0, t_0 and t_{E}. This first stage used a total of 20 walkers and 10,000 steps, yielding first estimates of $t_0 = 2457487.61 \pm 0.03$ days, $u_0 = 0.58 \pm 0.01$ and $t_{\mathrm{E}} = 85.6 \pm 1.0$ days.

For stage two, the fitting process was quadfurcated to test four candidate binary models, each representing a possible degenerate solution to the observed data. Two of these models were of the wide caustic topology, with one assuming the regular setup of binary parameters and the other representing the ecliptic degenerate solution, outlined by Poindexter et al. (2005). This degeneracy is the result of the event lying close to the ecliptic plane at $\beta = -4.16°$, such that the parallax effect from Earth's acceleration lies predominantly in the East/West direction, resulting in a symmetry between solutions with relative proper motions reversed in the North/South directions. As such, this ecliptic degenerate wide model was seeded with the same starting parameters except for the transformations $u_0 \to -u_0$, $\alpha \to -\alpha$ and $\pi_{\mathrm{E,N}} \to -\pi_{\mathrm{E,N}}$.

For the close models, the predominant degeneracy was between the passage of the source over the two different secondary (planetary) caustics. Although fits of the close model produced solutions which obeyed $s < 1$, the mass ratio q often produced resonant solutions when the source was initially made to pass near the upper planetary caustic, as shown in figure 4.8, which shows the best fit caustic models for the standard wide solution and two close solutions.

The binary models provided the planetary parameters $t_{0,\mathrm{pl}}$, $t_{\mathrm{E,pl}}$ and $u_{0,\mathrm{pl}}$ for each of the four degenerate solutions, using starting values of BJD $= 2457516$ days, 2 days and 0 respectively, using the justification outlined in section 4.2. Finite source effects were also introduced at this stage, but via the parameter $t_* = t_{\mathrm{E}}\rho$, the source radius crossing time. Much like the planetary parameterisation, using t_* allows for a faster convergence to a best fit value as it helps to characterise the width of the caustic crossing peaks in the data. An initial guess of $t_* = 0.01$ days was used, assuming a typical value of $\rho = 10^{-4}$.

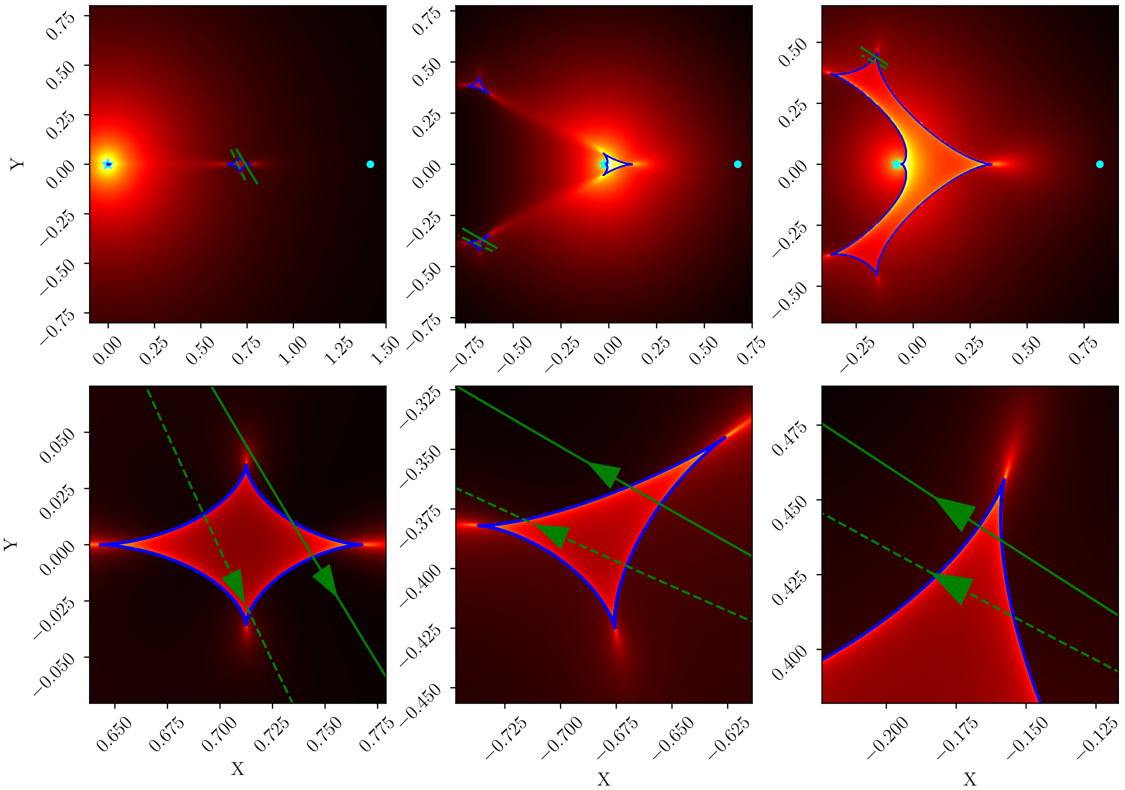

FIGURE 4.8: The magnification maps for the best fit standard wide solution (left column) and two close solutions (middle and right columns) are shown on a log-scale to compress the dynamic range for illustrative purposes. For the upper planetary caustic close solution, although the binary parameter s remained below unity, the mass ratio q rose high enough such that the planetary and primary caustics joined into a resonant topology (the conditions required for this were shown in figure 1.8). The caustics are shown above the magnification map in solid blue lines, with the ground model trajectory indicated with a solid green line and satellite trajectory indicated with a dashed green line. Arrow heads on the trajectories are included to illustrate the direction of motion of the source relative to the lens system. The primary lens is indicated with a cyan star at a location $X = -\frac{M_{\rm pl}}{M_{\rm pl}+M_*}$, while the secondary/planetary lens is indicated to the right with a cyan circle with the center of mass at $X = 0$. The bottom row shows a zoomed-in window of the top row, focusing on the caustic crossings.

This stage used the same number of walkers as the first stage of 20, but fewer steps of 4,000 due to the longer time required to numerically compute the finite source binary magnification compared to the simple analytical PSPL magnification.

The third stage is a brief detour from the optimisation of the microlensing model. To progress with the fitting process, the K2C9 photometry was required to fit a joint ground-satellite parallax model. To do this, the obstacles highlighted previously about the difficulties of extracting microlensing events from a K2 survey needed to be overcome. The modified causal pixel model (MCPM) (Poleski et al., 2019) specifically for dealing with these hurdles, was employed. It divides the flux measured by KEPLER into two components, namely a flux contribution from the source star and a flux contribution from instrumental phenomena. For the first contribution, MCPM used the wide ground-based model as an initial approximation to the time-dependent variation of the source flux. Both the microlensing model and data are jointly fit using `MulensModel` to evaluate the binary magnification and `EMCEE` (Foreman-Mackey et al., 2013), to perform the fit. The second contribution to the observed flux is induced by the varying pointing direction of KEPLER, which is determined by examining pixels nearby the target at the same epoch, using the causal pixel model method described in Wang et al. (2016). The extracted result represents the photometry of the magnified source signal in differential K2 flux counts, with associated errors, which could then be used in the next stage.

The introduction of parallax to the microlensing model adds two new parameters: $\pi_{\mathrm{E,E}}$ and $\pi_{\mathrm{E,N}}$, the parallax components in the Eastern and Northern directions, respectively, both initially set to zero as a starting condition for the fourth stage. This brought the total number of fitted microlensing parameters to nine, excluding the scaling and blending flux parameters for each dataset. This large number of parameters required a larger number of walkers at 100, required to explore the larger parameter space. In conjunction with the greater computational complexity of evaluating a finite source binary parallax model, the total number of steps was reduced to 500 due to the computation time required. This lower number of steps and higher number of random walkers allowed for a greater exploration of candidate global best fits, but with fewer steps, a less precise result with large non-Gaussian errors, mandating another fitting stage.

This fifth and final stage introduced limb darkening to the model, with the linear limb darkening parameters evaluated for each filter used in the analysis using data from Sing (2010). Although the limb darkening parameters were kept constant throughout the fitting stage, this once more had a significant impact on computation speed. Nevertheless, the number of walkers was reduced to 20 and the number of stages increased to 5,000 to produce the most accurate candidate solutions for each of the four models tested, taking approximately two days to complete for each model.

The fitted parameters for each tested model are shown in table 4.3, which shows the best performing solution is produced by the regular wide caustic model, using a metric of χ^2. Although the relative difference in χ^2 between the models is small, the main driver this difference is the caustic crossing anomaly which lasts only $\sim 1/30^{\mathrm{th}}$ the span of the ground-based data, and $\sim 1/6^{\mathrm{th}}$ the span of the full K2C9 photometry. The 2D distributions for the best 50% performing samples of the close, resonant and wide solutions in the binary lensing q, s parameter space are shown in figure 4.9. The ellipsoidal shape of the wide structure and the close proximity of the best fit to the ellipse's centroid help to confirm the validity of the wide model solution in contrast to the close and resonant solutions. Similarly, the 1D and 2D projections for each of the wide model parameters of the best 50% performing samples produced throughout the fit are shown in a corner plot separated across figures 4.10, 4.11 and 4.12. The Gaussian nature of these distributions demonstrates the success of the wide model at finding a local minimum in the parameter space, as well as showing correlations between the different parameters.

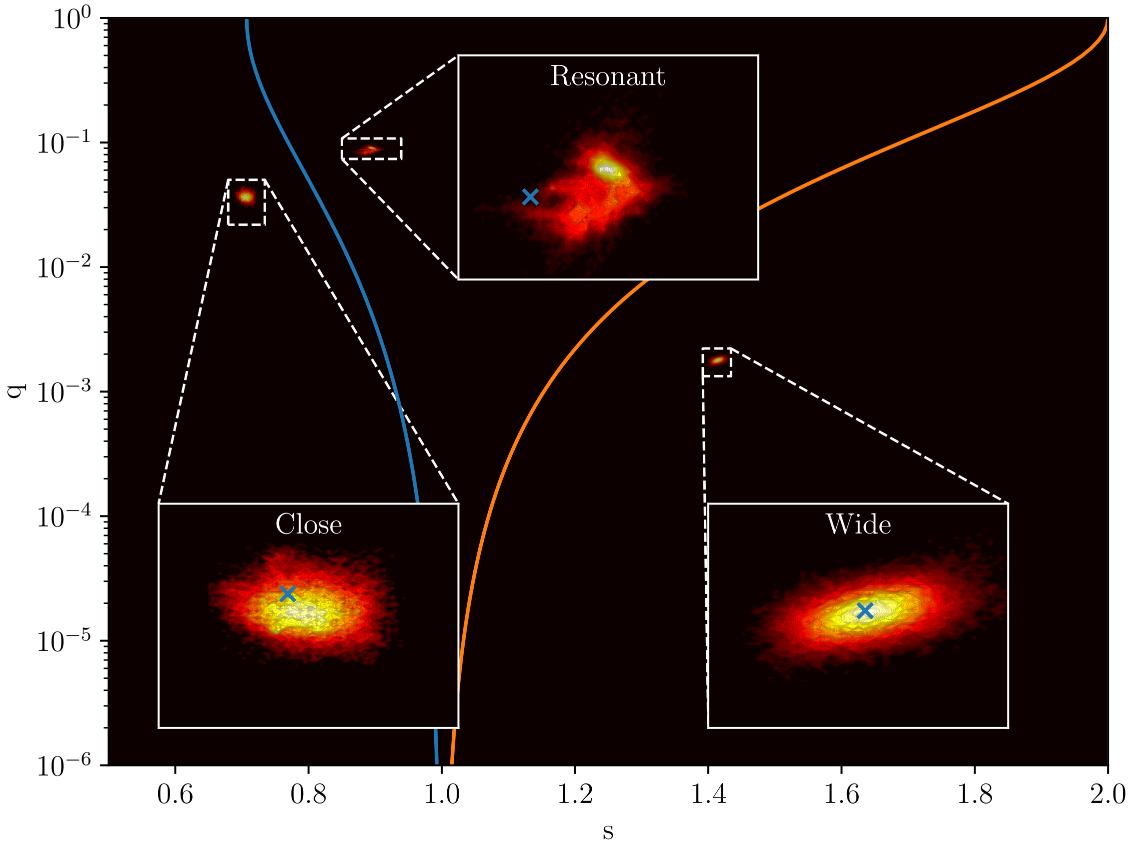

FIGURE 4.9: The distributions of the top 50% best performing samples extracted from the fitting process and plotted in an s, q parameter space are shown for the close, resonant and wide solutions. The blue line represents the close/resonant boundary, while the orange line represents the resonant/wide boundary, following from equations 1.34 and 1.35 from chapter 1. For each topology solution, a zoomed inset is shown with that topology's best solution indicated with a blue cross. The best performing model, the wide topology, exhibits a mostly symmetrical ellipse structure with the best solution aligning closely with that ellipse's centroid. The second best performing model, the close topology, features a more irregular shape with more pronounced noise present throughout the structure and a best solution offset from the structure's centroid. The worst performing solution, the resonant topology, exhibits a highly irregular structure with its main cluster of samples noticably offset from its best performing model.

Model	t_0 (days)	t_E (days)	t_* (days)	u_0	$t_{0,\text{pl}}$ (days)	$t_{E,\text{pl}}$ (days)	$u_{0,\text{pl}}$	$\pi_{E,E}$	$\pi_{E,N}$	χ^2
Wide	$7486.6^{+0.9}_{-0.9}$	$76.4^{+2.2}_{-2.1}$	$0.143^{+0.003}_{-0.003}$	$0.620^{+0.008}_{-0.008}$	$7515.41^{+0.02}_{-0.02}$	$3.24^{+0.03}_{-0.03}$	$-0.532^{+0.006}_{-0.006}$	$-0.045^{+0.002}_{-0.002}$	$-0.1103^{+0.003}_{-0.003}$	9839
Wide-Ecliptic	$7488.0^{+0.8}_{-0.9}$	$73.7^{+2.2}_{-1.9}$	$0.143^{+0.003}_{-0.004}$	$-0.639^{+0.008}_{-0.008}$	$7515.45^{+0.02}_{-0.02}$	$3.23^{+0.03}_{-0.03}$	$0.525^{+0.006}_{-0.006}$	$-0.076^{+0.003}_{-0.003}$	$0.090^{+0.002}_{-0.002}$	9860
Close	$7485.3^{+0.9}_{-0.6}$	$76.1^{+2.8}_{-2.4}$	$0.120^{+0.004}_{-0.004}$	$0.62^{+0.02}_{-0.02}$	$7514.2^{+0.1}_{-0.2}$	$15.0^{+0.6}_{-0.6}$	$0.09^{+0.06}_{-0.07}$	$0.015^{+0.005}_{-0.004}$	$0.100^{+0.003}_{-0.003}$	10532
Resonant	$7474.4^{+1.2}_{-1.1}$	$111.4^{+4.7}_{-2.6}$	$0.128^{+0.006}_{-0.010}$	$0.89^{+0.02}_{-0.03}$	$7522.3^{+3.4}_{-4.0}$	$32.7^{+1.0}_{-1.3}$	$-0.027^{+0.002}_{-0.001}$	$-0.035^{+0.002}_{-0.002}$	$0.060^{+0.001}_{-0.002}$	11147

TABLE 4.3: The fitted PSPL, binary, finite source and parallax model parameters are tabulated above for the best fit solutions of each of the four tested models. The χ^2 for each is shown in the final column.

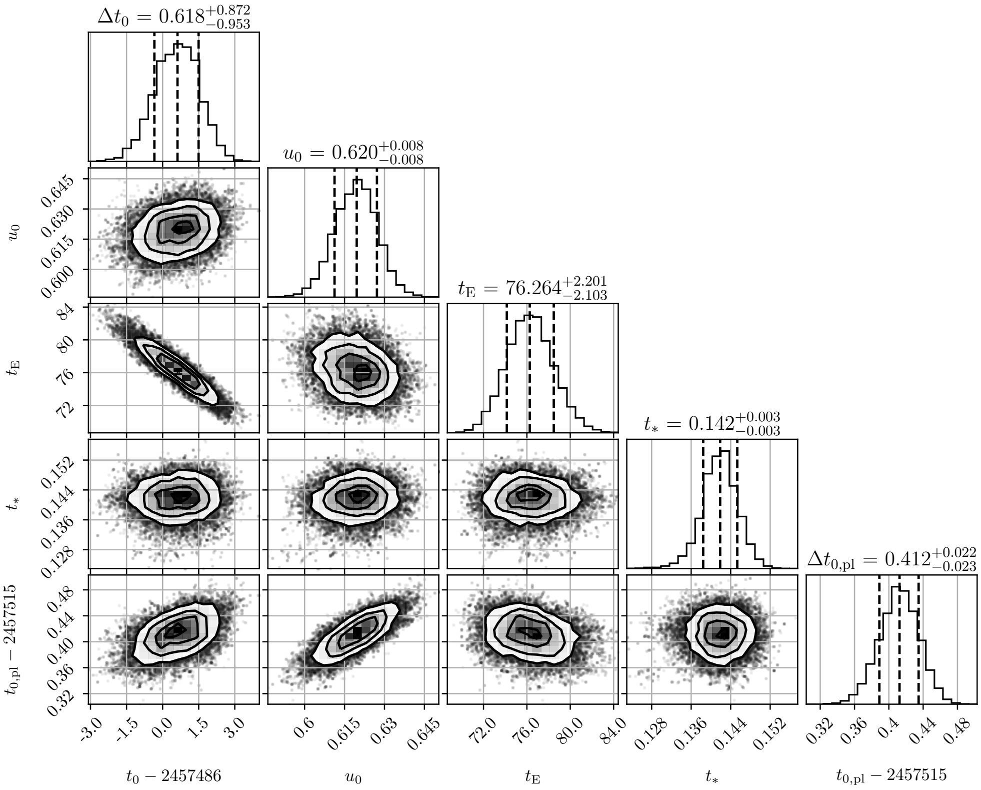

FIGURE 4.10: The corner plot displaying the distributions of the best 50% performing solutions from stage five for the standard wide caustic model, for the parameters t_0, u_0,t_E, t_* and $t_{0,pl}$ is shown. The median value of each parameter is shown above the 1D histograms along the diagonal, as well as the associated errors. We can see that the distribution of each parameter is approximately Gaussian, suggesting a healthy fit. The correlations between some parameters are also visible, such as between t_E and t_0, as the fitting algorithm attempts to constrain the location of the caustic crossing. Distributions of the remaining parameters are shown in figures 4.11 and 4.12. These corner plots were generated using code developed by Foreman-Mackey (2016).

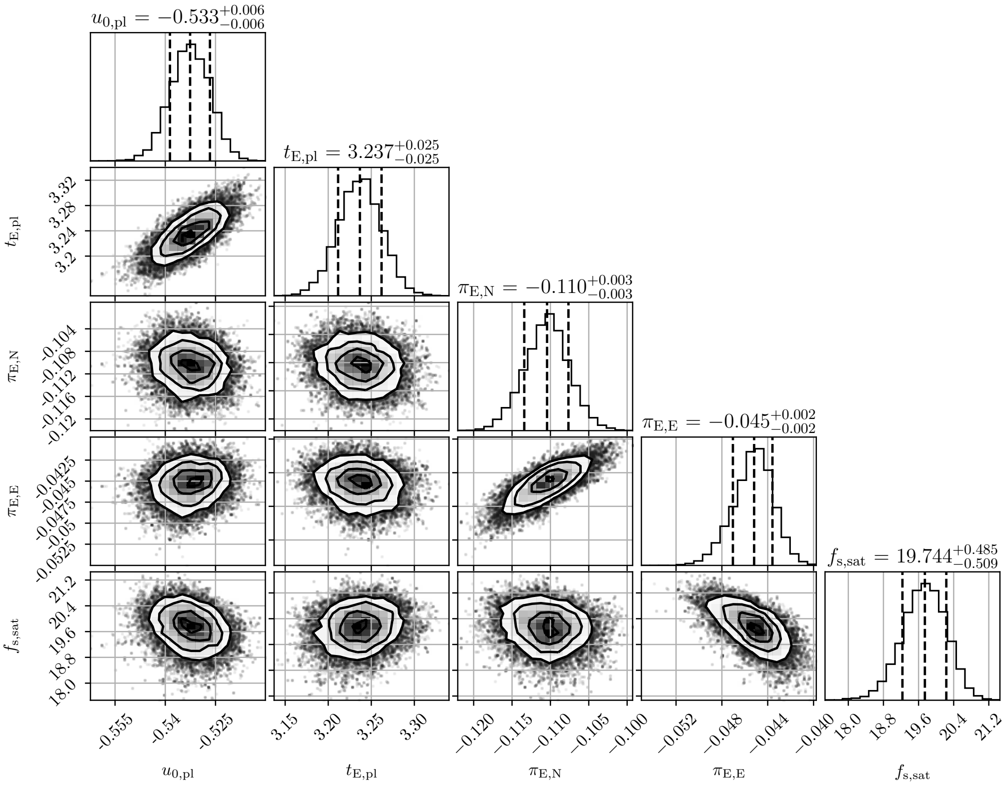

FIGURE 4.11: Shown above is the continuation of figure 4.10, for the parameters $u_{0,\mathrm{pl}}$, $t_{\mathrm{E,pl}}$, $\pi_{\mathrm{E,N}}$, $\pi_{\mathrm{E,E}}$ and $f_{\mathrm{s,sat}}$, the latter representing the scaling flux for the K2C9 photometry.

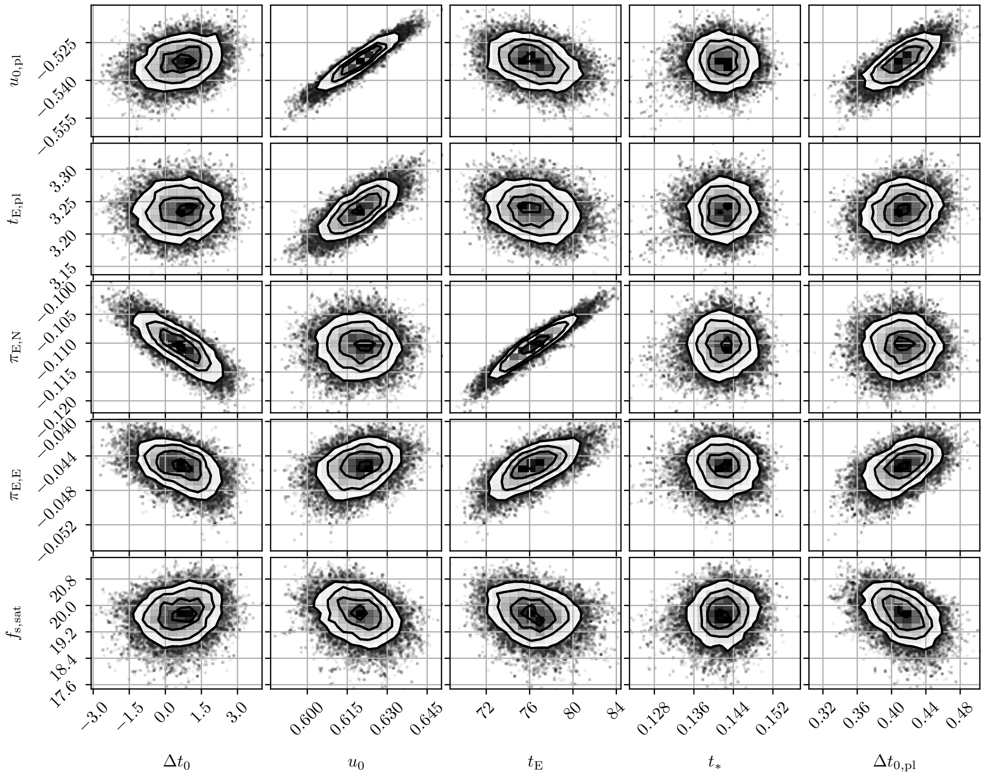

FIGURE 4.12: Shown are the final 2D joint distributions of parameters from figures 4.10 and 4.11. Here, the strongest correlations between parameter pairs are shown, those being $(u_0, u_{0,\mathrm{pl}})$ and $(t_{\mathrm{E}}, \pi_{\mathrm{E,N}})$.

4.4 Analysis of the source

Having established the best microlensing model solution that fits the data, there remains one important analysis before the planet and host mass can be extracted. The angular diameter of the source θ_* is required in concert with ρ to allow for the mass measurement, which was evaluated in the CFHT g-i and r-i colours and calibrated to the PanSTARRS-1 g, r and i filters (Magnier et al., 2020; Zang et al., 2018). This calibration produced magnitudes of $g_* = 24.026 \pm 0.013$, $r_* = 22.332 \pm 0.015$ and $i_* = 21.360 \pm 0.015$. As these values were not dereddened to account for the effects of interstellar extinction, a correction was applied using the methodology outlined in Yoo et al. (2004) to acquire the dereddened magnitudes of $g_{*,0} = 19.61 \pm 0.05$, $r_{*,0} = 19.15 \pm 0.05$ and $i_{*,0} = 18.97 \pm 0.04$. This involved calculating the central colour-magnitude of red clump stars (Girardi, 2016) within 60″ of K2-2016-BLG-0005 as a standard candle to estimate the reddening effect, which was evaluated as $g - i = 3.03 \pm 0.04$, $r - i = 1.03 \pm 0.04$ and $i = 17.190 \pm 0.007$ and is shown in figure 4.13.

Using the dereddened source colours of g-i and r-i and the i-band magnitude, a relation between colour and stellar surface-brightness outlined in Boyajian et al. (2012, 2013, 2014) was used to acquire the angular source radius θ_*. This was found to be $\theta_{*,\mathrm{g}} = 2.12\pm, 0.07\mu$as in the g-band and $\theta_{*,\mathrm{r}} = 1.79 \pm 0.07\mu$as in the r-band. These two estimates of θ_*, although consistent within 3σ, provided sufficient tension that it was decided to perform a further analysis on the CFHT-g and -r photometry to judge which dataset provides a more accurate estimate. As a metric of this analysis, the sensitivity of the scale flux f_s of both datasets to individual data points was calculated, implying that a higher sensitivity to single data points reduces the reliability of the filter's dataset at estimating θ_*. To calculate this, the microlensing parameters of the best fit wide model found from section 4.3 were kept constant, while fitting f_s and the baseline flux f_b to a dataset, omitting each datapoint for a different fit. The standard deviation of the scaling fluxes for each band was then calculated, yielding $\sigma_g = 0.07$ for g-band and $\sigma_r = 0.023$ for r-band, suggesting that the CFHT-g band photometry provides a more accurate estimate of θ_* and was henceforth chosen as the filter for evaluating the fiducial lens properties.

4.5 Analysis of the lens

Now that a source angular diameter had been established, the Einstein radius θ_E was then calculated using the relationship

$$\theta_\mathrm{E} = \frac{\theta_*}{\rho} = \theta_* \frac{t_\mathrm{E}}{t_*}, \tag{4.21}$$

giving a value of $\theta_\mathrm{E} = 0.57 \pm 0.03$ mas. The value of ρ, acquired using t_*/t_E, was found to be 0.00187 ± 0.00007, which is a typical value for microlensing events. This fully resolves the microlensing degeneracy between M_L, $\theta_\mathrm{E}$and π_E allowing for a direct lens mass measurement, lens distance measurement, lens-source relative proper-motion measurement, and by evaluating the binary parameters s and s using equations 4.8 and 4.9, we can also

Lens Mass ($M_\odot$)	Planet Mass (M_{jup})	D_{L} (kpc)	μ_{rel} (mas year^{-1})	Projected Separation (AU)	Semi-major Axis (AU)	Period (years)	s	q
0.584 ± 0.031	1.10 ± 0.08	5.20 ± 0.23	2.71 ± 0.07	4.18 ± 0.27	$4.4^{+1.9}_{-0.4}$	13^{+9}_{-2}	1.414 ± 0.007	0.0018 ± 0.0001

TABLE 4.4: The properties of the lens are tabulated above, including the binary parameters s and q. These are evaluated using the source properties of the CFHT-g band and the standard wide binary solution.

obtain the planetary mass M_{pl} and physical projected separation $a_\perp$ of the lens components, given by

$$M_{\text{pl}} = qM_{\text{L}}, \tag{4.22}$$

$$a_\perp = s\theta_{\text{E}} D_{\text{L}}. \tag{4.23}$$

Although not directly obtainable from the microlensing model and source properties, the planet's semi-major axis a and by extension orbital period P can be estimated assuming a model for the normalised host-planet separation s. To this end, a Monte-Carlo simulation was performed by a co-author of the paper, using the already obtained microlensing model and lens parameters, along with a power law distribution of ln(s) given by

$$\frac{dN}{d\ln(s)} \propto s^x, \tag{4.24}$$

where the normalised separation was restricted to the range $0.1 < s < 10$. The orbital inclination and phase were sampled using a uniform distribution, assuming circular orbits. The power x was taken to be 0.49 ± 0.48 following Suzuki et al. (2016). This large uncertainty drives the main contribution to the error on a and P, which were found to be $a = 4.4^{+1.9}_{-0.4}$AU and 13^{+9}_{-2} years. The final parameters of the lens are shown in table 4.4.

4.6 Conclusion

The significance of K2-2016-BLG-0005Lb is highlighted by the circumstances under which it was discovered, namely by a space-based observatory, the Kepler Space Telescope, which was not optimised for microlensing. The successful use of ground-based photometry to provide a parallax measurement was crucial in characterising properties of the lens system such as mass and distance. This discovery verifies the usefulness of future space-based microlensing surveys, such as those by EUCLID and ROMAN, as outlined in chapter 3, which promise to return a significant amount of science from their multi-billion dollar investments, as well as highlighting the importance of joint surveys to assist in resolving the microlensing parallax.

The properties of the host star, with a mass of $0.58 \pm 0.03 M_\odot$ and relative proper motion of $\mu_{\text{rel}} = 2.7 \pm 0.1$ mas year^{-1} suggests a K-dwarf star in the Galactic disk lensing a background source star in the Galactic bar. The planet discovered in this work also

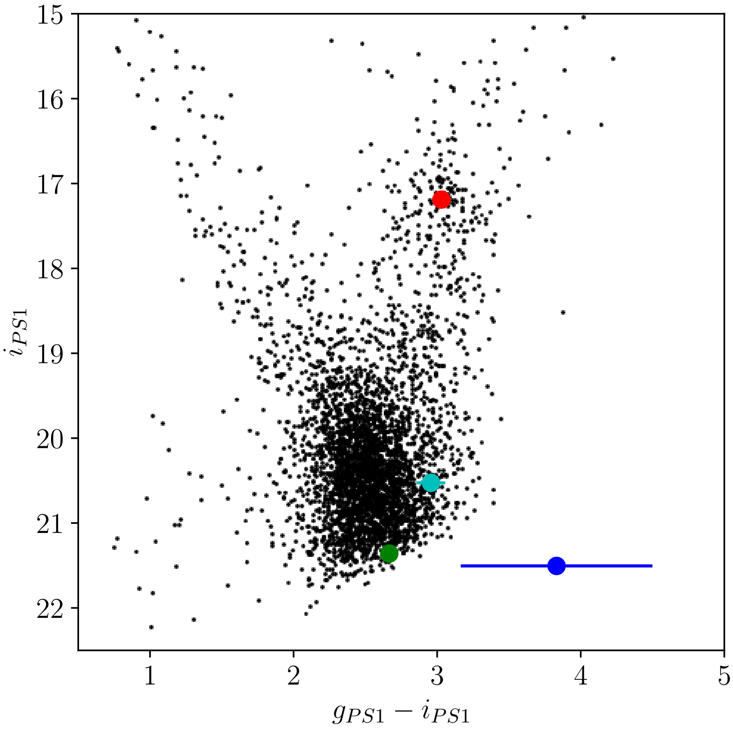

FIGURE 4.13: The colour-magnitude diagram of stars within 60″ of K2-2016-BLG-0005, indicated with black dots, calibrated to the PanSTARRS-1 (*PS1*) system, is shown. The central position of red clump stars is indicated with a red circle, with the source star as a green circle. The cyan circle represents the baseline colour and magnitude of the object coinciding with the location of K2-2016-BLG-0005. The blue circle represents the residual blending light.

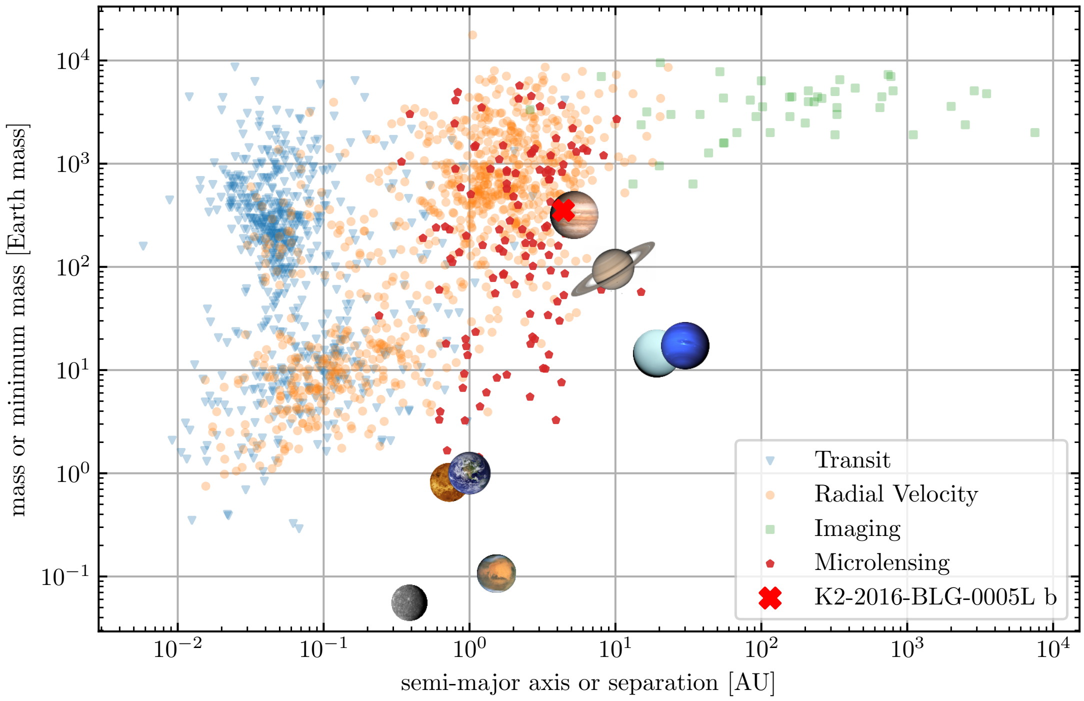

FIGURE 4.14: An updated version of figure 1.1 with K2-2016-BLG-0005Lb indicated by a red cross. The similarity of K2-2016-BLG-0005Lb to Jupiter is clear from this vantage point.

shows a marked similarity to Jupiter, from our own Solar system, albeit with a mass $\sim$ 10% greater and a semi-major axis consistent with that of Jupiter's, although with large uncertainties due to uncertainties in the prior distribution of the binary separation parameter. Its location in the planetary mass and semi-major axis parameter space, relative to previously discovered and confirmed exoplanets is shown in figure 4.14. This once more proves the applicability of microlensing as an astute method of detecting exoplanets beyond the snow line and once again bodes well for future dedicated microlensing surveys by EUCLID and ROMAN. The mass of K2-2016-BLG-0005Lb is also significant in this context, as planetary formation models predict that such planets are unlikely to be found around low mass stars (Kennedy & Kenyon, 2008).

Although this event was well described by a binary lensing model, with the advent of future dedicated microlensing surveys, it is inevitable that higher order lens systems, such as trinary lenses with either a binary star host orbited by a bound planet, or the even more tantalising possibility of a host star, orbited by an exoplanet, itself with a gravitationally bound exomoon, will be detected. The introduction of additional lens objects breaks the axial symmetry of the caustic structure about the primary/secondary axis and significantly increases the number of possible topologies beyond the close, resonant and wide variants. This added complexity significantly increases the computation required to fit to the photometry of such an event and as such, requires innovative methods to make this a practical venture, which shall now be discussed.

Chapter 5

Complex Caustics

As discussed in chapter 4, we can use `MulensModel` to efficiently evaluate a finite-source binary magnification with parallax considerations for good measure. Extending this to trinary lens systems on the other hand is more difficult, not simply because of the larger parameter space and hence degeneracies (Daněk & Heyrovský, 2019), but also due to the time complexity of solving numerically for the magnification of trinary or higher order lens systems. To understand the scale of the problem, we must first establish the mathematical relationship between locations in the source plane $\boldsymbol{\phi}$ and their equivalent image locations in the lens plane $\boldsymbol{\theta}$. This is given by the lens equation for N point lenses (e.g. Daněk & Heyrovský (2015)),

$$\boldsymbol{\phi} = \boldsymbol{\theta} - \theta_{\mathrm{E}}^2 \sum_{n=1}^{N} \frac{\mu_n (\boldsymbol{\theta} - \boldsymbol{\theta_n})}{|\boldsymbol{\theta} - \boldsymbol{\theta_n}|^2}, \tag{5.1}$$

$$\mu_n = \frac{M_n}{\sum_k^N M_k}. \tag{5.2}$$

Here, each vector has two components representing the angular coordinates of points in either the source or lens plane from the vantage point of an observer on Earth. The coordinates $\boldsymbol{\theta_n}$ represent the locations of the lens components, while the parameter μ_n represents the reduced mass of a lens component. Note that θ_{E} is calculated using the total mass of the lens system in the case of multiple lenses,

$$\theta_{\mathrm{E}} = \sqrt{\frac{4G}{c^2} \frac{D_{\mathrm{S}} - D_{\mathrm{L}}}{D_{\mathrm{S}} D_{\mathrm{L}}} \sum_{n}^{N} M_n}. \tag{5.3}$$

If we wish to find the locations $\boldsymbol{\theta_i}$ in the lens plane representing the multiple possible images of a single location in the source plane, we must subsequently find the roots of equation 5.1. In 2D vector notation, this is highly impractical and as such, a conversion into complex numbers is often performed when dealing with a multitude of lenses, as outlined by Witt (1990). This conversion works by using the natural orthogonality of the real and imaginary axes to represent a two dimensional vector (normalised to θ_{E}),

$$\boldsymbol{\theta} = \theta_x \hat{\boldsymbol{x}} + \theta_y \hat{\boldsymbol{y}} \rightarrow z = x + iy, \tag{5.4}$$

$$\boldsymbol{\phi} = \phi_x \hat{\boldsymbol{x}} + \phi_y \hat{\boldsymbol{y}} \rightarrow w = p + iq, \tag{5.5}$$

thus leading to a more malleable complex version of equation 5.1,

$$w = z - \sum_{n}^{N} \frac{\mu_n}{\bar{z} - \bar{z}_n}. \tag{5.6}$$

Solving equation 5.6, although more mathematically feasible, is nonetheless a daunting task for multiple lenses. Consider the form of the complex conjugate $\bar{z}$ of a lens location:

$$\bar{z} = \bar{w} + \sum_{n}^{N} \frac{\mu_n}{z - z_n}, \tag{5.7}$$

which can then be substituted back into equation 5.6 to acquire a lens equation purely in terms of the complex lens location z,

$$w = z - \sum_{n}^{N} \frac{\mu_n}{\bar{w} + \left(\sum_{k}^{N} \frac{\mu_k}{z - z_k} \right) - \bar{z}_n}, \tag{5.8}$$

which is a polynomial of order $N^2 + 1$, with a maximum of $5(N-1)$ valid images in the lens plane, satisfying the original lens equation 5.6 and a minimum of $N + 1$. For a binary lens system, this involves solving a 5th order polynomial. For a trinary or quaternary lens system, this swells to a 10th or 17th order polynomial, respectively. Given that trinary lens systems have been observed in the past, such as in Gaudi et al. (2008), it is not unrealistic that with the advent of the large survey era of microlensing, we may observe such exotic lens systems as a binary star host orbited by multiple Jupiter mass circumbinary planetary lenses, such as found by Murat Esmer et al. (2022) using the transit method with the Kepler Space Telescope. The possibility of finding such higher order lenses highlights the importance of streamlining the fitting process for microlensing photometry.

Given that each root must be found and determined, an algorithm which resolves every root of the polynomial must be used. A general method of achieving this is to find the eigenvalues of the polynomial's companion matrix, which at best has a time complexity of $\mathcal{O}(N^3)$ (Banks et al., 2019). This means that in general, the time complexity of solving for the image locations in the lens plane is $\mathcal{O}(N^5)$, making a binary lens fit $\sim$ 7.6 times faster than an equivalent trinary lens fit and $\sim$ 32 times faster than a quaternary lens fit.

A solution to this is to simulate the trajectory of light rays as they pass in reverse from the observer, through the lens plane and into the source plane. By casting enough such rays, a density map can be produced in the source plane with an amplitude proportional to the lens system's magnification map and an accuracy that increases with ray cast density from the lens plane. As evaluating the raycasting location in the source plane only involves solving the lens equation to obtain w, the time complexity of the algorithm is

$\mathcal{O}(MN)$, where the parameter M is the number of raycasts, a marked improvement over direct evaluation, although at the cost of up to millions of raycasts. An example of a situation where raycasting is useful in resolving the microlensing magnification is the lensing of quasars by clusters of stars in their host Galaxies, as suggested by Garsden & Lewis (2010), who used a supercomputer to produce 2D magnification maps of lens systems containing hundreds, thousands and millions of stars with billions of raycasts. We shall now discuss a hypothetical application much closer to home, mere thousands of parsecs away, involving alien civilisations.

5.1 The Earth Microlensing Zone

The prospect of alien civilisations cohabitating our Milky Way Galaxy has been explored at length over the 20th and 21st centuries, in both science fiction and research. Precisely how many we should expect to find is a similarly often discussed topic, popularised by Frank Drake in 1961 via his famous *Drake equation* (Drake, 1961), which aims to put bounds on this number by multiplying a series of successive terms, each restricting the number of planets hosting alien civilisations through some natural mechanism,

$$N = R_* \times f_\mathrm{p} \times n_\mathrm{e} \times f_\mathrm{l} \times f_\mathrm{i} \times f_\mathrm{c} \times L, \tag{5.9}$$

with R_* being the average star formation rate in the Milky Way, f_p the fraction of stars hosting bound planets (a value likely greater than 0.5, as suggested by Cassan et al. (2012); Youdin (2011)), n_e the total number of planets per stellar system which could potentially support life (which may be as high as 50% for Earth mass planets in their host's habitable zone as shown in Bryson et al. (2021)), f_l the fraction of those habitable worlds which eventually go on to support life, f_i the fraction of those life bearing worlds which support life that evolves to become intelligent and develop a civilisation, f_c the fraction of those civilisations which emit technosignatures (Wright et al., 2022) which humanity can detect and finally L, the duration over which such civilisations are capable of producing such observable technosignatures.

The search for extraterrestrial intelligence (SETI, Cocconi & Morrison (1959)) represents the ongoing efforts by humanity to detect the presence of such alien civilisations. Given the huge amount of data collected over decades by SETI related endeavors, the question of determining the optimal locations for searches is often brought up. One way of guiding such a decision is to employ game theory to determine regions of the Galaxy where alien civilisations would be more likely to find the Earth, determine its habitability and hence be more likely to send a signal our way. Examples of such an analysis include work by Kerins (2021), who considered the regions of the Galaxy where an alien telescope would be able to observe a transit of the Sun by the Earth, known as the Earth transit zone (ETZ, Filippova et al. (1991); Heller & Pudritz (2016)). Similarly, one can consider the Earth microlensing zone (EMZ), where our Sun is most likely to behave as a

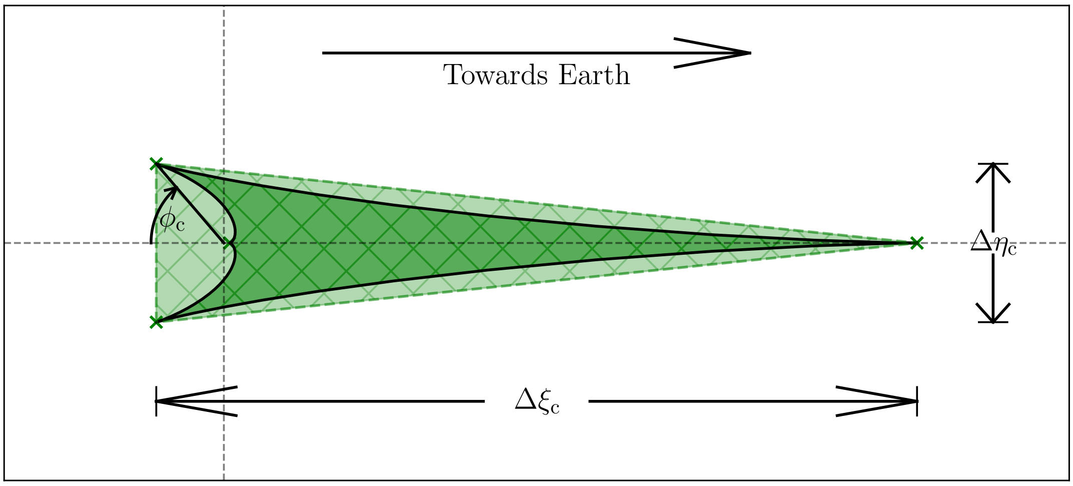

FIGURE 5.1: The dimensions of the central (primary) caustic are shown. The width $\Delta\xi_c$ and height $\Delta\eta_c$ of the caustic structure are also shown, from equations 5.11 and 5.12 respectively. The primary lens is located at the coordinates' origin, with the cusp angle ϕ_c from equation 5.13 shown for the upper off-axis cusp. The true area of the central caustic is shown shaded in a deep green, while the area A_c of the triangle approximant is shown in a lighter shade of green. The direction of Earth relative to the Solar primary lens is shown (off to the right of this diagram).

lens for a microlensing event and hence allow for a possible detection of the Earth given correct alignment.

Combining the two concepts of higher order lensing systems and SETI, this chapter will focus on a part of the work done in the paper *Earth through the looking glass: how frequently are we detected by other civilisations through photometric microlensing?* (Suphapolthaworn et al., 2022), of which the writer is a coauthor. In this study, a catalogue of 1.3 billion stars produced by the Gaia space observatory (Gaia Collaboration et al., 2018) was used by the other authors of the paper to extract candidate microlensing sources and host stars for alien observers. Specifically, a brightness cut of $G < 20$ is applied, brighter than which the stellar proper motion is known to an accuracy greater than 1.2mas year^{-1}. The distances to each star are determined from Gaia's parallax data via Bailer-Jones et al. (2018). Using this data, the microlensing optical depth due to an Earth-Sun caustic region $\tau_\oplus$ was evaluated to determine the probability over a given time period for alien civilisations to detect the Earth in a microlensing event.

To evaluate $\tau_\oplus$, we need an approximate expression for the area of the Earth-Sun binary caustics, which can be thought of as a sum over the central (primary) caustic region and the planetary (secondary) caustic region. As seen in chapter 4, the planetary caustic region consists of a single diamond shaped caustic for the wide topology, while for the close topology the planetary caustics split into two triangular regions, symmetrical about the binary axis. For both topologies the area A_c of the central caustic, as shown in Chung et al. (2005), is given by

$$A_{\mathrm{c}} = \frac{1}{2}\Delta\xi_{\mathrm{c}}\Delta\eta_{\mathrm{c}}, \tag{5.10}$$

$$\Delta\xi_{\mathrm{c}} = \frac{4qs^2}{(s^2-1)^2}, \tag{5.11}$$

$$\Delta\eta_{\mathrm{c}} = \Delta\xi_{\mathrm{c}}\frac{(s^2-1)|\sin^3(\phi_{\mathrm{c}})|}{(s^2-2s\cos(\phi_{\mathrm{c}})+1)^2}, \tag{5.12}$$

$$\cos(\phi_{\mathrm{c}}) = \frac{3}{4s}\left((s^2+1)-\sqrt{s^4-\frac{14}{9}s^2+1}\right), \tag{5.13}$$

where the parameter ϕ_{c} represents the polar angle of the off-axis cusps relative to the binary axis. Each of these parameters are shown in figure 5.1, for the example of an Earth-Sun binary system. The equivalent area A_{p} for the planetary caustic(s) is derived in Han (2006) and is given by

$$A_{\mathrm{p}} = \frac{1}{2}\Delta\xi_{\mathrm{p}}\Delta\eta_{\mathrm{p}}, \tag{5.14}$$

$$\Delta\xi_{\mathrm{p}} = \begin{cases} \frac{4}{s}\sqrt{\frac{q}{s^2-1}}, & s>1 \\ 2\sqrt{q}\cos(\phi_{\mathrm{p}})\left(\frac{\kappa_0^2(s^2+1)-s^2}{\kappa_0 s^2}\right), & s<1 \end{cases}, \tag{5.15}$$

$$\Delta\eta_{\mathrm{p}} = \frac{4}{s}\sqrt{\frac{q}{s^2+1}} \times \begin{cases} 1, & s>1 \\ 1-\sqrt{1-s^4}, & s<1 \end{cases}, \tag{5.16}$$

$$\kappa_0 = s\sqrt{\frac{\cos(2\phi_{\mathrm{p}})+\sqrt{s^4-\sin^2(2\phi_{\mathrm{p}})}}{s^4-1}}, \tag{5.17}$$

$$\phi_{\mathrm{p}} = \frac{1}{2}\left(\pi \pm \arcsin\left(\frac{\sqrt{3}}{2}s^2\right)\right), \tag{5.18}$$

where ϕ_{p} is the equivalent polar angle for the planetary cusps closest to the binary axis. The multiple solutions represent the two cusps of the caustic structure that lie off the axis perpendicular to the binary axis, as shown in figure 5.2. To calculate the optical depth, we must then average the normalised separation parameter s over Earth's orbital phase ψ, via

$$s = \frac{1\mathrm{AU}}{D_{\mathrm{L}}}\sqrt{\sin^2(\psi)+\cos^2(\psi)\sin^2(\beta)}, \tag{5.19}$$

$$\tau = \frac{1}{2\Omega_s}\sum_{n=1}^{N_s}\theta_{\mathrm{E}}^2\int_0^{2\pi} A_{\mathrm{c,n}}(s)+A_{\mathrm{p,n}}(s)d\psi, \tag{5.20}$$

where β is the ecliptic latitude of the nth source star from equation 5.20. Note that the caustic areas are only approximate and diverge significantly as $s \to 1$ where the resonant topology appears, leading to an overestimation of the total area. To account for that, an effective separation parameter s_{eff} is used, defined as

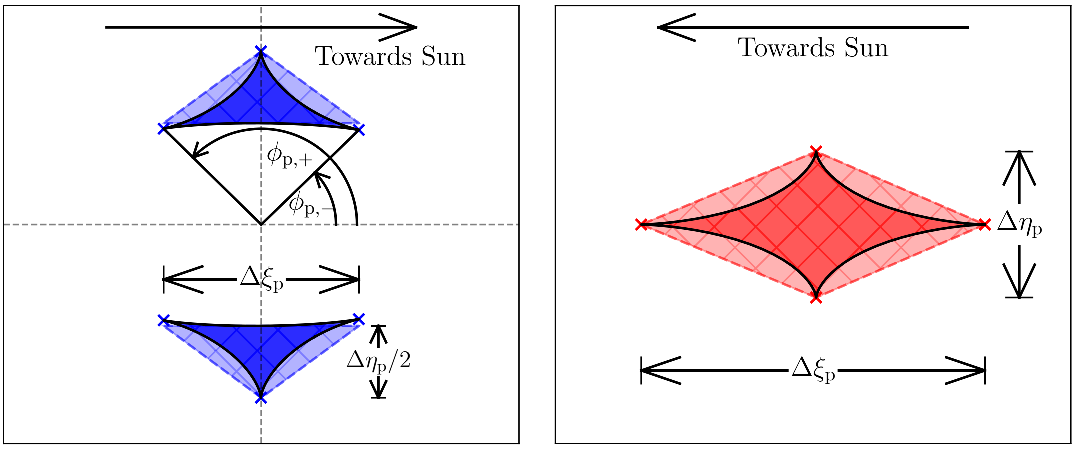

FIGURE 5.2: The dimensions of the planetary caustics are shown, for both the close (left) and wide (right) topologies. The widths are indicated by the parameter $\Delta\xi_{\mathrm{p}}$ defined in equation 5.15 and the heights indicated by $\Delta\eta_{\mathrm{p}}$ defined in equation 5.16. For the close caustics, the cusp angles $\phi_{\mathrm{p},+}$ and $\phi_{\mathrm{p},-}$ from equation 5.18 are shown for the upper caustic structure, while the lower caustic structure is annotated with the dimensions. Note that $\Delta\eta_{\mathrm{p}}$ is shared across the two caustics and hence is halved for each component. Like in figure 5.1, the area A_{p} is indicated in a light shade of blue for the close topology and red for the wide topology and is the area used in this work to approximate the true caustic areas shown in a darker shade of blue and red. For the wide topology, the shape used to approximate the caustic is a diamond which connects all four cusps. This is in contrast to the close topology, where the bases of the two triangle approximants are tangential to the caustic curves, meaning that only the corners furthest from the binary axis correspond with cusps on the caustic structures (note the vertical offset between the triangle approximant and two of the caustic cusps). The direction of the Solar (primary) lens relative to the caustics is shown for the different topology scenarios.

$$s_{\mathrm{eff}} = \begin{cases} 0.99, & 0.99 \leq s < 1 \\ 1.01, & 1.0 \leq s < 1.01 \\ s, & \text{otherwise} \end{cases} . \tag{5.21}$$

This correction alleviates some of the inaccuracy, but there remain larger concerns which motivate the use of higher order lensing models to describe caustics. While this correction alleviates some of the inaccuracy involved in approximating a caustic structure with a set of triangles and quadrilaterals, it does not address the effect of introducing other planets in our Solar System into the lensing potential, particularly Jupiter and Saturn which are hundreds of times more massive than the Earth and hence an analysis must be conducted to verify whether a simple binary approximation of an Earth-Sun system is sufficient to model a microlensing event observed from any of the candidate stars in the Gaia catalogue used in this study. To this end, a raycasting algorithm was developed which models the Solar System with all of its planets except Mercury in an attempt to study the effect of the other planets on the shape of Earth's caustic signature in the full Solar System caustic network which represents the contribution to this work by the writer.

5.1.1 The Raycasting Algorithm

In its simplest form, a raycasting algorithm comprises of an emission plane from which one casts rays and a receiver plane which the cast rays are incident on. In between these two planes, some transform may be applied which influences the travel direction of the rays as they travel from the emission to receiver planes, which in the case of microlensing is given by equation 5.6. As the angular size of the caustic structures produced by the planets of the Solar System are small compared to θ_{E}, a simple setup using a single emission plane which entirely contains the components of the lens system and a single receiver plane large enough to cover the full extent of the Solar System's caustic network would result in the overwhelming majority of the ray casts to miss any caustic structures and simply trace out a predominantly PSPL magnification map. As we are mostly interested in the shape of the Earth's planetary caustics, this is an extremely inefficient approach.

To deal with this, we can use the small mass ratios of the lens components to our advantage by assuming as a starting condition, that the locations of the caustic structures and critical boundaries can be approximated by their binary planet-Sun equivalents. This is important, as we can then begin to optimise the locations and sizes of the emission and receiver planes for the Earth's planetary caustics. To begin with, a realistic Earth-Sun separation parameter of $s = 0.3$ for the EMZ observers was used, with the planets of the Solar System aligned in two distinct test configurations; one with the North ecliptic pole aligned with the observer's viewing axis and another more realistic, edge on scenario using planetary locations calculated at the epoch MJD = 59507[1]. Having established the locations of each of the lens components in a 2-dimensional space normalised to θ_E, the locations and sizes of the emission planes were then established.

In a binary lens system, the location of the planetary caustics along the binary axis is given by

$$x = s - \frac{1}{s}, \tag{5.22}$$

which puts the caustics between the primary and planetary lens in the wide scenario and on the other side of the primary lens to the planetary lens in the close scenario. In the close scenario, the two planetary caustics are offset from the binary axis by

$$\eta_\mathrm{p} = \pm\frac{2}{s}\sqrt{\frac{q}{1+s^2}}, \tag{5.23}$$

from Han (2006). Using equations 5.22 and 5.23, the initial guess for the caustic locations is determined and a ten step Newton-Raphson iteration is used to refine the locations of the caustics using the eight-fold lens equation, which becomes the central location of the receiver planes. The location of the emission planes should likewise cover the extent of the critical boundaries, which are the caustic structures projected back onto the lens plane. For the wide topology, this location is simply the location of the lens, again with some numerical adjustments to account for perturbations arising from other lenses in the system. For the close topology, there are two critical boundaries, corresponding to the two planetary caustics. They have the same distance along the binary axis as the lens itself, but like the close planetary caustics, have an offset transverse to the binary axis given by

$$\Delta X_\mathrm{p} = \pm s\sqrt{q}. \tag{5.24}$$

Although the caustic structures themselves depend solely on the location of the critical boundaries, to construct an accurate magnification map and hence more accurately determine the effect of introducing a large number of lenses, a further contribution to the magnification at the location of the receiver plane must be added from the primary lens background, which in the case of the Sun is approximately a PSPL magnification map. To acquire this location, the image location transformation from equation 1.10 is used and similarly improved for accuracy using a Newton-Raphson iteration such that the transformed emission plane entirely covers the corresponding receiver plane.

This setup results in two emission planes per caustic structure, one for the caustics themselves and another for the background magnification. For a wide configuration, this results in a single receiver plane per lens, while the close topology requires a receiver plane for each of the two planetary caustics and hence four emission planes per lens. The sizes of the planes was also determined to allow enough coverage of the caustic and the magnification produced by any cusps. For the emission planes covering the critical

---

[1] Planetary coordinates relative to the Sun were acquired using an online tool available at `http://cosinekitty.com/solar_system.html`

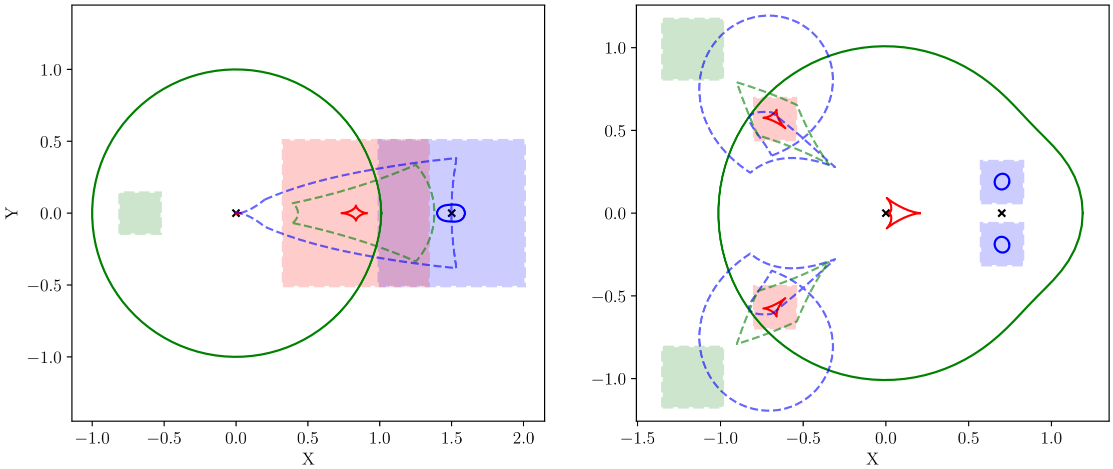

FIGURE 5.3: Shown on the left are the raycasting emission and receiver planes for a wide ($s = 1.5$, $q = 0.005$) binary lens, with lens locations indicated by black crosses. The filled red plane shows the extent of the receiver plane, while the blue and green planes are the critical boundary and PSPL background emission planes, respectively. The distorted shapes of the un-lensed emission planes are shown with their respective colours overlapping the receiver plane, with outlines only. The critical boundary encompassing the primary lens is indicated with a solid green line, while the critical boundary encompassing the planetary lens is shown as a solid blue line. The caustics are drawn as solid red lines. On the right is a similar setup, but using a close topology ($s = 0.7$, $q = 0.07$), where the extra emission and receiver planes are needed. In this case, the un-lensed shapes of the critical boundary emission planes (dashed blue lines) are highly distorted, with edges passing through each other due to the nature of the lens transform between the critical boundaries.

boundaries as well as the corresponding receiver plane, the width was simply taken to be four times the caustic width $\Delta\xi_{\mathrm{p}}$, while the width d_{BG} of the PSPL background emission plane was given by

$$d_{\mathrm{BG}} = 4\sqrt{q} \times \begin{cases} 1, & \text{wide} \\ s^3, & \text{close} \end{cases} . \tag{5.25}$$

An example of the locations of the emission and receiver planes using a pure binary lens configuration is shown in figure 5.3 for both the wide and close topology.

Some final improvements were made to the magnification map around the planetary caustics to clean up the result. As can be seen in figure 5.3, the un-lensed shapes of the emission planes do not cover the entirety of the receiver plane and as such, only the portion of the receiver plane with full coverage from both emission planes is useful. To this end, the magnification map was cropped using a rectangular shape to remove any incomplete portions. The result was then placed over a much lower resolution background to show the continuation of the magnification map outside of the crop.

5.1.2 Results

The two configurations of the Solar System are shown in figures 5.4 and 5.5. The resolutions of both the emission and receiver planes was 500 × 500 pixels, with 20 raycasts

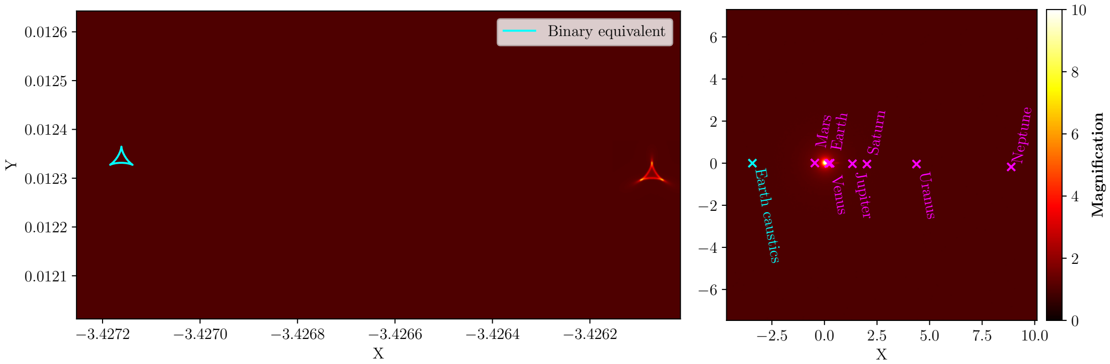

FIGURE 5.4: The Solar System caustic network is shown for the aligned configuration of the Solar System. The upper Earth planetary caustic is shown in the left panel for the eight-fold lens on the right side (as part of the magnification map) and the Sun-Earth binary equivalent on the left (traced out in cyan). On the right is shown a fully zoomed out caustic network, with only a small signature visible to indicate the wide caustics produced by Jupiter. The locations of the planets are shown in magenta, with the location of Earth's planetary caustics indicated in cyan.

per pixel. As the sizes of the two emission planes were different, a scaling factor of $(d_{\mathrm{BG}}/4\Delta\eta)^2$ was introduced to the contribution of the primary background emission raycasts to correct for the differences in ray density at the receiver plane. To quantify the effect on the shape of Earth's planetary caustics by introducing the other lens components studied in this analysis, a metric δ was devised which compared the difference in the areas of the caustic structures between the binary scenario A_{binary} and the full 8-fold lens configuration $A_{8-\mathrm{fold}}$, via

$$\delta = \frac{A_{\mathrm{binary}} - A_{8-\mathrm{fold}}}{A_{8-\mathrm{fold}}}, \tag{5.26}$$

which was found to be $\delta = -3.1 \times 10^{-4}$ for the aligned configuration and $\delta = -6.5 \times 10^{-5}$ for the spiral configuration, suggesting that for lens systems comprised of a heavy primary and multiple smaller secondaries, the shapes of the caustic structures do not change significantly and as such, a binary model would be justified in similar scenarios. On a different note however, as evident in the figures, the offset of the two caustics in the left panels is significant when compared to the width of the caustics. Using a characteristic width given by the average of the side lengths between the three cusps, the offset between the binary and eight-fold Earth planetary caustics was found to be 10.1 and 24.4 times the caustic width for the spiral and aligned configurations respectively. Although significant when compared to the size of the caustics, this offset is unlikely to affect a mass measurement as the size of the offset normalised to the Einstein radius is insignificant and would at worst be misinterpreted as a difference in the projected position of the Earth relative to the Sun and would furthermore be a minor contributor to the sources of error on the final mass measurement.

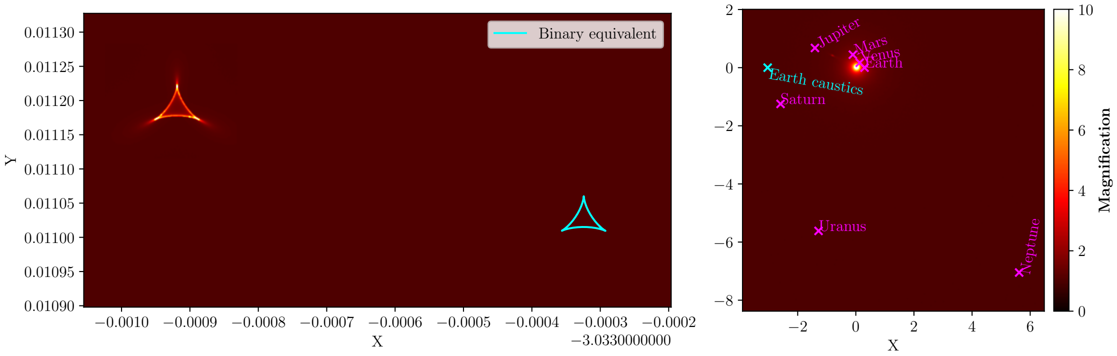

FIGURE 5.5: Same as figure 5.4 but for a spiral configuration of the Solar System, where the viewing axis is aligned with the normal to the plane of the Solar System.

5.1.3 Detection Probability and Event Rate

Returning to the work done by the other authors who contributed to this study, we find that the microlensing optical depth and event rates from crossings of Earth's binary caustics is extremely low by comparison to the lensing towards the Galactic bar as discussed in chapter 2. We find that by summing over the microlensing event rate over the entire sky, a total of 14.7 Earth detections per year would be expected, assuming every Gaia star brighter than $G = 20$ hosts an observing civilisation. Even around the region of highest optical depth in Orion-Cygnus arm at Galactic coordinates $(l, b) = (69.0°, -5.1°)$, we find microlensing parameters of $\tau = 3.28 \times 10^{-10}$ and $\Gamma = 0.0024$ events year^{-1}deg^{-2}, a factor 10,000 times lower than typical values for lensing by stars towards the Galactic bar. When combining this small event rate with the expected occurrence rate of technological civilisations predicted by equation 5.9 (even assuming an upper bound on all currently unknown terms), the number of actual detections of the Earth drops even lower. This suggests that assuming a similar level of technology to ourselves, the Earth is unlikely to be detected via photometric microlensing. With further advances in multi-lens system fitting, one could extend this analysis to model the astrometric microlensing effect of our Solar system as discussed in section 1.8, which would result in a larger optical depth, but remains beyond the scope of this work.

5.2 GPU Powered Microlensing

As raycasting is a massively parallel operation, there are natural ways to improve and streamline the compilation of magnification maps. An obvious way to achieve this is to employ the parallel computing power of a graphics processing unit (GPU - also known as a *graphics card*). To demonstrate the utility of using a GPU to perform microlensing calculations, a compute shader was written using a single emission and receiver plane which compiled a magnification map of resolution 2048×2048 pixels with six raycasts per pixel. A five-fold lens, representing a hypothetical system of a binary red dwarf host system orbited by two gravitationally bound objects, the heavier of which is a low mass brown dwarf and the other a high mass gas giant with a $1.85 M_{\rm Jup}$ mass planetary binary

	Host primary	Host secondary	Brown dwarf	High mass planet	Low mass planet
q	0.6217	0.2931	0.0444	0.0355	0.0053
X	1.819	-0.254	0.942	-0.283	-0.179
Y	-0.537	0.000	0.697	-1.291	-0.141

TABLE 5.1: The lens system configuration (normalised mass and positions) are shown for each component.

companion is simulated. Although highly unlikely to be found in a realistic survey, this lensing system features a complex caustic network which unlike the Earth's EMZ configuration, cannot rely on binary lensing approximations. The parameters used for the lensing system are shown in table 5.1.

Although the magnification map was produced at a high resolution, this comes at a cost of increasing levels of noise due to the lower number of raycasts per pixel at six compared to 20 from the EMZ analysis. The consequences of this are borne out in figure 5.6, where the noise produced by the lower raycast count is evident in the figure insets. This has the consequences of reducing the quality of a fit, given that it has to rely on an inaccurate magnification. One way to overcome this is to employ a de-noising algorithm which attempts to reduce the noise without compromising the sharpness of the magnification map near the edges of the caustic structure. One such algorithm was developed specifically to operate within the paradigm of microlensing magnification maps.

After constructing the mangification map using raycasting, each pixel was iterated over and a denoise operation was performed. Firstly, a check was performed to determine whether the pixel was near the edge of a caustic structure. The spatial derivative $\partial_{X,Y}$ of magnification was calculated for both the horizontal and vertical directions as

$$\partial_X = \frac{M(Y, X + \delta_X) - M(Y, X - \delta_X)}{2\delta_X}, \tag{5.27}$$

$$\partial_Y = \frac{M(Y + \delta_Y, X) - M(Y - \delta_Y, X)}{2\delta_Y}, \tag{5.28}$$

$$\partial_{X,Y} = \sqrt{\partial_X^2 + \partial_Y^2}, \tag{5.29}$$

where δ_X and δ_Y is the size of a pixel in normalised space. The requirement that further de-noising is only applied if $\partial_{X,Y} < 0.7$ was then applied. For those pixels that satisfy this requirement, the mean magnification within a square shaped annulus of side length $n \in [3, 5, 7, 9]$ centred of the target pixel was calculated. The de-noised pixel value was then taken to be the mean over each of these annulus magnifications M_i satisfying $M > 1.2 \times \min(\mathrm{M_i})$. This allowed for a smoothing operation to drastically reduce the noise in the magnification map, while also avoiding blurring over the edges of the caustic which should be preserved and not de-noised. The results of this algorithm are shown for comparison in figure 5.7. Although successful in reducing the noise to near zero, this comes at a cost of edge effects near the caustic boundary; while it is not blurred by the kernel, the magnification leading up to it exhibits a terracing phenomenon on the spatial

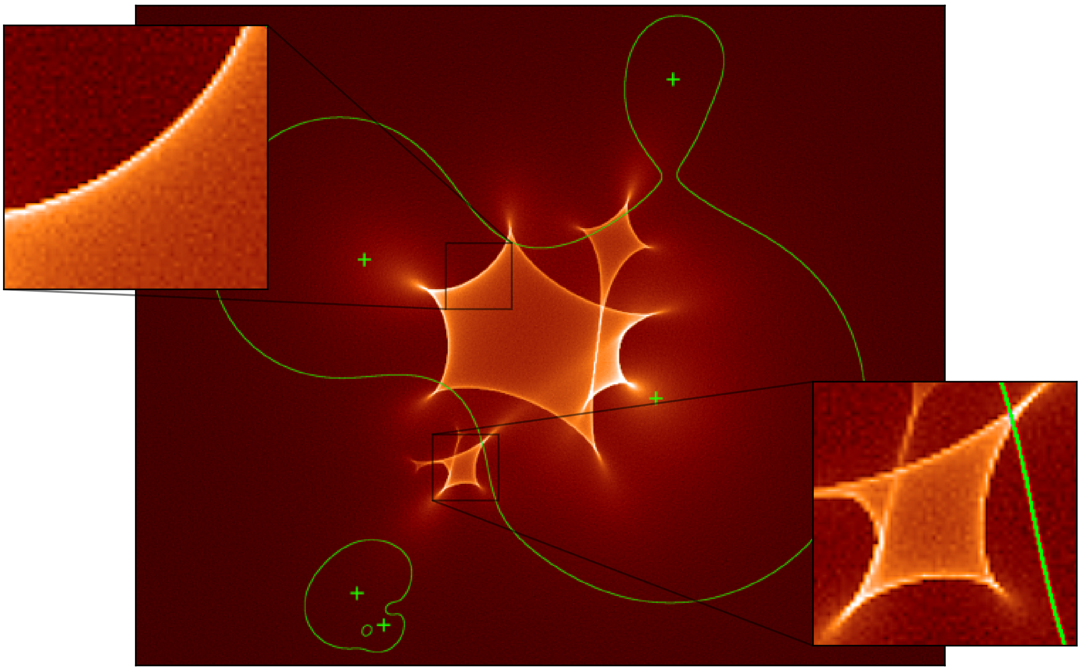

FIGURE 5.6: A noisy magnification map of the lenses described in table 5.1 is shown, with critical boundaries drawn as a green line and lens locations indicated by green plus symbols. Insets are shown to the left and right to highlight the significance of the noise.

scale of a pixel, due to the outer annuli being suppressed as one approaches the edge of the caustic structure.

Another benefit of using the GPU to construct magnification maps is that it is relatively straight forward to draw critical boundaries as well. As the critical boundaries of a lensing system represent the locations where the sign of the determinant J of the lens transform's Jacobian changes from positive to negative (or vice versa), the value of J can be evaluated at each corner of the pixel and their signs multiplied together. If the result of this multiplication is negative, then the pixel definitely exists over a critical boundary. This can be extended by evaluating more samples of J along a border or indeed in a grid pattern centred on a pixel if the drawing thickness of the critical boundary should be greater than a single pixel.

The performance gains from employing a GPU are significant, with a 2048×2048 resolution magnification map at six raycasts per pixel taking approximately 0.1 seconds using a Nvidia GTX 1080 GPU, compared to 800 seconds using a single core of an Intel Xeon W-2104 CPU processor building the same magnification map. Although in practice, multi-threading could be used to bring down the total compute time to ~ 100 seconds using the CPU, the performance gain from employing the GPU remains three orders of magnitude faster. This highlights the importance of using GPU accelerated programming in microlensing calculations, specifically for tasks that can be massively parallelised. This is also a comparatively cheap option, as the GPU used is six years old at the time of writing and is less expensive than high end commercially available CPUs. Of note is the the fact that the operation bottleneck when computing the magnification map is not

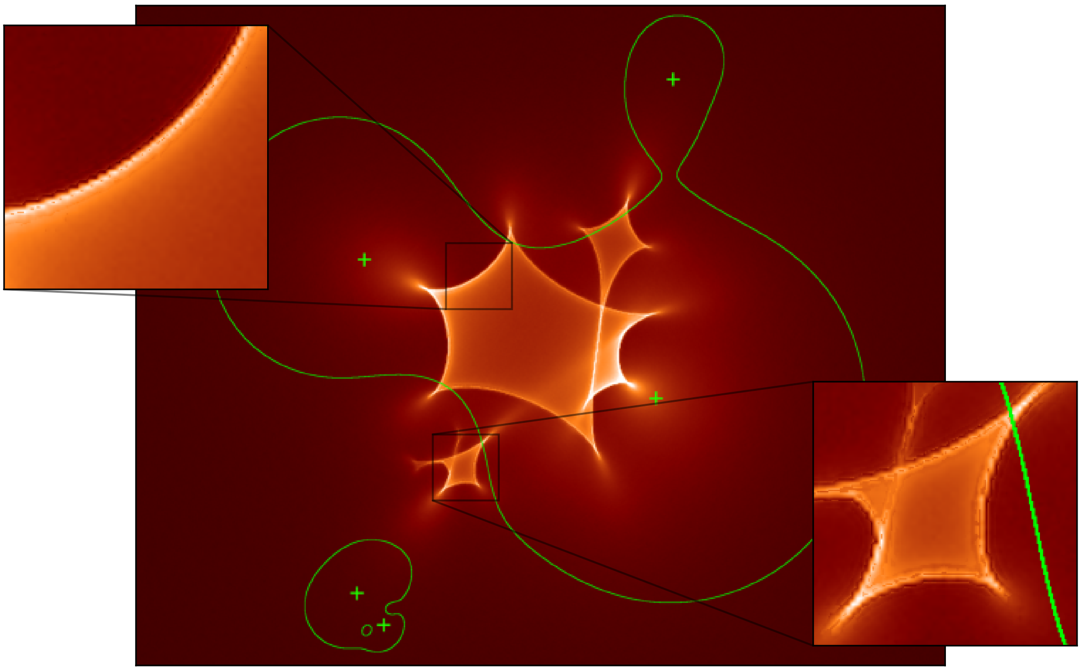

FIGURE 5.7: Shown is the result of applying the de-noising algorithm to the magnification map in figure 5.6. Here, the noise is visibly lessened, but edge effects are present near caustic structure boundaries.

the evaluation of the lens transform, but rather the read and write operations required to update the map's pixels, suggesting that the complexity of the lensing system can be significantly increased before producing a noticeable performance degradation.

5.3 Conclusion

This chapter has served to demonstrate the performance benefits of using raycasting to evaluate the microlensing magnification for complex lens systems, with a striking benefit of employing a GPU running a compute shader. This work has confirmed the binary-lens assumption made while evaluating the microlensing optical depth due to the Earth-Sun caustic structure as observed by alien civilisations in the EMZ as valid, suggesting only very small changes on the order of 10^{-4} of the area of eight-fold lens and binary lens Earth planetary caustics. Although successfully employed in this context, there remain many further steps to overcome before using raycasting as a means of fitting higher order lensing models to observed photometry.

One clear optimisation that could be made is to restrict emission planes to only cover regions which will be received over the desired source trajectory. Currently, the entire magnification map is built, along with a higher resolution zoom of a caustic structure(s), but typically we are only interested in a small strip of the magnification map representing the source's trajectory and only wide enough to accommodate finite source effects. As such, future work could significantly cut down on the total read and write operations performed by the GPU, or simply reducing the number of raycasts performed on a multi-threaded CPU, by estimating appropriate areas to place emission planes which minimise the unused portions of the magnification map.

A second avenue of improvement would be in handling the noise currently inherent in any raycasted magnification map. This could be handled simply by increasing the number of samples from six to a higher number, being careful to avoid race conditions inherent in parallel programming, although this brute force approach comes at the cost of increasing read and write operations on the GPU. For sufficiently large numbers of samples, one could attempt to evaluate the magnification contribution to each unique pixel affected by a single batch of raycasts, although this runs into issues caused by the limited functional programming capabilities of shader languages like GLSL. An alternative would be to develop a much more rigorous de-noising algorithm, being careful not to compromise the accuracy of the magnification result. For instances where finite source effects are strong due to a large value of ρ, the noise becomes less significant as it is averaged out during the convolution of the finite source kernel, although this once again comes at a cost of an increase in the number of pixel reads to sample the magnification map after compilation to estimate the finite source magnification.

Chapter 6

Conclusion

The work presented in this thesis is an exploration of techniques invaluable to the large survey era of gravitational microlensing. Beginning with the work done in Specht et al. (2020), a microlensing tool was developed to predict, with unprecedented accuracy, the rate of microlensing events for telescopes of varying specifications spanning a large swathe of the sky around the Galactic centre. The MaBμlS-2 microlensing simulator described in chapter 2 introduced a formal treatment of finite source effects, background light and improved error estimation, with each factor proving useful in follow-up work. The accuracy of MaBμlS-2 was demonstrated by comparing the empirical OGLE-IV event rate from Mróz et al. (2019) to that predicted by the simulator, showing a high degree of agreement that improves upon previous work by Awiphan et al. (2016).

In Bachelet et al. (2022), the run-time estimation of the finite source magnification assisted in the analysis of free-floating planet event rates by a possible joint mission between the EUCLID and ROMAN space telescopes, as discussed in chapter 3, potentially revealing hundreds of Earth mass FFPs with direct mass measurements over the course of such a mission. Such event rates were accompanied by an assurance of scientific return regardless of the rotational alignment of the two observatories' fields, reinforcing the robustness of such a mission proposal. The results from such a mission would further contribute to our understanding of Galactic structure and planetary formation theory in a way unobtainable by other detection methods, such as via the direct imaging of FFP thermal emissions, which have driven the majority of FFP detections thus far and can only access the highest mass portion of the parameter space.

A further bespoke use of the MaBμlS-2 simulation was shown in chapter 4 came in the form of validating results from KEPLER's K2C9 microlensing campaign in McDonald et al. (2021), which aimed to extract possible FFP candidates from an advanced event filtering pipeline, finding five novel candidate events. While the analysis of FFPs could not break the three-fold microlensing degeneracy between lens mass, angular Einstein radius and lens distance and hence obtain mass measurements for these candidates, results from MaBμlS-2 were nonetheless able to show that the new events are consistent with an Earth mass population of FFPs.

One of the novel events from K2C9 was decidedly *not* a free-floating planet event, but rather a microlensing light curve with a clear binary caustic crossing signature. This event was analysed in Specht et al. (2022) using an advanced model fitting code, operating on the well sampled caustic crossing photometry provided by KEPLER and yielded both a highly accurate finite source measurement and a microlensing parallax measurement, allowing for an extraction of the lens mass and planetary companion after characterisation of the source properties. This result is highly significant, as it demonstrates that even a space-based observatory designed for a completely different mechanism of exoplanet detection (the transit method in the case of Kepler) is still more than capable of discovering exoplanets via microlensing and with supplementary ground-based data for a space-based parallax measurement, further demonstrates the validity of joint microlensing missions with large baselines. This discovery is a clear proof of concept for a future mission by the EUCLID and ROMAN space-based telescopes which will be optimised for microlensing science.

Although the science return from future microlensing missions will yield many planetary events, the prospect of complex lens systems with three or more lenses must be considered, whether from a host-planet-moon system or an exoplanet gravitationally bound to a binary star. Using a raycasting algorithm outlined in chapter 5, the Solar System was simulated in Suphapolthaworn et al. (2022) using an eight lens system to confirm whether such higher order lens effects would be evident to alien civilisations in the Earth Microlensing Zone. It was determined that for an aligned Solar System, a binary approximation would be valid for a mainly straightforward rate calculation. In other scenarios with larger mass ratios, the binary approximation may break down contingent on the alignment of the lens components and the trajectory of the source. To this end, the raycasting algorithm was adapted to use a graphics processing unit which can produce high resolution magnification maps in fractions of a second, paving the way for more computationally efficient fitting algorithms using three or more lenses in the microlensing model.

All of the work presented in this thesis represents a step forward in microlensing simulation, designed to equip researchers with a next generation suite of tools for optimising microlensing surveys and analysing high fidelity data from observatories such as EUCLID and ROMAN. This represents an exciting prospect for the future of exoplanet science, as the microlensing method promises to yield thousands of planet discoveries, on parity with techniques such as the transit and radial velocity methods, while probing a mostly unexplored region of the exoplanet parameter space: the snow line and beyond.

Bibliography

Abe F., et al., 2008, in 17th Workshop on General Relativity and Gravitation in Japan. pp 62–74

Akima H., 1970, J. ACM, 17, 589–602

Alard C., 2000, Astronomy and Astrophysics, Supplement, 144, 363

Albrow M., et al., 1998, Astrophysical Journal, 509, 687

Alcock C., et al., 1992, in Kayser R., Schramm T., Nieser L., eds, Gravitational Lenses. Springer Berlin Heidelberg, Berlin, Heidelberg, pp 156–162

Alcock C., et al., 1995, Astrophysical Journal, Letters, 454, L125

Alcock C., et al., 2000, Astrophysical Journal, 542, 281

Allan A., Naylor T., Saunders E. S., 2006, Astronomische Nachrichten, 327, 767

Arenou F., et al., 2017, Astronomy and Astrophysics, 599, A50

Astudillo-Defru N., et al., 2017, Astronomy and Astrophysics, 602, A88

Awiphan S., Kerins E., Robin A. C., 2016, Monthly Notices of the RAS, 456, 1666

Bachelet E., Penny M., 2019, Astrophysical Journal, Letters, 880, L32

Bachelet E., Hinse T. C., Street R., 2018, Astronomical Journal, 155, 191

Bachelet E., et al., 2022, Astronomy and Astrophysics, 664, A136

Bailer-Jones C. A. L., Rybizki J., Fouesneau M., Mantelet G., Andrae R., 2018, Astronomical Journal, 156, 58

Ban M., 2020, Monthly Notices of the RAS, 494, 3235

Ban M., Kerins E., Robin A. C., 2016, Astronomy and Astrophysics, 595, A53

Banerjee S., Bhattacharyya A., Ghosh S. K., Raha S., Sinha B., Toki H., 2003, Monthly Notices of the RAS, 340, 284

Banks J., Garza-Vargas J., Kulkarni A., Srivastava N., 2019, arXiv e-prints, p. arXiv:1912.08805

Barclay T., Quintana E. V., Raymond S. N., Penny M. T., 2017, Astrophysical Journal, 841, 86

Beichman C., et al., 2014, Publications of the ASP, 126, 1134

Bergbusch P. A., Vandenberg D. A., 1992, Astrophysical Journal, Supplement, 81, 163

Beuzit J. L., et al., 2019, Astronomy and Astrophysics, 631, A155

Bond I. A., et al., 2001, Monthly Notices of the RAS, 327, 868

Bonnarel F., et al., 2000, Astronomy and Astrophysics, Supplement, 143, 33

Boyajian T. S., et al., 2012, Astrophysical Journal, 757, 112

Boyajian T. S., et al., 2013, Astrophysical Journal, 771, 40

Boyajian T. S., van Belle G., von Braun K., 2014, Astronomical Journal, 147, 47

Bozza V., 2010, Monthly Notices of the RAS, 408, 2188

Bozza V., Bachelet E., Bartolić F., Heintz T. M., Hoag A. R., Hundertmark M., 2018, Monthly Notices of the RAS, 479, 5157

Bryson S., et al., 2021, Astronomical Journal, 161, 36

Buchalter A., Kamionkowski M., 1997, Astrophysical Journal, 482, 782

Caldwell J. A. R., Ostriker J. P., 1981, Astrophysical Journal, 251, 61

Cassan A., 2008, Astronomy and Astrophysics, 491, 587

Cassan A., et al., 2012, Nature, 481, 167

Chang K., Refsdal S., 1979, Nature, 282, 561

Chung S.-J., et al., 2005, Astrophysical Journal, 630, 535

Claret A., Bloemen S., 2011, Astronomy and Astrophysics, 529, A75

Clarkson W., et al., 2008, Astrophysical Journal, 684, 1110

Cocconi G., Morrison P., 1959, Nature, 184, 844

Cropper M., et al., 2016, in MacEwen H. A., Fazio G. G., Lystrup M., Batalha N., Siegler N., Tong E. C., eds, Society of Photo-Optical Instrumentation Engineers (SPIE) Conference Series Vol. 9904, Space Telescopes and Instrumentation 2016: Optical, Infrared, and Millimeter Wave. SPIE, pp 269 – 284, doi:10.1117/12.2234739, `https://doi.org/10.1117/12.2234739`

Daněk K., Heyrovský D., 2015, Astrophysical Journal, 806, 63

Daněk K., Heyrovský D., 2019, Astrophysical Journal, 880, 72

Dominik M., 1999, Astronomy and Astrophysics, 349, 108

Dominik M., Sahu K. C., 1998, arXiv e-prints, pp astro–ph/9805360

Drake F. D., 1961, Physics Today, 14, 40

Earman J., Glymour C., 1980, Historical Studies in the Physical Sciences, 11, 49

Eker Z., et al., 2015, Astronomical Journal, 149, 131

El-Badry K., Rix H.-W., Heintz T. M., 2021, Monthly Notices of the RAS, 506, 2269

Euclid Collaboration et al., 2022, Astronomy and Astrophysics, 662, A92

Filippova L. N., Kardashev N. S., Likhachev S. F., Strelnitskij V. S., 1991, in Heidmann J., Klein M. J., eds, , Vol. 390, Bioastronomy: The Search for Extraterrestial Life &mdash; The Exploration Broadens. pp 254–258, doi:10.1007/3-540-54752-5_225

Foreman-Mackey D., 2016, The Journal of Open Source Software, 1, 24

Foreman-Mackey D., Hogg D. W., Lang D., Goodman J., 2013, Publications of the ASP, 125, 306

Gaia Collaboration et al., 2018, Astronomy and Astrophysics, 616, A1

Gardner E., Debattista V. P., Robin A. C., Vásquez S., Zoccali M., 2014, Monthly Notices of the RAS, 438, 3275

Garsden H., Lewis G. F., 2010, New Astronomy, 15, 181

Gaudi B. S., et al., 2008, Science, 319, 927

Girardi L., 2016, Annual Review of Astron and Astrophys, 54, 95

Gomez A. E., Grenier S., Udry S., Haywood M., Meillon L., Sabas V., Sellier A., Morin D., 1997, in Bonnet R. M., et al., eds, ESA Special Publication Vol. 402, Hipparcos - Venice '97. pp 621–624

Gould A., 2000, Astrophysical Journal, 542, 785

Gould A., Loeb A., 1992, Astrophysical Journal, 396, 104

Goullioud R., et al., 2012, in Clampin M. C., Fazio G. G., MacEwen H. A., Jr. J. M. O., eds, Society of Photo-Optical Instrumentation Engineers (SPIE) Conference Series Vol. 8442, Space Telescopes and Instrumentation 2012: Optical, Infrared, and Millimeter Wave. SPIE, pp 654 – 664, doi:10.1117/12.927808, `https://doi.org/10.1117/12.927808`

Han C., 2006, Astrophysical Journal, 638, 1080

Han C., et al., 2016, Astrophysical Journal, 827, 11

Heller R., Pudritz R. E., 2016, Astrobiology, 16, 259

Henderson C. B., et al., 2016, Publications of the ASP, 128, 124401

Hennebelle P., Chabrier G., 2008, Astrophysical Journal, 684, 395

Howell K. C., 1984, Celestial Mechanics, 32, 53

Hugot E., Ferrari M., El Hadi K., Costille A., Dohlen K., Rabou P., Puget P., Beuzit J. L., 2012, Astronomy and Astrophysics, 538, A139

Hwang K.-H., et al., 2022, Astronomical Journal, 163, 43

Jeong J., et al., 2015, Astrophysical Journal, 804, 38

Johnson S. A., Penny M., Gaudi B. S., Kerins E., Rattenbury N. J., Robin A. C., Calchi Novati S., Henderson C. B., 2020, Astronomical Journal, 160, 123

Kaltenegger L., Traub W. A., 2009, Astrophysical Journal, 698, 519

Kennedy G. M., Kenyon S. J., 2008, Astrophysical Journal, 673, 502

Kerins E., 2021, Astronomical Journal, 161, 39

Kerins E., Robin A. C., Marshall D. J., 2009, Monthly Notices of the RAS, 396, 1202

Kim S.-L., et al., 2016, Journal of Korean Astronomical Society, 49, 37

Kim H.-W., et al., 2018a, arXiv e-prints, p. arXiv:1806.07545

Kim H. W., et al., 2018b, Astronomical Journal, 155, 186

Koch D. G., et al., 2004, in Mather J. C., ed., Society of Photo-Optical Instrumentation Engineers (SPIE) Conference Series Vol. 5487, Optical, Infrared, and Millimeter Space Telescopes. pp 1491–1500, doi:10.1117/12.552346

Koshimoto N., et al., 2017, Astronomical Journal, 153, 1

Laureijs R. J., Duvet L., Sanz I. E., Gondoin P., Lumb D. H., Oosterbroek T., Criado G. S., 2010, in Jr. J. M. O., Clampin M. C., MacEwen H. A., eds, Society of Photo-Optical Instrumentation Engineers (SPIE) Conference Series Vol. 7731, Space Telescopes and Instrumentation 2010: Optical, Infrared, and Millimeter Wave. SPIE, pp 453 – 458, doi:10.1117/12.857123, `https://doi.org/10.1117/12.857123`

Lee C. H., Riffeser A., Seitz S., Bender R., 2009, Astrophysical Journal, 695, 200

Limousin M., et al., 2008, Astronomy and Astrophysics, 489, 23

Ma S., Mao S., Ida S., Zhu W., Lin D. N. C., 2016, Monthly Notices of the RAS, 461, L107

Maccone C., 2009, GL-SETI (gravitational lensing SETI): Receiving far ETI signals focused by the gravity of other stars. Springer Berlin Heidelberg, Berlin, Heidelberg, pp 71–84, doi:10.1007/978-3-540-72943-3_6, `https://doi.org/10.1007/978-3-540-72943-3_6`

Macintosh B., et al., 2006, in Ellerbroek B. L., Calia D. B., eds, Society of Photo-Optical Instrumentation Engineers (SPIE) Conference Series Vol. 6272, Advances in Adaptive Optics II. SPIE, pp 177 – 188, doi:10.1117/12.672430, `https://doi.org/10.1117/12.672430`

Magnier E. A., et al., 2020, Astrophysical Journal, Supplement, 251, 6

Mao S., Paczynski B., 1991, Astrophysical Journal, Letters, 374, L37

Marshall D. J., Robin A. C., Reylé C., Schultheis M., Picaud S., 2006, Astronomy and Astrophysics, 453, 635

McBride J., Graham J. R., Macintosh B., Beckwith S. V. W., Marois C., Poyneer L. A., Wiktorowicz S. J., 2011, Publications of the ASP, 123, 692

McDonald I., et al., 2021, Monthly Notices of the RAS, 505, 5584

Mellier Y., 1999, Annual Review of Astron and Astrophys, 37, 127

Miret-Roig N., et al., 2022, Nature Astronomy, 6, 89

Mogavero F., Beaulieu J. P., 2016, Astronomy and Astrophysics, 585, A62

Moniez M., 2009, arXiv e-prints, p. arXiv:0901.0985

Mordasini C., 2018, Planetary Population Synthesis. Springer International Publishing, Cham, pp 2425–2474, doi:10.1007/978-3-319-55333-7_143, `https://doi.org/10.1007/978-3-319-55333-7_143`

Mróz P., et al., 2017, Nature, 548, 183

Mróz P., et al., 2019, Astrophysical Journal, Supplement, 244, 29

Muraki Y., et al., 1999, Progress of Theoretical Physics Supplement, 133, 233

Murat Esmer E., Baştürk Ö., Osman Selam S., Aliş S., 2022, arXiv e-prints, p. arXiv:2202.02118

Nightingale J. W., Massey R. J., Harvey D. R., Cooper A. P., Etherington A., Tam S.-I., Hayes R. G., 2019, Monthly Notices of the RAS, 489, 2049

Nucita A. A., de Paolis F., Ingrosso G., Giordano M., Manni L., 2017, International Journal of Modern Physics D, 26, 1741015

Oasa Y., Tamura M., Sugitani K., 1999, Astrophysical Journal, 526, 336

Paczynski B., 1986, Astrophysical Journal, 304, 1

Paczynski B., 1991, Astrophysical Journal, Letters, 371, L63

Padoan P., Nordlund Å., 2002, Astrophysical Journal, 576, 870

Penny M. T., 2014, Astrophysical Journal, 790, 142

Penny M. T., et al., 2013, Monthly Notices of the RAS, 434, 2

Penny M. T., Rattenbury N. J., Gaudi B. S., Kerins E., 2017, Astronomical Journal, 153, 161

Penny M. T., Gaudi B. S., Kerins E., Rattenbury N. J., Mao S., Robin A. C., Calchi Novati S., 2019, Astrophysical Journal, Supplement, 241, 3

Poindexter S., Afonso C., Bennett D. P., Glicenstein J.-F., Gould A., Szymański M. K., Udalski A., 2005, Astrophysical Journal, 633, 914

Poleski R., Yee J. C., 2019, Astronomy and Computing, 26, 35

Poleski R., Penny M., Gaudi B. S., Udalski A., Ranc C., Barentsen G., Gould A., 2019, Astronomy and Astrophysics, 627, A54

Racca G. D., et al., 2016, in MacEwen H. A., Fazio G. G., Lystrup M., Batalha N., Siegler N., Tong E. C., eds, Society of Photo-Optical Instrumentation Engineers (SPIE) Conference Series Vol. 9904, Space Telescopes and Instrumentation 2016: Optical, Infrared, and Millimeter Wave. SPIE, pp 235 – 257, doi:10.1117/12.2230762, `https://doi.org/10.1117/12.2230762`

Ricker G. R., et al., 2014, in Oschmann Jacobus M. J., Clampin M., Fazio G. G., MacEwen H. A., eds, Society of Photo-Optical Instrumentation Engineers (SPIE) Conference Series Vol. 9143, Space Telescopes and Instrumentation 2014: Optical, Infrared, and Millimeter Wave. p. 914320 (`arXiv:1406.0151`), doi:10.1117/12.2063489

Robin A. C., Reylé C., Derrière S., Picaud S., 2003, Astronomy and Astrophysics, 409, 523

Robin A. C., Marshall D. J., Schultheis M., Reylé C., 2012, Astronomy and Astrophysics, 538, A106

Robin A. C., Reylé C., Fliri J., Czekaj M., Robert C. P., Martins A. M. M., 2014, Astronomy and Astrophysics, 569, A13

Sabelhaus P. A., Decker J. E., 2004, in Mather J. C., ed., Society of Photo-Optical Instrumentation Engineers (SPIE) Conference Series Vol. 5487, Optical, Infrared, and Millimeter Space Telescopes. pp 550–563, doi:10.1117/12.549895

Sajadian S., Poleski R., 2019, Astrophysical Journal, 871, 205

Sauer T., 2008, Archive for History of Exact Sciences, 62, 1

Schönrich R., Binney J., Dehnen W., 2010, Monthly Notices of the RAS, 403, 1829

Sekiguchi M., Fukugita M., 2000, Astronomical Journal, 120, 1072

Shvartzvald Y., Bryden G., Gould A., Henderson C. B., Howell S. B., Beichman C., 2017, Astronomical Journal, 153, 61

Sing D. K., 2010, Astronomy and Astrophysics, 510, A21

Skowron J., Gould A., 2012, arXiv e-prints, p. arXiv:1203.1034

Skowron J., et al., 2016, Acta Astronomica, 66, 1

Specht D., Kerins E., Awiphan S., Robin A. C., 2020, Monthly Notices of the RAS, 498, 2196

Specht D., et al., 2022, arXiv e-prints, p. arXiv:2203.16959

Spergel D., et al., 2015, arXiv e-prints, p. arXiv:1503.03757

Sumi T., Penny M. T., 2016, Astrophysical Journal, 827, 139

Sumi T., et al., 2003, Astrophysical Journal, 591, 204

Sumi T., et al., 2011, Nature, 473, 349

Sumi T., et al., 2013, Astrophysical Journal, 778, 150

Suphapolthaworn S., Awiphan S., Chatchadanoraset T., Kerins E., Specht D., Nakharutai N., Komonjinda S., Robin A. C., 2022, Monthly Notices of the RAS,

Suzuki D., et al., 2016, ApJ, 833, 145

Trick W. H., van de Ven G., Dutton A. A., 2016, Monthly Notices of the RAS, 463, 3151

Tsapras Y., 2018, Geosciences, 8, 365

Tsapras Y., et al., 2009, Astronomische Nachrichten, 330, 4

Udalski A., 2003, Acta Astronomica, 53, 291

Udalski A., Szymanski M., Kaluzny J., Kubiak M., Mateo M., 1992, Acta Astronomica, 42, 253

Udalski A., et al., 1994a, Acta Astronomica, 44, 165

Udalski A., Szymanski M., Kaluzny J., Kubiak M., Mateo M., Krzeminski W., Paczynski B., 1994b, Acta Astronomica, 44, 227

Udalski A., Kubiak M., Szymanski M., 1997, Acta Astronomica, 47, 319

Udalski A., Szymański M. K., Szymański G., 2015, Acta Astronomica, 65, 1

Van Cleve J. E., Caldwell D. A., 2016, Kepler Instrument Handbook, Kepler Science Document KSCI-19033-002, id.1. Edited by Michael R. Haas and Steve B. Howell

Veras D., Raymond S. N., 2012, Monthly Notices of the RAS, 421, L117

Walsh D., 1989, in Moran J. M., Hewitt J. N., Lo K. Y., eds, Gravitational Lenses. Springer Berlin Heidelberg, Berlin, Heidelberg, pp 11–22

Walsh D., Carswell R. F., Weymann R. J., 1979, Nature, 279, 381

Wang D., Hogg D. W., Foreman-Mackey D., Schölkopf B., 2016, Publications of the ASP, 128, 094503

Witt H. J., 1990, Astronomy and Astrophysics, 236, 311

Witt H. J., Mao S., 1994, Astrophysical Journal, 430, 505

Wright J. T., 2018, in Deeg H. J., Belmonte J. A., eds, , Handbook of Exoplanets. p. 4, doi:10.1007/978-3-319-55333-7_4

Wright J. T., Gaudi B. S., 2013, in Oswalt T. D., French L. M., Kalas P., eds, , Planets, Stars and Stellar Systems. Volume 3: Solar and Stellar Planetary Systems. p. 489, doi:10.1007/978-94-007-5606-9_10

Wright J. T., Howard A. W., 2009, Astrophysical Journal, Supplement, 182, 205

Wright J. T., Haqq-Misra J., Frank A., Kopparapu R., Lingam M., Sheikh S. Z., 2022, Astrophysical Journal, Letters, 927, L30

Wyrzykowski Ł., et al., 2010, Monthly Notices of the RAS, 407, 189

Wyrzykowski Ł., et al., 2015, Astrophysical Journal, Supplement, 216, 12

Wyrzykowski Ł., et al., 2016, Monthly Notices of the RAS, 458, 3012

Yee J. C., et al., 2012, Astrophysical Journal, 755, 102

Yee J. C., et al., 2015, Astrophysical Journal, 802, 76

Yoo J., et al., 2004, Astrophysical Journal, 603, 139

Youdin A. N., 2011, Astrophysical Journal, 742, 38

Zang W., et al., 2018, Publications of the ASP, 130, 104401

Zapatero Osorio M. R., Béjar V. J. S., Martín E. L., Rebolo R., Barrado y Navascués D., Bailer-Jones C. A. L., Mundt R., 2000, Science, 290, 103

Zhao H., Mao S., 1996, Monthly Notices of the RAS, 283, 1197

van Kooten M. A. M., Doelman N., Kenworthy M., 2020, Astronomy and Astrophysics, 636, A81